

A MEASUREMENT OF THE
TRIPLE GAUGE BOSON COUPLINGS
FROM e^+e^- COLLISIONS
AT 183–189 GEV

Stephen T. Betts
University College, London

Submitted to the University of London
in fulfillment of the requirements
for the award of the degree of
Doctor of Philosophy.
July 1999.

ABSTRACT

Measurements of the trilinear gauge boson vertex coupling parameters based on data collected in 1997 and 1998 by the OPAL detector at LEP are presented in this thesis. Integrated luminosities of 57fb^{-1} at $\sqrt{s} = 183\text{GeV}$ and 183fb^{-1} at $\sqrt{s} = 189\text{GeV}$ were collected in 1997 and 1998 respectively. The selected data samples comprise 247 events at $\sqrt{s} = 183\text{GeV}$ and 747 at $\sqrt{s} = 189\text{GeV}$. The parameters were measured using a Near Neighbour Maximum Likelihood analysis; the Near Neighbour technique is a method by which a differential cross-section or probability density at a single position in phase-space may be obtained from a large reference sample of simulated events. The main parameters measured are the α_W - $\alpha_{W\phi}$ - $\alpha_{B\phi}$ set (for the 1997 data) and λ - Δg_Z^1 - $\Delta\kappa_\gamma$ set (for the 1998 data); these two sets of parameters were chosen as they may have anomalous values without violating the $\text{SU}(2)_L \times \text{U}(1)_Y$ symmetry of the Electroweak Lagrangian. The measured parameter values are

$$\begin{aligned}\alpha_W &= 0.012_{-0.240}^{+0.343} \pm 0.056 \\ \alpha_{W\phi} &= 0.039_{-0.128}^{+0.144} \pm 0.022 \\ \alpha_{B\phi} &= -0.423_{-0.345}^{+0.493} \pm 0.470\end{aligned}$$

from the 1997 data and

$$\begin{aligned}\lambda &= -0.059_{-0.081}^{+0.086} \pm 0.061 \\ \Delta g_Z^1 &= -0.010_{-0.073}^{+0.076} \pm 0.054 \\ \Delta\kappa_\gamma &= 0.211_{-0.251}^{+0.314} \pm 0.210,\end{aligned}$$

from the 1998 data. The first quoted error is statistical and the second is the systematic uncertainty. All of these values are consistent with zero, which is the value for each of the parameters predicted by the Standard Model.

ACKNOWLEDGEMENTS

I owe a lot of people thanks for their assistance during the course of my degree. In particular I would like to thank my supervisor, Peter Clarke, and Peter Sherwood and Gideon Bella for their essential guidance. In addition, I am particularly grateful to David Miller, Jenny Thomas and the rest of the H.E.P. group at U.C.L.; to Nigel & Miriam Watson, Dave Charlton and the rest of the WW working group; and also to Ed McKigney, Jim Libby, Dave Eatough, Max Sang and Jon Couchman.

CONTENTS

1	AN INTRODUCTION TO THE STANDARD MODEL	1
1.1	The Fundamental Particles	1
1.1.1	The Fermions	2
1.1.2	The Bosons	4
1.2	Gauge Theories of Elementary Particle Physics	8
1.3	The Electroweak Theory	10
1.3.1	The Higgs Mechanism	10
2	TRILINEAR GAUGE VERTEX INTERACTIONS	15
2.1	The Electroweak Gauge Boson Lagrangian	16
2.1.1	Explicit $SU(2)_L \times U(1)_Y$ invariance in the General T.G.C. Lagrangian	19
2.1.2	Limits on the Energy Scale for New Physics	22
2.2	The T.G.C. Cross-section	23
2.2.1	The W-pair production Cross-section	23
2.2.2	The Decay Angle Cross-section	28
2.2.3	Obtaining the T.G.C. Angles from the Decay Fermions	32
3	THE LEP COLLIDER AND OPAL DETECTOR	37
3.1	The LEP Collider	37
3.2	The OPAL Detector	40
3.2.1	Tracking Chambers	43
3.2.2	Low-Angle Subdetectors	45

3.2.3	The Solenoid and Time of Flight Counters	46
3.2.4	The Calorimeters	47
3.2.5	The Outer Muon Detectors	50
3.2.6	The Trigger	51
3.2.7	Data Acquisition	51
4 EVENT RECONSTRUCTION AND DATA SELECTION		53
4.1	The Signal and Background Processes	53
4.1.1	The Signal Processes	53
4.1.2	Background processes	58
4.2	The Monte Carlo Samples	62
4.2.1	The four-fermion signal and background processes	62
4.2.2	Other background processes	63
4.3	The WW and WV utility packages	64
4.3.1	Event reconstruction	64
4.3.2	The Likelihood Event Selection	64
4.3.3	Kinematic Fitting.	77
4.3.4	The Effect of the Selection on Kinematic Variables	79
4.4	The Performance of the Selection Algorithm	80
4.4.1	The Selected Data Sample	80
4.4.2	Expected signal and background cross-sections	80
4.4.3	Efficiency and Purity	85
5 THE NEAR NEIGHBOUR MAXIMUM LIKELIHOOD ANALYSIS		89
5.1	Introduction to the N.N.M.L. Method	89
5.2	The Single-Parameter N.N.M.L. Method	93
5.2.1	Measuring the Differential Cross-section from a Monte Carlo Sample	93

5.2.2	Extrapolating the Probability Density as a Function of the T.G.C. Strength	97
5.2.3	Maximum Likelihood Fitting of the Data Sample	99
5.3	Configuration and Performance of the N.N.M.L.	102
5.3.1	The Statistical Error in the Parabolic Fit	102
5.3.2	Comparing the Different Kernels	105
5.3.3	Optimization of r_0	109
5.3.4	N.N.M.L. Fitting to Different Values of the T.G.C. Pa- rameters	112
5.4	Incorporating All Accepted Processes	116
5.4.1	Correcting the Total Cross-section	116
5.4.2	Incorporating The Inclusive Differential Cross-Section . .	117
5.5	The Multi-Parameter N.N.M.L. Method	120
5.5.1	The Multi-Parameter Likelihood Function	120
5.5.2	Measuring the Hyperparabola Parameters	122
5.5.3	Performance and Optimization of the Multi-Parameter Fits	124
5.6	Incorporating a Systematic Error	126
6	THE MEASUREMENT OF THE T.G.C.S	129
6.1	Measured Values of the T.G.C. Parameters	130
6.2	Log-Likelihood Curves and Fitted Values	132
6.2.1	The Basic N.N.M.L. Fit	132
6.2.2	Incorporating the Expected Background Level	136
6.2.3	The Measurement Using the Inclusive Cross-Section . . .	136
6.2.4	Incorporating the Systematic Error	142
6.3	Measured Limit on the Scale of New Physics	145
7	EVALUATION OF THE SYSTEMATIC ERROR	147

7.1	Systematic Error on the Total Cross-Section	147
7.1.1	Electroweak Modelling	149
7.1.2	Selection Algorithm Acceptance	151
7.1.3	The Dependence of the Cross-section on Kinematic Pa- rameters	153
7.1.4	Detector Simulation	155
7.2	Uncertainties in the Decay Distributions	156
7.2.1	Finite Monte Carlo Statistics	156
7.2.2	The Background Estimation	159
7.2.3	Monte Carlo Modelling	160
7.2.4	Detector Simulation	160
7.2.5	Jet Reconstruction	163
8 CONCLUSION		167
8.1	Review of the N.N.M.L. Method	167
8.1.1	Possible Modifications of the Method	167
8.1.2	The Performance of the N.N.M.L.	169
8.1.3	Comparison With Other Methods	169
8.2	Discussion of the Measurements	172
A MONTE CARLO SAMPLES		175
A.1	Monte Carlo Samples at $\sqrt{s} = 183\text{GeV}$	175
A.2	Monte Carlo Samples at $\sqrt{s} = 189\text{GeV}$	179

LIST OF FIGURES

1.1	A wine-bottle potential, cutaway to show its unstable minimum.	11
2.1	The two trilinear gauge boson vertices in the Standard Model Electroweak theory.	16
2.2	The processes involving the trilinear gauge boson vertices; W-pair production and the $W e \nu_e$ process.	17
2.3	Schematic illustration of the decay angles, θ^* and ϕ^* , of a particle with momentum \mathbf{p}_f^*	28
2.4	Plots of the W^- production angle and the decay angles taken from simulated Monte Carlo events.	30
2.5	The angle between the true and calculated momenta of the neutrino and W^\pm boson.	33
3.1	Schematic representation of the accelerators at CERN.	39
3.2	A schematic representation of the OPAL detector.	41
3.3	Cross-section diagrams of the OPAL detector.	42
4.1	Feynman diagrams of the W-pair production leading to a $q\bar{q}l\nu_l$ final state	54
4.2	Energies of the fermions from $W^+W^- \rightarrow q\bar{q}l\nu_l$ decays.	54
4.3	The angular separation of fermions from $W^+W^- \rightarrow q\bar{q}l\nu_l$ decays.	55
4.4	Charged current processes leading to a $q\bar{q}l\nu_l$ final state.	57
4.5	Neutral current processes leading to a $l\bar{l}q\bar{q}$ final state.	59
4.6	Feynman diagram for the 2-photon interaction.	60
4.7	Feynman diagram of radiative fermion-pair production via an intermediate Z^0 boson.	60
4.8	Distributions of some of the preselection variables.	69

4.9	Distributions of some of the variables used in the likelihood function.	71
4.10	Distribution of the relative likelihood function.	73
4.11	An event selected as $q\bar{q}'\mu\nu_\mu$ at $\sqrt{s} = 183\text{GeV}$, displayed using GROPE.	75
4.12	An event selected as $q\bar{q}'e\nu_e$ at $\sqrt{s} = 189\text{GeV}$, displayed using GROPE.	76
4.13	Distributions of the resolution of the energy of charged leptons from $W^+W^- \rightarrow q\bar{q}'l\nu_l$ events.	78
4.14	Distributions of E_L and $\cos\theta_W$ from $W^+W^- \rightarrow q\bar{q}'l\nu_l$ events showing different reconstruction levels.	79
4.15	Plots showing the distributions of the data sample in the angular variable phase-space.	81
5.1	Schematic representation of the prototypical N.N.M.L. analysis method.	92
5.2	Illustrations of three different kernels.	94
5.3	Parabolic cross-section functions, fitted to discrete, measured values.	100
5.4	χ^2 distributions obtained using different kernels.	104
5.5	Fitted results comparing different kernels with different methods of choosing the length scale, r_0	108
5.6	Fitted results using the Gaussian kernel with various values of $N_{RP/DP}$ and f_{r_0} at $\sqrt{s} = 183\text{GeV}$	110
5.7	Fitted results using the Gaussian kernel with various values of $N_{RP/DP}$ and f_{r_0} at $\sqrt{s} = 189\text{GeV}$	111
5.8	Bias plots of the main parameters at $\sqrt{s} = 183\text{GeV}$ and $\sqrt{s} = 189\text{GeV}$	113
5.9	Bias plots of other T.G.C. parameters at $\sqrt{s} = 183\text{GeV}$	115
5.10	Plot showing the effect of using inclusive reference samples . . .	118

5.11	Plot showing the distributions of the events which fail the multi-parameter fit, for the data sample and for a Standard Model 4-fermion Monte Carlo sample.	123
5.12	95% C.L.L. contours for the λ - Δg_Z^1 - $\Delta\kappa_\gamma$ parameters from multi-parameter fits.	125
6.1	Log-likelihood curves for the main T.G.C. parameters measured using the basic N.N.M.L. on the 183GeV and 189GeV data. . .	134
6.2	Log-likelihood curves for additional T.G.C. parameters measured using the basic N.N.M.L. on the 183GeV data.	135
6.3	Log-likelihood curves for the main T.G.C. parameters measured using the basic N.N.M.L. fit incorporating the expected total cross-section.	137
6.4	Log-likelihood curves for the additional T.G.C. parameters measured using the basic N.N.M.L. fit incorporating the expected total cross-section.	138
6.5	Log-likelihood curves for the main T.G.C. parameters measured using the inclusive cross-section N.N.M.L..	139
6.6	Log-likelihood curves for additional T.G.C. parameters measured using the inclusive cross-section N.N.M.L..	140
6.7	95% C.L.L. contours for the λ - Δg_Z^1 - $\Delta\kappa_\gamma$ parameters measured from the 1998 data using the multi-parameter inclusive N.N.M.L..	141
6.8	Log-likelihoods curves for the main T.G.C. parameters measured using the inclusive N.N.M.L. incorporating the expected systematic error.	143
6.9	Log-likelihoods curves for additional T.G.C. parameters measured using the inclusive N.N.M.L. incorporating the expected systematic error.	144
8.1	Likelihood curves for the λ - Δg_Z^1 - $\Delta\kappa_\gamma$ parameter set obtained using three different analyses on the 1998 data set.	171

LIST OF TABLES

1.1	The fundamental fermions, arranged in generations.	2
1.2	Quantum numbers of the first generation of fundamental fermions.	3
1.3	Properties of the force-carrying bosons.	7
2.1	Terms carrying the couplings and angular dependence of the Standard Model helicity amplitudes.	25
2.2	Terms carrying the couplings and angular dependence of the anomalous coupling helicity amplitudes.	26
4.1	The performance of the selection algorithm at $\sqrt{s} = 183\text{GeV}$. . .	82
4.2	The performance of the selection algorithm at $\sqrt{s} = 189\text{GeV}$. . .	83
7.1	The systematic error on the total cross-section.	148
7.2	The difference between expected accepted cross-section for the main four-fermion processes (excluding final states with e^\pm pairs) generated with the EXCALIBUR and that generated with the <code>grc4f</code> Monte Carlo Generators.	150
7.3	Systematic error due to statistical fluctuations in the Monte Carlo Reference Samples.	152
7.4	Uncertainties in the $W^+W^- \rightarrow q\bar{q}'l\nu_l$ cross-section due to the mass of the W^\pm boson and the beam energy.	154
7.5	Uncertainty in the measured cross-section due to the imperfect detector simulation.	155
7.6	The systematic error on the fitted T.G.C. values.	157
7.7	Estimation of the error due to the finite statistics of the Monte Carlo Reference Samples.	158

7.8	Uncertainty in the fitted values of the T.G.C. parameters due to the statistical error of the non-T.G.C. dependent Monte Carlo reference samples.	159
7.9	Uncertainty in the fitted T.G.C. parameters due to Monte Carlo modelling.	161
7.10	Uncertainties in the fitted T.G.C. parameters due to the imperfect detector simulation.	162
7.11	Uncertainties in the fitted T.G.C. parameters due to the uncertainty in the measured energy and direction of the jets.	164
8.1	The measured T.G.C. parameter values from the OPAL experiment.	172
8.2	95% C.L.L. on the λ - Δg_Z^1 - $\Delta \kappa_\gamma$ parameters from the N.N.M.L. analysis and from the OPAL and DØ experiments.	173
A.1	Monte Carlo Reference samples at $\sqrt{s} = 183\text{GeV}$	175
A.2	Monte Carlo Reference samples at $\sqrt{s} = 189\text{GeV}$	179

CHAPTER 1

AN INTRODUCTION TO THE STANDARD MODEL

The goal of physics has always been to comprehend the fundamental interactions between the most elementary constituents of matter. The most widely accepted theory which does this at present is the Standard Model. However, it is known to be incomplete, a low-energy approximation which, nevertheless, has been exceedingly well verified at the energies scales reached to date. One of the major goals of Particle Physics is to determine where the approximation becomes invalid. In this thesis, one facet of the electroweak force which is relatively unconstrained experimentally—the interactions between its force quanta—is studied in order to measure the values of fundamental parameters for comparison with those values predicted by the Standard Model.

1.1 THE FUNDAMENTAL PARTICLES

In this section, the Standard Model is described in terms of the properties and interactions of the fundamental particles[1, 2]; expressed in this way, the Standard Model seems relatively simple but diverse, with little unity. In the subsequent section (§1.2) the mathematics underpinning the theory, which elegantly expresses its unifying principles, is described.

The fundamental physical interactions occur between fermions (commonly thought of as the “matter” particles), and are mediated by bosons (thought

of as the “force-carrying” particles). The difference between these two types of particles is their intrinsic angular momentum (their “spin”); in units of \hbar , fermions have half-integral spin and bosons have integral spin.

1.1.1 THE FERMIONS

There are two types of fermionic particles: quarks, those fermions which can interact via the strong force, and the leptons, which cannot. There are six flavours of quarks—up, down, charm, strange, top and bottom—and there are six flavours of lepton—electron, muon, tau and their neutrinos. Each of the fermions has a corresponding antiparticle, which has the same mass but opposite quantum numbers, making twenty-four fundamental fermions in total. The fermions are commonly grouped in generations, as in table 1.1; corresponding fermions in different generations have identical quantum numbers, apart from that which specifies the flavour of the fermion; it should also be noted that, with the possible exception of the neutrinos which shall be discussed shortly, the mass of corresponding fermions increases through the generations.

Generation:	I	II	III
Leptons:	$\begin{pmatrix} \nu_e \\ e^- \end{pmatrix}$	$\begin{pmatrix} \nu_\mu \\ \mu^- \end{pmatrix}$	$\begin{pmatrix} \nu_\tau \\ \tau^- \end{pmatrix}$
Quarks:	$\begin{pmatrix} u \\ d \end{pmatrix}$	$\begin{pmatrix} c \\ s \end{pmatrix}$	$\begin{pmatrix} t \\ b \end{pmatrix}$

TABLE 1.1: *The fundamental fermions, arranged in generations.*

Quarks are never observed in isolation, only as composite particles, collectively known as hadrons. Hadrons themselves come in two types: bosonic mesons which are comprised of a quark-antiquark pair; and fermionic baryons

comprised of three quarks or three antiquarks. This property of quarks is somewhat explained by the nature of the colour force, which is outlined later in this chapter.

As the fermions have half-integral spin, they may, *a priori*, exist in two helicity states; however, the situation for neutrinos is not clear at present. Until very recently neutrinos were thought only to exist in left-handed states (negative helicity), and, conversely, anti-neutrinos in right-handed (positive helicity); this would imply that the neutrinos would have to be massless (otherwise there would always be another frame of reference from which the neutrino would be observed in the opposite helicity state). But recent results from Super-Kamiokande[3] have detected evidence of mixing between the different neutrino flavours, which implies that they must have a mass, and, therefore, that both helicity states must exist. As shall be seen, the helicities of the fermions are important in weak interactions.

The basic quantum numbers for the first generation of fermions are given in table 1.2, where C , Q and t_3 are the quantities to which the force quanta couple, as explained in the next section.

Fermion Type	Flavour	Colour Charge	Q	$(t_3)_L$
Quarks	u	R, G or B	$+\frac{2}{3}$	$+\frac{1}{2}$
	d	R, G or B	$-\frac{1}{3}$	$-\frac{1}{2}$
Leptons	e^-	0	-1	$-\frac{1}{2}$
	ν_e	0	0	$+\frac{1}{2}$

TABLE 1.2: *Some quantum numbers of the first generation of fundamental fermions; these are the same for the two successive generations. The quantum numbers for the corresponding antiparticles are obtained by taking the negative of those given in the table.*

1.1.2 THE BOSONS

Bosons are particles with integral spin and all of the force quanta in the Standard Model have spin of 1. There are three forces contained within the Standard Model: the strong force, for which there are eight bosons, called the “gluons”; the electromagnetic force, for which there is a single boson, the “photon”; and the weak force, for which there are three, the “ W^+ ”, “ W^- ” and the “ Z^0 ” bosons. The very different natures of these forces may be explained by the differences in the bosons and their coupling strengths.

GLUONS—THE STRONG FORCE QUANTA

The strong force is mediated by massless particles, called “gluons”. The gluons couple to the colour charge, which has six different types, denoted by R , G , and B (for red, green and blue) and their antiparticle opposites, \bar{R} , \bar{G} , and \bar{B} . Each individual quark is in one of these colour states. The gluons themselves have colour, so that interactions between the gluons themselves will occur. There are eight types of gluons, differentiated by their colour state.

One striking feature of the strong force is that the potential energy of two colour charges increases with their separation (or, more precisely, as the invariant mass of the intermediary gluon decreases). This implies that coloured objects—just the quarks and gluons, of the fundamental particles—never exist as free particles. Because of this, the strong force is never observed as a long range interaction; it has an effective range.

Unlike leptons, when quarks are produced they are observed as showers of particles. The simplest way to picture this is to think of two quarks being produced as a colour singlet state, but moving in opposite directions. As they separate, the potential energy between them increases until two new quarks are produced; now there are two colour singlet states, which no longer strongly interact with each other (and so are effectively free), but may individually continue to split into more colour singlet states. When the initial quark-

pairs are produced at high enough energy, showers (or “jets”) of particles are produced, which is how hadrons are observed in High Energy Physics detectors such as OPAL.

THE PHOTON—THE ELECTROMAGNETIC FORCE QUANTUM

The force quantum of electromagnetism is the photon, which couples to the conventional charge of particles, Q . The photon is massless—implying that it has an infinite lifetime—and uncharged—so it cannot interact with other photons; because of these two properties there is no limit on the range of the electromagnetic force.

Unlike the strong interaction, the electromagnetic coupling strength decreases asymptotically to a finite value as the invariant mass of the intermediary photon decreases; roughly, this implies that the potential energy of two charges decreases with their separation, so electromagnetically charged particles may exist as unbound states.

THE W^\pm & Z^0 BOSONS—THE WEAK FORCE QUANTA

There are three bosons associated with the weak force, two of which—the W^\pm bosons—have an electric charge, whilst the other—the Z^0 boson—is neutral. These particles are massive particles, with a Breit-Wigner mass spectrum; this implies that the weak force bosons have a finite lifetime, and, therefore, a limited range. In fact, the range of the electroweak force is of the order of 10^{-18}m , which is partly why the force appears to be so feeble (it will be seen in the next section that the true weak coupling strength is the same as that of electromagnetism).

The W^\pm bosons couple to the weak isospin of a particle, denoted by “ t_3 ”. Only the negative helicity fermions and positive helicity antifermions have non-zero weak isospin, and so the opposite helicity states do not interact with

the charged weak force bosons. The Z^0 boson couples to a combination of the weak isospin and electromagnetic charge (as in table 1.3), so that it couples to fermions and antifermions in both helicity states (although with different strengths). Only the weak force couples to all the leptons and quarks. Interactions with the Z^0 bosons do not change the flavour of the fermions, but interactions with the W^\pm bosons must.

As the W^\pm bosons are electromagnetically charged and have non-zero weak isospin, they also couple to the Z^0 boson and to the photon. It is the form of these interactions which is the topic of study of this thesis.

The properties of the force quanta are detailed in table 1.3.

THE HIGGS BOSON

It should be stated that the electromagnetic force and the weak force are both facets of a single force, called the “electroweak” force. The unification between these forces cannot easily be expressed in the context of a simple discussion of their force quanta, and is left until the next section. Suffice to say at present that this unification requires an additional boson called the “Higgs boson”, which is yet to be discovered. The Higgs boson is vitally important to the Standard Model, as all of the particles which have mass do so through interactions with its associated field.

This boson has zero intrinsic spin, and is, therefore, a scalar particle, unlike the vector force quanta. It has no colour or electromagnetic charge, but it does have weak isospin of $-\frac{1}{2}$. The Higgs boson has a mass, although its value is not predicted by theory, and, obviously, has not been directly measured; conspicuous by its absence, the 95% confidence level lower limit for the Higgs boson mass is currently 89.7GeV[5].

Force	Boson	Coupling Strength	Mass	Colour	Q	t_3
Strong	Gluons	C^a (colour charge)	0	$C\bar{C}'$ and superpositions of $C\bar{C}$ states	0	0
Electromagnetic	The Photon	Q	0	0	0	0
	W^\pm	t_3	$80.41 \pm 0.10 \text{ GeV}$	0	± 1	$\pm \frac{1}{2}$
Weak	Z^0	$\frac{(t_3 - \sin \theta_{\text{WK}} Q)}{\sin \theta_{\text{WK}} \cos \theta_{\text{WK}}}$	$91.187 \pm 0.007 \text{ GeV}$	0	0	0

^awhere C can be R, G or B

TABLE 1.3: Properties of the force-carrying bosons[4].

1.2 GAUGE THEORIES OF ELEMENTARY PARTICLE PHYSICS

Each of the forces described in the previous section are formulated in the Standard Model as gauge symmetric quantum field theories[6, 7]. Two disjunct theories are required to describe the three forces: quantum chromodynamics (Q.C.D.) and the electroweak theory, which also contains quantum electrodynamics (Q.E.D.).

The transition amplitude for a system to change states may be expressed as an integral equation of the Hamiltonian of the system, which itself is obtained from the Lagrangian. Hence, the system is fully described by its Lagrangian. Feynman derived a method whereby the transition amplitude is given by a sum of representational diagrams; each element of the diagrams has a corresponding “Feynman Rule”, a mathematical expression obtained from the Lagrangian. Knowing the “Feynman Rules” describing an interaction is equivalent to knowing the interaction Lagrangian[8].

As the systems contain particles which may be created or destroyed, their Lagrangians are constructed from creation and annihilation operators which act on the vacuum state. These operators obey canonical commutation or anti-commutation relations and, as they act at a particular position in space, they are field operators. Hence theories based on such Lagrangians are called “Quantum Field Theories”.

To say that these theories are gauge symmetric is to say that the Lagrangians are invariant under local transformations of a characteristic symmetry group; Q.C.D. and the electroweak theories are invariant under local transformations of the $SU(3)_C$ and the $SU(2)_L \times U(1)_Y$ groups, respectively.

For the Lagrangian to be invariant under a certain transformation, its constituents must be covariant with respect to the same transformation. However, Lagrangians typically contain not only the quantized fields themselves, but also derivatives of the fields. Ordinary derivatives cannot be covariant with respect

to a local transformation, and so must be replaced with a covariant form. This “covariant derivative” requires the addition of one or more gauge fields to ensure covariance.

When the symmetries imposed on the Lagrangian belong to Lie groups (as is the case in Q.C.D. and the electroweak force) an arbitrary local transformation, $\mathbf{U}(\phi(\mathfrak{x}))$, may be expressed in terms of the generators of the group[9]:

$$\mathbf{U}(\phi(\mathfrak{x})) = e^{ic\mathbf{\Gamma}\cdot\phi(\mathfrak{x})}. \quad (1.1)$$

In this equation c is an overall scale term, $\phi(\mathfrak{x})$ gives the extent of the transformation at a position \mathfrak{x} , and $\mathbf{\Gamma}$ are the generators of the group which obey the group algebra defined by the structure constants, g_{ijk} :

$$[T_i, T_j] = g_{ijk} T_k. \quad (1.2)$$

Under such a transformation, the covariant derivative is given by

$$\partial^\mu \rightarrow D^\mu = \partial^\mu + ic\mathbf{\Gamma}\cdot\mathbf{F}^\mu, \quad (1.3)$$

where the \mathbf{F}^μ are the gauge fields necessary to restore covariance. These gauge fields form interaction terms with the fermionic fields and are identified as the fields of the force quanta (the gauge bosons) described in the previous section. It can easily be seen from equation 1.3 that there must be one field in the covariant derivative for each of the generators of the group; i.e., there must be one gauge boson for each generator. Hence, there are eight gluons as the $\text{SU}(3)_C$ symmetry of Q.C.D. has eight generators, and there are four electroweak gauge bosons as the $\text{SU}(2)$ group has three generators and the $\text{U}(1)$ group has one.

As the gauge fields represent particles, just as the fermionic fields do, there must be terms in the Lagrangian corresponding to their free fields. Covariant derivatives must also be used for these terms, and as the gauge groups are non-Abelian there will be terms in the Lagrangian which correspond to self-interactions between the gauge bosons.

So, simply imposing a local symmetry upon the fermionic particles' field operators leads elegantly to the emergence of gauge field operators corresponding to the force quanta, which were introduced empirically in the previous section.

1.3 THE ELECTROWEAK THEORY

The analysis described in this thesis investigates the interactions between the electroweak gauge bosons. It is therefore necessary to describe the electroweak theory in some more detail.

The Electroweak Theory is an $SU(2)_L \times U(1)_Y$ gauge symmetric field theory, where the subscripts indicate that the $SU(2)_L$ fields only couple to left-handed fermions (and right-handed anti-fermions) and that the $U(1)_Y$ field couples to the weak hypercharge (which is non-zero for all fermions and anti-fermions). The four gauge fields are the three \mathbf{W}^μ fields of weak isospin, and the B^μ field of the weak hypercharge, but these fields cannot be simply identified with the W^\pm and Z^0 bosons and the photon; gauge symmetry requires that the particles represented by such fields must be massless, which is incompatible with the limited range of the weak bosons. However, the fields and physical, massive gauge bosons may be connected via the Higgs Mechanism.

1.3.1 THE HIGGS MECHANISM

The Higgs mechanism allows gauge symmetric fields to acquire mass, and, as such, is a vitally important part of the Standard Model. Its principal feature is the existence of a scalar field which has a degenerate, non-zero vacuum expectation value. This is normally illustrated with a “wine-bottle” potential, as in figure 1.1; the ground-state of such a potential is not at the origin of the ϕ_1 - ϕ_2 space, but lies in the minimum of the potential. From figure 1.1 it may be seen that this ground-state is infinitely degenerate—as a rotation of the ground state in the complex ϕ_1 - ϕ_2 space yields an equivalent ground-state—and, crucially, it does not display the same symmetry properties as the Lagrangian; hence, the symmetry is referred to as “hidden” or “spontaneously broken”.

The Higgs field of figure 1.1 is a simple $U(1)$ example; the Standard Model

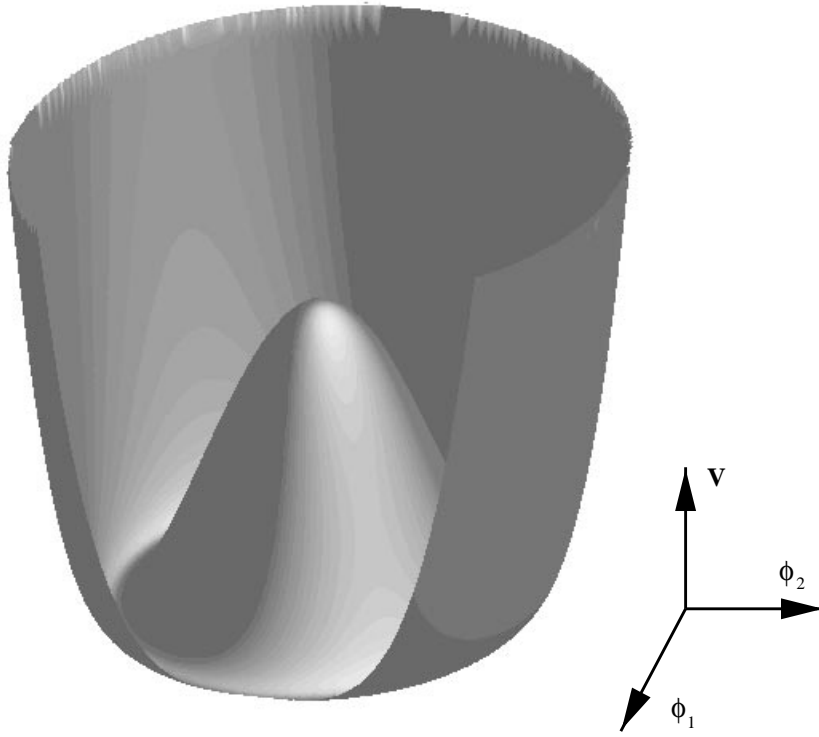


FIGURE 1.1: A wine-bottle potential, cutaway to show its unstable minimum.

Higgs Field is an SU(2) doublet field:

$$\Phi = \frac{1}{\sqrt{2}} \begin{pmatrix} \phi_1 + i\phi_2 \\ \phi_3 + i\phi_4 \end{pmatrix}. \quad (1.4)$$

It is most convenient to impose a choice of gauge (called the “Unitarity Gauge”) on this field, such that

$$\Phi_U = \frac{1}{\sqrt{2}} \begin{pmatrix} 0 \\ f + \sigma(\mathbf{x}) \end{pmatrix}. \quad (1.5)$$

This confers the advantage that f may be interpreted as the constant vacuum expectation value of the Higgs field and deviations from this vacuum state are given by $\sigma(\mathbf{x})$, which is interpreted as the field of the Higgs boson. It should be

noted that the physical content is unchanged by the choice of a specific gauge—equation 1.5—over the general case—equation 1.4—but the interpretation is much simpler.

With such a non-zero valued field permeating the vacuum, all particles which interact with the Higgs field may effectively acquire a mass. In actuality, the form of the Higgs field is such that the charged $SU(2)_L$ fields, given by

$$W^{-\mu} = \frac{1}{\sqrt{2}}(W^{1\mu} - iW^{2\mu}) \quad (1.6)$$

$$W^{+\mu} = \frac{1}{\sqrt{2}}(W^{1\mu} + iW^{2\mu}), \quad (1.7)$$

acquire a mass, and the neutral $SU(2)_L$ and $U(1)_Y$ fields mix to form two new fields,

$$Z^\mu = \cos \theta_{\text{WK}} W^{3\mu} - \sin \theta_{\text{WK}} B^\mu \quad (1.8)$$

$$A^\mu = \sin \theta_{\text{WK}} W^{3\mu} + \cos \theta_{\text{WK}} B^\mu. \quad (1.9)$$

Z^μ is the massive field of the Z^0 boson and A^μ is the massless $U(1)_{\text{EM}}$ field of the photon. The weak mixing angle, θ_{WK} , is defined by

$$\cos \theta_{\text{WK}} = \frac{g}{\sqrt{g^2 + g'^2}} \quad (1.10)$$

$$\sin \theta_{\text{WK}} = \frac{g'}{\sqrt{g^2 + g'^2}}, \quad (1.11)$$

where g and g' are the coupling strengths of the $SU(2)_L$ and $U(1)_Y$ gauge fields, respectively.

In the Standard Model, all of the massive particles acquire their mass via interactions with the Higgs field. However, it should be noted that, while the masses of the gauge bosons are calculable from the electroweak quantum numbers of the Higgs field and measured fundamental parameters, the masses of the fundamental fermions cannot; the only way to determine the coupling strengths of the fermions to the Higgs field is to measure their masses. The fact that the masses of the fermions are entirely unconstrained theoretically is evidence that the Standard Model must be incomplete.

The $SU(2)_L \times U(1)_Y$ form for the gauge fields has been dramatically verified by all experimental evidence so far and particularly by the extensive studies of the Z^0 boson at LEP.

CHAPTER 2

TRILINEAR GAUGE VERTEX INTERACTIONS

The Electroweak theory is non-Abelian, implying that there must, in general, be interactions between its gauge bosons. These self-interactions are fully constrained in the Standard Model, but, prior to LEP-II, were relatively unconstrained experimentally [10, 11]. This thesis describes an attempt to measure fundamental coupling parameters which govern a generalized Lagrangian describing three-way interactions between the gauge bosons; these parameters are referred to as the “Triple Gauge Coupling” or T.G.C. parameters. The measurement is performed by analysing $q\bar{q}'l\nu_l$ final states (where the charged lepton is an electron or muon), which principally arise from W -pair production.

The first section of this chapter describes a generalized Electroweak Self-Interaction Lagrangian. This most general form *is* experimentally constrained by the data collected at LEP-I, and a parametrisation of this Lagrangian is given which does not contradict the data gathered thus far. Anomalous coupling strengths will lead to violation of probability conservation (or “Unitarity violation”) at higher energies, and so the sensitivity of the Scale of New Physics, Λ_{NP} , to the measured T.G.C. parameters is discussed. The differential cross-section derived from this parameterisation of the Lagrangian is described in the next section (§2.2), showing how the distributions of the production angle of the W^\pm bosons and the decay angles of the fermions depend on the T.G.C. parameters. With this in mind, the reasons for studying the $q\bar{q}'e\nu_e$ and $q\bar{q}'\mu\nu_\mu$ final states are discussed at the end of this section.

2.1 THE ELECTROWEAK GAUGE BOSON LAGRANGIAN

There are many possible self-interaction vertices for the electroweak gauge bosons, but only two of these are trilinear (i.e., involving three gauge bosons), shown in figure 2.1.

To first order the trilinear gauge vertices (“T.G.V.s”) are involved in two classes of process at LEP-II: on-shell W-pair production ($e^+e^- \rightarrow W^+W^- \rightarrow f'\bar{f}''f'''\bar{f}''''$) and t-channel single W production ($e^-e^+ \rightarrow We\nu_e \rightarrow e\nu_e f'\bar{f}''$, referred to as the “ $We\nu_e$ process”); these are shown in figure 2.2. These two processes have different characteristics even though $We\nu_e$ events and W-pair events may have the same final states, and the two processes are studied separately; only W-pair production is considered as the signal process in this thesis.

The most general, lowest dimension Lorentz-invariant Lagrangian density

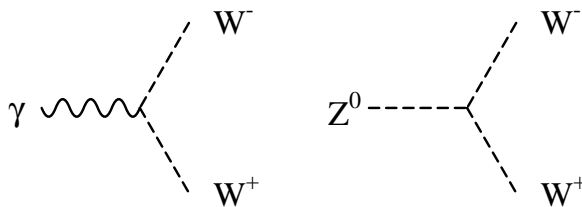


FIGURE 2.1: *The two trilinear gauge boson vertices in the Standard Model Electroweak theory.*

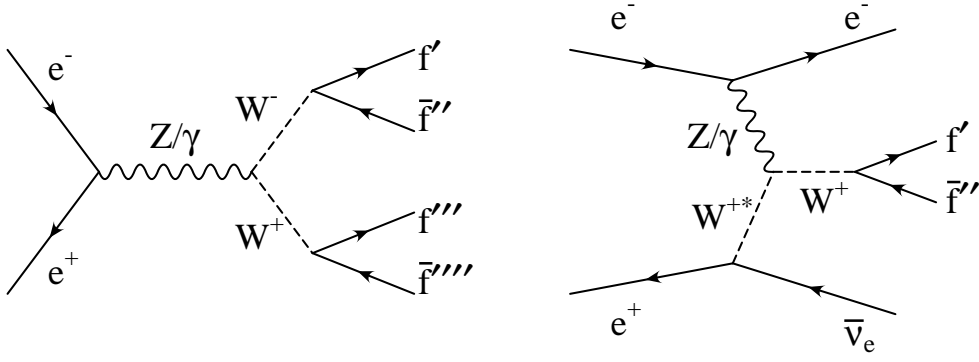


FIGURE 2.2: The processes involving the trilinear gauge boson vertices; W -pair production and the $W e \nu_e$ process.

describing the trilinear gauge vertices contains 14 independent parameters[12]:

$$\begin{aligned}
 \mathcal{L}_{\text{TGC}} = & -ie[g_\gamma^1 A_\mu (W^{-\mu\nu} W_\nu^+ - W^{+\mu\nu} W_\nu^-) + \kappa_\gamma F_{\mu\nu} W^{+\mu} W^{-\nu}] \quad (2.1) \\
 & -ie \cot \theta_{\text{WK}} [g_Z^1 Z_\mu (W^{-\mu\nu} W_\nu^+ - W^{+\mu\nu} W_\nu^-) + \kappa_Z Z_{\mu\nu} W^{+\mu} W^{-\nu}] \\
 & +ie \frac{\lambda_\gamma}{M_W^2} F^{\nu\lambda} W_{\lambda\mu}^- W_\nu^{+\mu} \\
 & +ie \cot \theta_{\text{WK}} \frac{\lambda_Z}{M_W^2} Z^{\nu\lambda} W_{\lambda\mu}^- W_\nu^{+\mu} \\
 & +e g_Z^5 \epsilon_{\mu\nu\rho\sigma} ((\partial^\rho W^{-\mu}) W^{+\nu} - W^{-\mu} (\partial^\rho W^{+\nu})) A^\rho \\
 & +e \cot \theta_{\text{WK}} g_Z^5 \epsilon_{\mu\nu\rho\sigma} ((\partial^\rho W^{-\mu}) W^{+\nu} - W^{-\mu} (\partial^\rho W^{+\nu})) Z^\rho \\
 & +ie \left[\hat{\kappa}_\gamma \hat{F}_{\mu\nu} W^{+\mu} W^{-\nu} + \frac{\hat{\lambda}_\gamma}{M_W^2} \hat{F}^{\nu\lambda} W_{\lambda\mu}^+ W_\nu^{-\mu} \right] \\
 & +ie \cot \theta_{\text{WK}} \left[\hat{\kappa}_Z \hat{Z}_{\mu\nu} W^{+\mu} W^{-\nu} + \frac{\hat{\lambda}_Z}{M_W^2} \hat{Z}^{\nu\lambda} W_{\lambda\mu}^+ W_\nu^{-\mu} \right] \\
 & +ie \hat{\kappa}_\gamma (\partial^\mu A^\nu + \partial^\nu A^\mu) W_\mu^+ W_\nu^- \\
 & +ie \cot \theta_{\text{WK}} \hat{\kappa}_Z (\partial^\mu Z^\nu + \partial^\nu Z^\mu) W_\mu^+ W_\nu^-.
 \end{aligned}$$

In this expression, the charge (C) and parity (P) conserving terms are displayed in blue, the C and P violating, CP conserving terms are displayed in magenta and the CP violating terms are displayed in red, and the following field tensors

have been used:

$$W_{\mu\nu}^{\pm} = \partial_{\mu} W_{\nu}^{\pm} - \partial_{\nu} W_{\mu}^{\pm} \quad (2.2)$$

$$Z_{\mu\nu} = \partial_{\mu} Z_{\nu} - \partial_{\nu} Z_{\mu}.$$

$$\hat{F}_{\mu\nu} \equiv \frac{1}{2} \epsilon_{\rho\sigma\alpha\beta} F^{\alpha\beta} \quad (2.3)$$

$$\hat{Z}_{\mu\nu} \equiv \frac{1}{2} \epsilon_{\rho\sigma\alpha\beta} Z^{\alpha\beta}$$

The Standard Model values of these parameters are such that the Lagrangian respects the electroweak $\text{SU}(2)_L \times \text{U}(1)_Y$ symmetry and does not violate Unitarity:

$$g_{\gamma}^1 = g_Z^1 = \kappa_{\gamma} = \kappa_Z = 1 \quad (2.4)$$

$$\lambda_{\gamma} = \lambda_Z = g_{\gamma}^5 = g_Z^5 = \hat{\kappa}_{\gamma} = \hat{\kappa}_Z = \hat{\hat{\kappa}}_{\gamma} = \hat{\hat{\kappa}}_Z = 0. \quad (2.5)$$

In fact, g_{γ}^1 and g_{γ}^5 are additionally constrained to these values by $\text{U}(1)_{\text{EM}}$ gauge invariance, a powerful enough constraint that they are often not considered as parameters in the relevant literature.

Hence, the Standard Model coupling strengths gives the following Standard Model trilinear gauge vertex Lagrangian density:

$$\begin{aligned} \mathcal{L}_{\text{SM}} = & -ie[A_{\mu}(W^{-\mu\nu}W_{\nu}^{+} - W^{+\mu\nu}W_{\nu}^{-}) + F_{\mu\nu}W^{+\mu}W^{-\nu}] \\ & -ie \cot \theta_{\text{wk}}[Z_{\mu}(W^{-\mu\nu}W_{\nu}^{+} - W^{+\mu\nu}W_{\nu}^{-}) + Z_{\mu\nu}W^{+\mu}W^{-\nu}]. \end{aligned} \quad (2.6)$$

2.1.1 EXPLICIT $SU(2)_L \times U(1)_Y$ INVARIANCE IN THE GENERAL T.G.C. LAGRANGIAN

It is not possible to measure each of the coupling parameters given in the Lagrangian density of expression 2.1 with the limited statistics obtained at LEP-II. However, it is not necessary as the data taken at LEP-I provides strong constraints on the additional terms which are allowed. In particular, the LEP-I data may be protected by embedding any anomalous terms in an $SU(2)_L \times U(1)_Y$ gauge invariant structure[13].

The explicitly $SU(2)_L \times U(1)_Y$ gauge invariant terms may be elegantly expressed in terms of the unmixed fields (the $W^3 B$ base):

$$\mathcal{L}_W = \left(\frac{1}{6}\right) \mathbf{w}^{\mu\nu} \cdot (\mathbf{w}_{\nu\lambda} \times \mathbf{w}_\mu^\lambda) \quad (2.7)$$

$$\mathcal{L}_{W\phi} = i \frac{e}{2 \sin \theta_{\text{WK}}} \mathbf{w}^{\mu\nu} (D_\mu \Phi)^\dagger \boldsymbol{\tau} \cdot (D_\nu \Phi) \quad (2.8)$$

$$\mathcal{L}_{B\phi} = i \frac{e}{2 \cos \theta_{\text{WK}}} B^{\mu\nu} (D_\mu \Phi)^\dagger (D_\nu \Phi). \quad (2.9)$$

In these equations Φ is the scalar Higgs doublet, $\boldsymbol{\tau}$ represents the generators of the $SU(2)$ group, $\mathbf{w}_{\mu\nu}$ is the non-Abelian field tensor and D_μ is the $SU(2)_L \times U(1)_Y$ covariant derivative, which are given by:

$$\mathbf{w}_{\mu\nu} = \partial_\mu \mathbf{W}_\nu - \partial_\nu \mathbf{W}_\mu - \frac{e}{\sin \theta_{\text{WK}}} \mathbf{W}_\mu \times \mathbf{W}_\nu \quad (2.10)$$

$$D_\mu = \partial_\mu + i \frac{e}{\sin \theta_{\text{WK}}} \frac{\boldsymbol{\tau}}{2} \mathbf{W}_\mu + i \frac{e}{\cos \theta_{\text{WK}}} B_\mu Y. \quad (2.11)$$

The $SU(2)_L \times U(1)_Y$ invariant T.G.C. Lagrangian density may now be written as

$$\mathcal{L}_{\text{TGC}} = \mathcal{L}_{\text{SM}} + \alpha_W \mathcal{L}_W + \alpha_{W\phi} \mathcal{L}_{W\phi} + \alpha_{B\phi} \mathcal{L}_{B\phi}, \quad (2.12)$$

where the α parameters— α_W , $\alpha_{W\phi}$ and $\alpha_{B\phi}$ —are the triple gauge coupling strengths to be measured. Upon returning to the mixed base, the α parameters may be expressed in terms of the parameters in the more general Lagrangian

density of equation 2.1:

$$\alpha_{W\phi} = \Delta g_Z^1 \cos^2 \theta_{WK} \quad (2.13)$$

$$\alpha_{B\phi} = \Delta \kappa_\gamma - \Delta g_Z^1 \cos^2 \theta_{WK} \quad (2.14)$$

$$\alpha_W = \lambda \quad (2.15)$$

with the constraints

$$\lambda_\gamma = \lambda_Z \equiv \lambda \quad (2.16)$$

$$\Delta \kappa_Z = -\Delta \kappa_\gamma \tan^2 \theta_{WK} + \Delta g_Z^1, \quad (2.17)$$

The “ Δ ” prefix indicates deviations from predicted values, such that

$$\Delta g_Z^1 \equiv (g_Z^1 - 1) \quad (2.18)$$

$$\Delta \kappa_\gamma \equiv (\kappa_\gamma - 1) \quad (2.19)$$

$$\Delta \kappa_Z \equiv (\kappa_Z - 1). \quad (2.20)$$

It can be seen by comparing these relations with the general T.G.C. Lagrangian density that all the terms in this reduced Lagrangian density conserve both charge and parity.

An anomalous value of any of these parameters would lead to a W-pair cross-section which diverges with the energy scale of the interaction, \sqrt{s} ; unchecked this would lead to Unitarity Violation and so must be countered by some hitherto unknown interaction.

It should be noted[14] that any of the terms in the general T.G.C. Lagrangian may be rendered $SU(2)_L \times U(1)_Y$ by the addition of higher dimension terms, but they will be suppressed by factors of $(E/\Lambda_{NP})^{d-4}$, where d is the dimension of the terms and E is the energy of the interaction[15]. The α -model Lagrangians are all dimension 6, and the relations given in equations 2.13–2.15 are only valid in the approximation that contributions from terms of higher dimension are negligible; but, with that caveat, the two parameter sets are equivalent. These two sets of parameters represent the only $SU(2)_L \times U(1)_Y$ gauge symmetric additions to the T.G.C. Lagrangian up to dimension 6[16, 17].

These two sets of parameters are investigated in the analysis described in this thesis. For the first two years of LEP-II all the LEP experiments used the α -model parameterisation; during the third year (the 183GeV run) a decision was taken that the Δg_Z^1 - $\Delta\kappa_\gamma$ - λ parameter set should be used, to facilitate comparison with the C.D.F. and DØ experiments. Although the two parameter sets are equivalent it is, in general, not possible to transform one set of single-parameter measurements into another set which are a linear combination of those parameters. When all three parameters in one set are measured simultaneously it is possible to transform to the other set, but the values obtained from these 3-parameter fits naturally have much larger errors and, therefore, are not normally quoted.

ADDITIONAL T.G.C. MODELS

Obviously, the parameter set of the general T.G.C. Lagrangian may be reduced with other constraints. In particular, there exist fully simulated Monte Carlo samples at a collision energy (\sqrt{s}) of 183GeV which were generated with anomalous values of two different parameters, $\Delta\kappa_\gamma^{\text{HISZ}}$ and $\Delta\kappa$. The $\Delta\kappa_\gamma^{\text{HISZ}}$ parameter is defined by[18, 19]

$$\Delta\kappa_\gamma^{\text{HISZ}} = \Delta g_Z^1 2 \cos^2 \theta_{\text{WK}} \quad (2.21)$$

$$\Delta\kappa_Z = \Delta\kappa_\gamma^{\text{HISZ}} \frac{(1 - \tan^2 \theta_{\text{WK}})}{2} \quad (2.22)$$

and the $\Delta\kappa$ parameter by

$$\Delta\kappa = \Delta\kappa_\gamma = \Delta\kappa_Z \quad (2.23)$$

$$\Delta g_Z^1 = 0. \quad (2.24)$$

These parameterisations are not so interesting on the aesthetic grounds that they introduce arbitrary constraints on the $\text{SU}(2)_L \times \text{U}(1)_Y$ gauge symmetry of the T.G.C. Lagrangian. For completeness, a measurement of these parameters is presented along with the measurements of the other parameters.

2.1.2 LIMITS ON THE ENERGY SCALE FOR NEW PHYSICS

It is possible to get something of a quantitative hold on the Scale of New Physics from a measurement of the Triple Gauge Couplings. This is because of the previously mentioned fact that anomalous values of the couplings would imply that there must be a new physics process, effective at some higher energy such that Unitarity is not violated. The “Unitarity Limit”, Λ_U , is the maximum energy for such an interaction to become manifest, and, hence, gives an upper limit on the Scale of New Physics, Λ_{NP} [20]. The stronger the anomalous couplings, the lower the Unitarity Limit must be; this is encapsulated in the following expressions for the α -couplings[14]:

$$|\alpha_W| \simeq 19 \left(\frac{M_W}{\Lambda_{NP}^{LIM}} \right)^2 ; \quad |\alpha_{W\phi}| \simeq 15.5 \left(\frac{M_W}{\Lambda_{NP}^{LIM}} \right)^2 ; \quad |\alpha_{B\phi}| \simeq 49 \left(\frac{M_W}{\Lambda_{NP}^{LIM}} \right)^2 . \quad (2.25)$$

Hence, a measurement of the T.G.C. parameters is a genuine attempt to make a quantitative evaluation of physics beyond the Standard Model.

2.2 THE T.G.C. CROSS-SECTION

2.2.1 THE W-PAIR PRODUCTION CROSS-SECTION

The Lagrangian shown in equation 2.1 describes the most general W-pair production process via an intermediate photon or Z^0 boson. By incorporating this into the Standard Model Lagrangian[13], a differential cross-section is obtained which describes the complete W-pair production process (i.e., including the t-channel diagram). It should be noted that this is not the complete cross-section to produce an $f\bar{f}'f''\bar{f}'''$ final state, as other diagrams also contribute (those which do so for the signal are shown in chapter 4, §4.1.1); however, it is the s-channel W-pair production diagrams which give most of the T.G.C. dependence and, at this point, it is appropriate to neglect these extra diagrams.

This cross-section is a function of the angle at which the W bosons are produced in the lab ($\cos\theta_W$), and of the helicities of both the initial state electron-positron pair and the W-bosons. The helicities of the W^\pm bosons—denoted τ^\pm —may take values of $0, \pm 1$. If the W boson has a helicity of ± 1 it is said to be transverse; if it has a helicity of 0 it is said to be longitudinal. Any W-pair final state may be denoted as TT, LL or LT, in an obvious notation. Any arbitrary electron or positron may have a helicity of $\pm\frac{1}{2}$, but in the W-pair production diagrams the incoming electron-positron pair must have opposite helicities which means that the initial state may be specified by a single index, λ .

The following expression shows the W-pair production differential cross-section in terms of $F_{\tau_1\tau_2}^{(\lambda)}$, the amplitudes for producing a $\tau^+\tau^-$ final helicity state from an initial helicity state of λ :

$$\frac{d\sigma(e^+e^- \rightarrow W^+W^-)}{d\cos\theta_W} = \frac{|\mathbf{p}|}{16\pi s\sqrt{s}} \sum_{\lambda, \tau_1, \tau_2} |F_{\tau_1\tau_2}^{(\lambda)}(s, \cos\theta_W)|^2. \quad (2.26)$$

where $|\mathbf{p}|$ is the magnitude of the centre-of-mass momentum of the W^+ or W^- ,

given by

$$|\mathfrak{D}| = \frac{\beta\sqrt{s}}{2} \quad (2.27)$$

$$= \frac{\sqrt{s - 4M_W^2}}{2}. \quad (2.28)$$

The helicity amplitudes are given explicitly by:

$$F_{\tau_1\tau_2}^{(\lambda)}(s, \cos\theta_W) = -\frac{e^2\lambda}{2}s \left[C^{(\nu)}(\lambda, t) M_{\lambda\tau_1\tau_2}^{(\nu)}(s, \cos\theta_W) + \sum_{i=1}^7 \left(C_i^{(\gamma)}(\lambda, s) + C_i^{(Z^0)}(\lambda, s) \right) M_{i,\lambda\tau_1\tau_2}^{(\gamma/Z^0)}(s, \cos\theta_W) \right]. \quad (2.29)$$

This equation requires some explanation; the sum over i in the latter two terms is actually over the trilinear gauge couplings in the general T.G.C. Lagrangian, equation 2.1. The terms of the form $C^{(D)}(\lambda, s \text{ or } t) M_{\lambda\tau_1\tau_2}^{(D)}(s, \cos\theta_W)$ arise from the Feynman diagrams for W-pair production, the superscript indicating from which. The functions $C^{(D)}(\lambda, s \text{ or } t)$ carry the dependence on the couplings, and hence, for the $C_i^{(\gamma)}(\lambda, s)$ and $C_i^{(Z^0)}(\lambda, s)$ terms, the dependence on the anomalous couplings. The $M_{\lambda\tau_1\tau_2}^{(\nu)}(s, \cos\theta_W)$ and $M_{i,\lambda\tau_1\tau_2}^{(\gamma/Z^0)}(s, \cos\theta_W)$ give the helicity composition and the production angle distributions of the W-bosons for the different couplings terms; the $M_{i,\lambda\tau_1\tau_2}^{(D)}(s, \cos\theta_W)$ are the same for corresponding γ and Z^0 contributions. The values of the $C^{(D)}(\lambda, s \text{ or } t)$ and $M_{i,\lambda\tau_1\tau_2}^{(D)}(s, \cos\theta_W)$ terms are well documented so that the differential cross-section for any particular combination of values of the T.G.C.s may be calculated.

It is instructive to look at some of the $C^{(D)}(\lambda, s \text{ or } t)$ and $M_{\lambda\tau_1\tau_2}^{(D)}(s, \cos\theta_W)$ terms; the Standard Model expressions are shown in table 2.1, and the expressions with anomalous couplings allowed within a dimension-6 $SU(2)_L \times U(1)_Y$ framework are shown in table 2.2.

In tables 2.1 and 2.2 the helicity state of $\tau_1 = \pm, \tau_2 = 0$, is given by changing τ_2 for $-\tau_1$ in the terms in the final rows. The vector and axial couplings, a

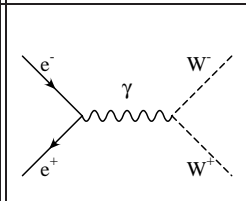
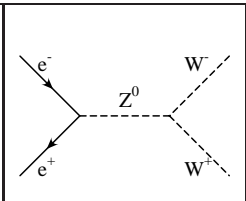
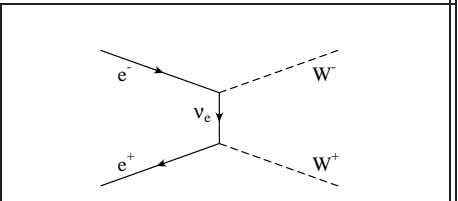
				
$C^{(D)}(\lambda, s \text{ or } t)$		$-\frac{2}{s}$	$\frac{2 \cot \theta_{\text{WK}}}{(s - M_Z^2)} \times$ $(a - 2b\lambda)$	$\frac{2\lambda - 1}{4t \sin^2 \theta_{\text{WK}}}$
$M_{\lambda\tau_1\tau_2}^{(D)}(s, \cos\theta)$	$\tau_1 = \pm 1$ $\tau_2 = \pm 1$	$\frac{1}{2}e^2 s \lambda \sin \theta_{\text{W}} \beta$		$\frac{1}{2}e^2 s \lambda \sin \theta_{\text{W}} \times$ $(\beta - \cos \theta_{\text{W}})$
	$\tau_1 = \pm 1$ $\tau_2 = \mp 1$	0		$\frac{1}{2}e^2 s \lambda \sin \theta_{\text{W}} \times$ $(2\tau_1 \lambda + \cos \theta_{\text{W}})$
	$\tau_1 = 0$ $\tau_2 = 0$	$\frac{1}{2}e^2 s \lambda \sin \theta_{\text{W}} \beta \left(1 + \frac{s}{2M_{\text{W}}^2}\right)$		$\frac{e^2 s^2 \lambda \sin \theta_{\text{W}}}{4M_{\text{W}}^2} \times$ $\left[\cos \theta_{\text{W}} - \beta \left(1 + \frac{2M_{\text{W}}^2}{s}\right)\right]$
	$\tau_1 = 0$ $\tau_2 = \pm 1$	$\frac{e^2 \sqrt{s^3} \lambda \beta}{2\sqrt{2}M_{\text{W}}} (\tau_2 \cos \theta_{\text{W}} - 2\lambda)$		$\frac{e^2 s \lambda}{2\sqrt{2}} (\tau_2 \cos \theta_{\text{W}} - 2\lambda) \times$ $\left[\frac{2M_{\text{W}}}{\sqrt{s}} \frac{\tau_2 \sin^2 \theta_{\text{W}}}{(\tau_2 \cos \theta_{\text{W}} - 2\lambda)} - \frac{\sqrt{s}}{2M_{\text{W}}} (\cos \theta_{\text{W}}(1 + \beta^2) - 2\beta)\right]$

TABLE 2.1: Terms carrying the couplings and angular dependence of the Standard Model helicity amplitudes.

$C^{(\gamma)}(\lambda, s)$		$\frac{\Delta\kappa_\gamma}{s}$	$\frac{\lambda_\gamma}{s}$	
$C^{(Z)}(\lambda, s)$		$\frac{\cot\theta_{\text{WK}}\Delta g_Z^1(a-2b\lambda)}{(s-M_{\text{W}}^2)}$	$\frac{\cot\theta_{\text{WK}}\lambda_Z(a-2b\lambda)}{(s-M_{\text{W}}^2)}$	
$M_{\lambda_1\lambda_2}^{(D)}(s, \cos\theta)$	$\tau_1 = \pm 1$ $\tau_2 = \pm 1$	$\frac{1}{2}e^2s\lambda\sin\theta_{\text{W}}$	0	$\frac{e^2s^2\beta\lambda\sin\theta_{\text{W}}}{2M_{\text{W}}^2}$
	$\tau_1 = \pm 1$ $\tau_2 = \mp 1$	0		
	$\tau_1 = 0$ $\tau_2 = 0$	$\frac{1}{2}e^2s\beta\lambda\sin\theta_{\text{W}} \times$ $\left(1 + \frac{s}{2M_{\text{W}}^2}\right)$	$\frac{e^2s^2\beta\lambda\sin\theta_{\text{W}}}{2M_{\text{W}}^2}$	0
	$\tau_1 = 0$ $\tau_2 = \pm 1$	$\frac{e^2\sqrt{s^3}\lambda\beta}{2\sqrt{2}M_{\text{W}}}(\tau_2\cos\theta_{\text{W}} - 2\lambda)$		

TABLE 2.2: Terms carrying the couplings and angular dependence of the anomalous coupling helicity amplitudes.

and b , are given by

$$\begin{aligned} a &= \frac{4 \sin^2 \theta_{\text{WK}} - 1}{2 \sin 2\theta_{\text{WK}}}, \\ b &= \frac{-1}{2 \sin 2\theta_{\text{WK}}}, \end{aligned}$$

where θ_{WK} is the weak mixing angle.

Now, it can be seen that the cross-section is parabolic with each of the anomalous coupling parameters: the $C^{(D)}$ terms depend linearly on the coupling parameters (table 2.2); the helicity amplitudes, $F_{\tau_1 \tau_2}^{(\lambda)}$, in turn depend linearly on the $C^{(D)}$ terms (equation 2.29); and the W-pair production cross-section is proportional to the squared amplitude of the helicity amplitudes (equation 2.26). Hence, the W-pair production cross-section varies quadratically with the anomalous couplings. This quadratic form is an important property of the anomalous coupling cross-sections, utilised in many analyses.

As an example of the the importance of W-bosons' helicities in W-pair production, it may be seen from table 2.1 that the helicity amplitude for the case where the W-bosons have opposite helicities is given by

$$\begin{aligned} F_{\pm\tau\mp\tau}^{(\lambda)} &= C^{(\nu)}(\lambda, t) M_{\lambda\pm\tau\mp\tau}^{(\nu)}(s, \cos\theta_{\text{W}}) \\ &= \frac{2\lambda - 1}{4t \sin^2\theta_{\text{WK}}} (\cos\theta_{\text{W}} \pm 2\tau\lambda) \left(\frac{1}{2}e^2 s \lambda \sin\theta\right). \end{aligned} \quad (2.30)$$

As this final state has a total angular momentum of 2, it cannot arise through and intermediate photon or Z^0 boson; therefore, the only diagram which leads to this helicity state is the t-channel diagram. Note also that the $C^{(\nu)}(\lambda, t)$ term contains a factor of $(2\lambda - 1)$ ensuring that the neutrino exchange may only occur for an initial-state electron with negative helicity.

Furthermore, it can also be seen that the only terms which contribute in the limit of $\theta_{\text{W}} \rightarrow 0$ are those describing an LT final helicity state, i.e., with $\tau^\pm = 0$ and $|\tau^\mp| = 1$. This is reasonably intuitive; the initial state has an overall spin of 1 parallel to the beam-axis, so it is not possible to have a final state with spin of 2 or 0 parallel to the beam-axis, which would occur for the TT or LL final states respectively if θ_{W} was 0.

2.2.2 THE DECAY ANGLE CROSS-SECTION

It is not possible to directly measure the W-pairs; only their decay fermions are detected. Therefore, the relevant cross-section is not that of equation 2.26, but that relating to the final-state fermions. The decay distributions of these fermions are defined in the rest-frame of their parent particle, and are described by the decay angles, θ^* and ϕ^* ; these are, respectively, the polar and azimuthal angles in the basis given by

$$\hat{\mathbf{z}} = \frac{\mathbf{p}_{W^\pm}^{\text{CoM}}}{|\mathbf{p}_{W^\pm}^{\text{CoM}}|} \quad (2.31)$$

$$\hat{\mathbf{y}} = \frac{\mathbf{p}_{e^-}^{\text{CoM}} \times \mathbf{p}_{W^\pm}^{\text{CoM}}}{|\mathbf{p}_{e^-}^{\text{CoM}}| |\mathbf{p}_{W^\pm}^{\text{CoM}}|}, \quad (2.32)$$

where $\mathbf{p}_{W^\pm}^{\text{CoM}}$ and $\mathbf{p}_{e^-}^{\text{CoM}}$ are the momenta in the detector frame of the W^\pm boson and the electron beam respectively. For the W^- decay, the angles relate to the decay fermion, and, conversely, for the W^+ decay they relate to the antifermion. The angles and the basis in which they are defined are illustrated in figure 2.3.

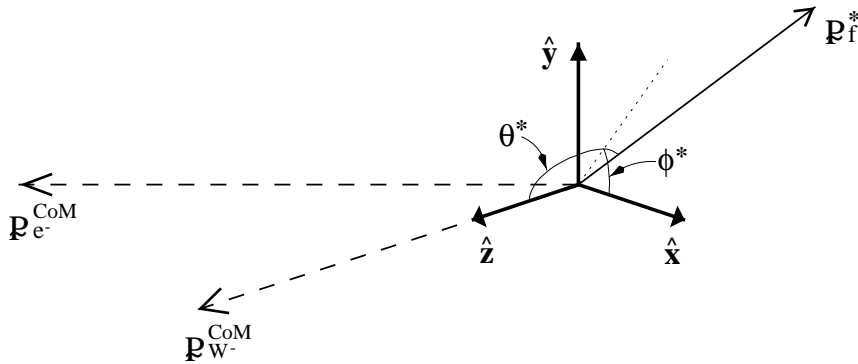


FIGURE 2.3: Schematic illustration of the decay angles, θ^* and ϕ^* , of a particle with momentum \mathbf{p}_f^* .

The production angle of the W boson, and the decay angles of the four-fermions form a set commonly referred to as the ‘‘T.G.C. angles’’; in terms of

these the differential cross-section is as follows:

$$\begin{aligned} \frac{d\sigma(e^-e^+ \rightarrow W^+W^- \rightarrow f_W\bar{f}_W.f_{W^+}\bar{f}_{W^+})}{d\cos\theta_W d\cos\theta_1^* d\phi_1^* d\cos\theta_2^* d\phi_2^*} = \\ Br(W^- \rightarrow f_W\bar{f}_W)(W^+ \rightarrow f_{W^+}\bar{f}_{W^+}) \frac{|\mathbb{R}|}{16\pi s\sqrt{s}} \left(\frac{3}{8\pi}\right)^2 \\ \times \sum_{\lambda\tau_-\tau'_-\tau_+\tau'_+} F_{\tau_-\tau_+}^{(\lambda)}(s, \cos\theta_W) F_{\tau'_-\tau'_+}^{(\lambda)}(s, \cos\theta_W) D_{\tau_-\tau'_-}(\theta_1^*, \phi_1^*) D_{\tau_+\tau'_+}(\theta_2^*, \phi_2^*). \end{aligned} \quad (2.33)$$

In equation 2.33, $Br(X \rightarrow Y)$ denotes the branching ratio for the process shown in parentheses (the actual branching ratios are given in §2.2.3), and $D_{\tau\tau'}(\theta^*, \phi^*)$ gives the decay angle distribution for each helicity combination, $\tau\tau'$. However, unlike in the W-pair cross-section, these helicities refer to a single W-boson. This is seen in the cross-section expression; the two indices on the helicity amplitudes $F_{\tau_-\tau_+}^{(\lambda)}$ —corresponding to different W-bosons—do not relate to a single angular term, $D_{\tau\tau'}(\theta^*, \phi^*)$. This means that it is not meaningful to consider any given 4-fermion final-state as having arisen from a single TT, LT, or LL helicity state. As a corollary, it is not possible to decompose this cross-section into three distinct cross-sections, $d\sigma^{TT}$, $d\sigma^{LT}$ and $d\sigma^{LL}$, unlike the case for the W-pair production cross-section. However, the decay angle distributions obey the relation

$$\int_{-1}^{+1} \int_0^{2\pi} D_{\tau\tau'}(\theta^*, \phi^*) d\phi d\cos\theta = 2\pi \frac{4}{3} \delta_{\tau\tau'} \quad (2.34)$$

so that equation 2.26 is recovered upon integration of equation 2.33 over the decay angles and summation over the different decay channels.

The distributions, $D_{\tau\tau'}(\theta^*, \phi^*)$ are central to the T.G.C. analyses as they are intimately connected to the helicity amplitudes; anomalous coupling strengths would change the values of the $C^{(D)}$ terms in the helicity amplitudes, which would, in turn, alter the relative contributions of these decay distributions. It is this change in the decay distributions and the production angle of the W bosons which T.G.C. analyses attempt to measure.

The variation of the W production angle and the decay angles of the fermions with T.G.C. strength values is shown in figure 2.4. The distributions

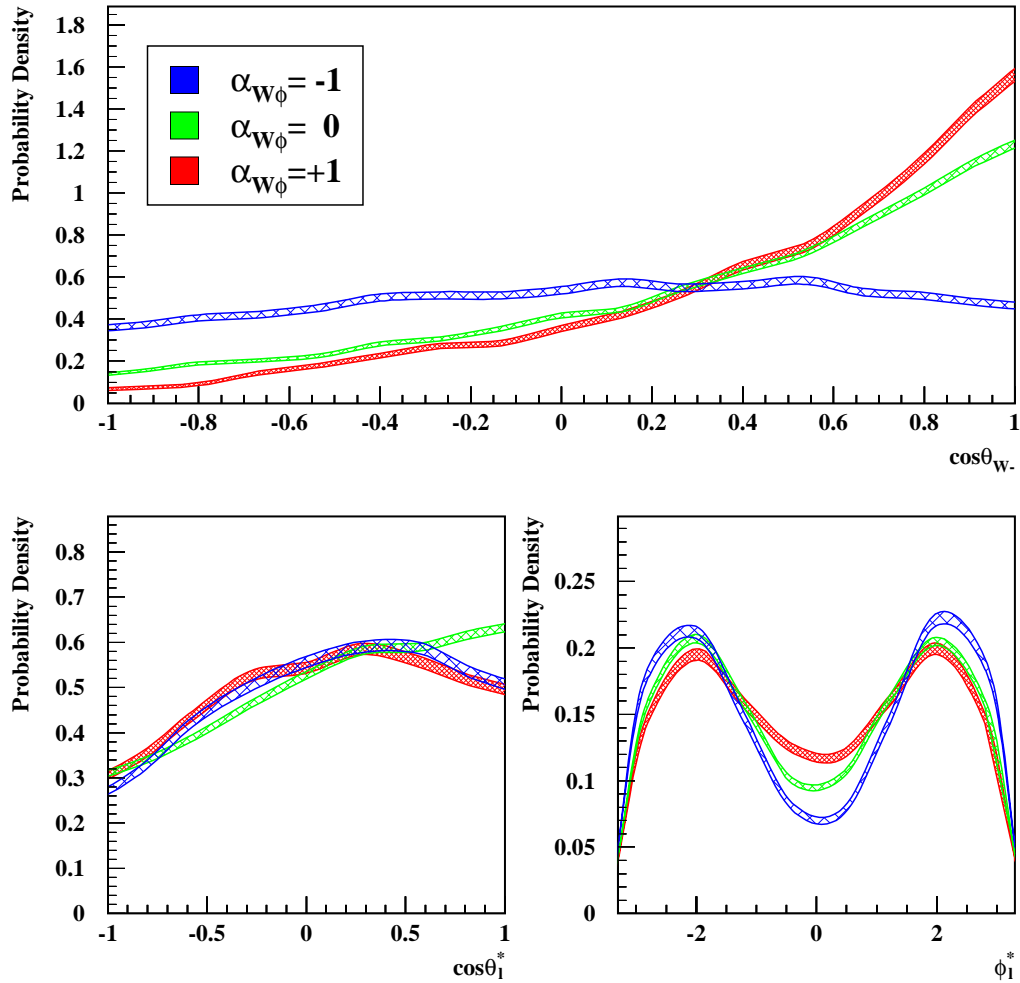


FIGURE 2.4: Plots of the W^- production angle and the decay angles taken from simulated Monte Carlo events. As with all such plots in this thesis, the width of the lines shows their statistical error; the distributions are not perfectly smooth due to the finite statistics of the Monte Carlo sample.

shown in this figure use events from the EXCALIBUR Monte Carlo generator (this and the `grc4f` generator, mentioned shortly, will be described in more detail in Chapter 4,§4.2.1).

2.2.3 OBTAINING THE T.G.C. ANGLES FROM THE DECAY FERMIONS

At this stage it is appropriate to consider how the possible final states from W-pair decays will be observed; this discussion is very general and neglects considerations of detector acceptance and resolution and, hence, is valid for any generic, multi-purpose detector.

Each W boson may decay either hadronically or leptonically. This gives three decay channels for W-pair production: $W^+W^- \rightarrow q'\bar{q}''q'''\bar{q}''''$, $W^+W^- \rightarrow q\bar{q}'l\nu_l$, & $W^+W^- \rightarrow l\nu_l l'\nu_{l'}$. The branching ratios for these channels are respectively 45.6%, 43.9% and 10.5%[14].

The production angle of the W^\pm pair is conventionally defined for the W^- boson, and the decay angles are defined for the fermion from W^- decays, and for the antifermion from W^+ decays. Ideally, it would be possible to know the charges and 4-momenta of each of the fermions, so that the five T.G.C. angles may be measured perfectly. Unfortunately, this is not possible in any of the channels.

HADRONIC W BOSON DECAYS

A hadronically decaying W boson produces two quarks which are observed as two jets of hadronic particles. The momentum of the jets will be well measured, but the charge must be inferred using a jet charge technique[21]; such a technique would at best have limited success for the combined system—where the overall charge must be ± 1 —but for an individual jet—where the overall charge must be $\pm \frac{1}{3}$ or $\pm \frac{2}{3}$ —it would be practically useless. This means that the modulus of the W production angle and the decay angles may be obtained very well, but the overall sign for the production angle would only be poorly ascertained, and for the polar decay angle, θ^* , it would be essentially unknown.

LEPTONIC W BOSON DECAYS

There are two slightly different situations for leptonic decays, depending on whether the charged lepton is a light lepton (i.e., an electron or muon) or a tau; the two cases will be described separately.

The former case is straight forward; there will be a single, well-measured charged track and missing 4-momentum corresponding to that of the neutrino. From the charge of the observed track, it should be possible to determine both whether the charged lepton was a fermion or antifermion, and also the charge of the parent W boson. This means that, unlike the hadronic case, the T.G.C. angles will only have a single solution.

However, if there is initial or final state radiation in the event the assumed 4-momentum of the neutrino will, effectively, be the sum of the

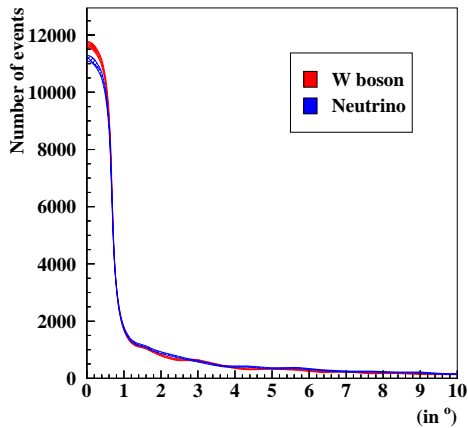


FIGURE 2.5: *The angle between the true and calculated momenta of the neutrino and W^\pm boson.*

tion for the W production angle.

As the charged lepton track will be well measured, there will be no problem in knowing which particle is the fermion and which the antifermion; this means

4-momenta of the neutrino and photon; this implies that the inferred direction of the combined charged lepton-neutrino momentum will not correspond precisely to that of the parent W boson. The extent of this effect is illustrated in figure 2.5, which were produced using simulated events generated with the `grc4f` Monte Carlo generator. The plot shows the angle between the momentum of the true neutrino and the missing momentum, and also the angle between the momenta of the true and inferred lepton systems, which is, effectively, an inherent finite resolution for the W production angle.

that, unlike in the hadronic case, there will be no ambiguity in the calculated decay angles. However, as the decay angles are defined in the W boson's rest frame they cannot be reconstructed perfectly because there will be a finite resolution on the 4-momentum of the W boson, due, again, to the uncertainty in the 4-momentum of the neutrino.

When the W boson decays to a tau and tau neutrino the situation is more complicated as taus are too short lived to be directly observed. In general, taus decay to one or three charged particles and at least one neutrino. This extra missing momentum means that the 4-momenta of the tau and tau-neutrino can only be reconstructed comparatively poorly, so neither the W production angle, nor the decay angles may be obtained as cleanly as from W boson decays to electrons or muons.

THE VARIABLE SET AND SIGNAL PROCESS

For the analysis in this thesis, only $q\bar{q}'l\nu_l$ final states where the charged lepton is an electron or muon are considered as the signal. In this channel the W production angle, $\cos\theta_W$, is best measured by calculating its modulus from the hadronic system and then deducing which solution refers to the W^- boson from the charge of the observed lepton. Only the leptonic decay angles are used, due to the ambiguity in the reconstructed hadronic decay angles. This gives a three variable parameter space of $\cos\theta_W$, $\cos\theta_l^*$ and ϕ_l^* .

DECAY ANGLES IN THE OTHER CHANNELS

The channel and variable set used in this analysis are the most sensitive to the T.G.C. strengths; for completeness, the reasons for the lower sensitivities in the other channels are outlined below.

In the $W^+W^- \rightarrow q'\bar{q}''q'''\bar{q}''''$ channel, the decay angles of both pairs of fermions have the reconstruction problems previously described. But, further-

more, it is also difficult to pair correctly the jets from a single W boson, and then difficult to determine the charge of that boson; this means that all of the T.G.C. angles in the hadronic channel will have considerably worse resolutions than those for the $W^+W^- \rightarrow q\bar{q}'l\nu_l$ channel.

For the $W^+W^- \rightarrow q\bar{q}'\tau\nu_\tau$ channel the reconstruction of the W production angle and the hadronic decay angles (which are not used in this analysis) should be no worse than for the signal channel. However, as discussed above, the leptonic decay angles will be significantly degraded.

The $W^+W^- \rightarrow l\nu_l l'\nu_{l'}$ channel also has problems in the lepton reconstruction, as well as having the lowest cross-section. Considering the simplest case where neither charged lepton is a tau, there are always two neutrinos in the final state, and their momenta cannot be calculated unambiguously; the components of their momenta transverse to the plane of the charged leptons' momenta must be equal and opposite (C.o.L.M.), but which neutrino has which component cannot be determined. This results in a two-fold ambiguity in the W production angle and in the azimuthal decay angle for each W boson. When one or both of the charged leptons are taus, their momenta are less well known, leading to an additional degradation in the reconstructed T.G.C. angles.

From this point onward, the terms $q\bar{q}'l\nu_l$, “lepton” and “neutrino” will only refer to electrons, muons, and their associated neutrinos.

CHAPTER 3

THE LEP COLLIDER AND OPAL DETECTOR

In the previous two chapters the motivation and framework for studying the T.G.C. parameters were discussed. In the following two chapters the means of analysing the events is described. This chapter details the LEP collider and the OPAL detector, and the next describes the selection algorithm for $W^+W^- \rightarrow q\bar{q}l\nu_l$ events.

3.1 THE LEP COLLIDER

The Large Electron-Positron[22] (LEP) collider is the largest synchrotron accelerator in the world, and is situated underneath France and Switzerland at CERN (*La Centre Européene pour la Recherche Nucléaire*). It was designed for the collision of electrons and positrons at centre-of-mass (\sqrt{s}) energies around the rest-mass energy of the Z^0 boson (91GeV), to investigate the neutral current interactions of the electroweak force. It ran at these energies from 1989 until 1995, at which time it was upgraded[14] to reach energies at which pairs of W^\pm bosons are produced, to allow the investigation of the charged current sector of the electroweak theory. In the first phase, it was desirable to collide at energies very close to the Z^0 boson mass, but in the latter phase it is desirable to achieve the highest energy possible with the collider, rather than simply running at the threshold energy for production of W-pairs (i.e.,

$2 M_W \simeq 161 \text{ GeV}$); this difference is because the cross-section for production of pairs of W^\pm bosons continues to rise up to roughly 200 GeV .

The LEP ring is 26.7 km in circumference which runs under France and Switzerland, between the Jura mountains and Geneva, $80\text{--}170 \text{ m}$ below the surface. The plane of the ring is inclined to the horizontal at 1.4° . The ring was designed to have the maximum possible radius of curvature, to minimize energy losses from synchrotron radiation. LEP consists of eight arcs, and four straight sections where the acceleration of the beams occurs and the experiments are located. Each of the arcs contain 31 magnetic cells, with a single cell having a length of 79.11 m . The accelerating sections consist of copper cavities and superconducting cavities which were installed for the LEP-II energy upgrade.

LEP is filled with electrons and positrons which are injected after having been passed through a series of CERN's older, smaller accelerators. The electrons are produced by thermionic emission; some of these are then collided with a tungsten target to produce the positrons. The remaining electrons and the positrons are then passed into the Proton Synchrotron (PS) accelerator, from there into the Super Proton Synchrotron (SPS) and then into LEP, having reached energies of 22 GeV . The arrangement of the three accelerators is shown in figure 3.1. To maintain the beams for as long as possible, it is necessary to maintain a high vacuum in the tunnel; without beams present the pressure is 10^{-12} Torr and this is degraded to 10^{-9} Torr with circulating beams (this is mainly due to outgassing due to synchrotron radiation striking the walls of the beampipe).

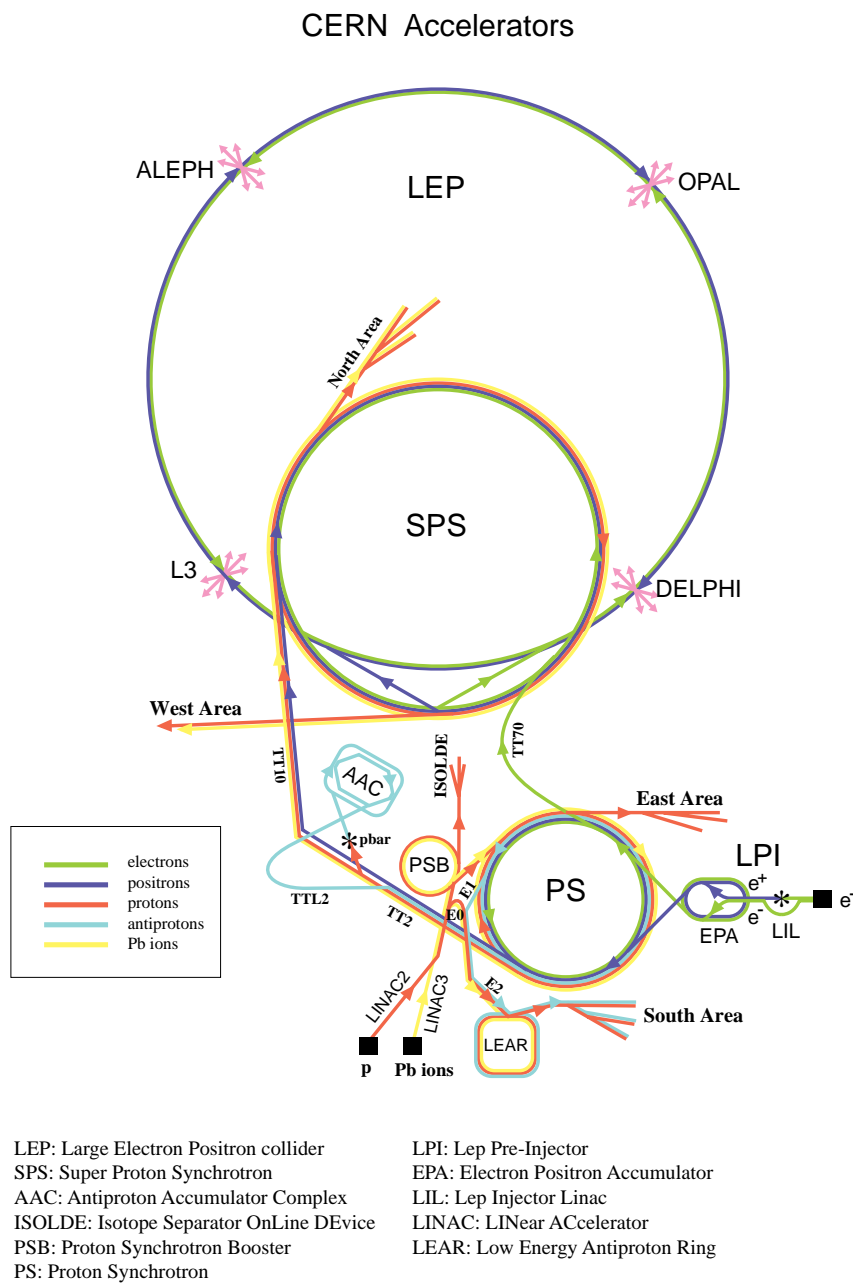


FIGURE 3.1: Schematic representation of the accelerators at CERN, showing how the smaller, older accelerators are used to provide the electrons and positrons.

3.2 THE OPAL DETECTOR

The electrons and positrons are brought into collision at points on the LEP ring where the four LEP experiments—ALEPH, DELPHI, L3 and OPAL—are situated.

Like the other LEP detectors, OPAL is a symmetric barrel detector[23]. A schematic diagram of OPAL is shown in figure 3.2. From this figure, the OPAL coordinate system can be seen; the z -axis is parallel to the beampipe, and is positive in the direction of the electrons' momentum, and the positive x -axis points to the centre of the LEP-ring. The origin is the nominal interaction point.

In this figure all the important features of OPAL can be seen. Roughly, it may be thought of as having vertex and tracking subdetectors in the centre, then the solenoid—to cause bending of the tracks in the tracking chambers—then calorimeters and finally the muon chambers. This is a simplification, not least because the arrangement in the flat ends of the detector (called the “endcaps”) is different from the central cylindrical section (the “barrel”). A detailed cross-section of the OPAL detector is shown in figure 3.3.

In the analysis presented in this thesis, both hadronic and leptonic W boson decays are analysed. The hadronic decays give the production angle of the W^\pm bosons, and information from both decays are needed to reconstruct the decay angles of the fermions. Hadronic W -boson decays are seen in the detector as jets of particles, which are measured by the central tracking chambers (referred to as CV, CJ and CZ) and by the calorimeters (EB and EE, and HB, HE and HP). A single charged particle is seen from a leptonically decaying W boson (excluding tau decays, which are not counted as part of the signal in this thesis). In order to identify the particle and measure its momentum and energy, the central tracking chambers and electromagnetic calorimeter and—for muon decays—the Muon Chambers (MB and ME) are used. The Forward Detectors and Silicon Microvertex subdetector are not used in this analysis, although they are described briefly for completeness.

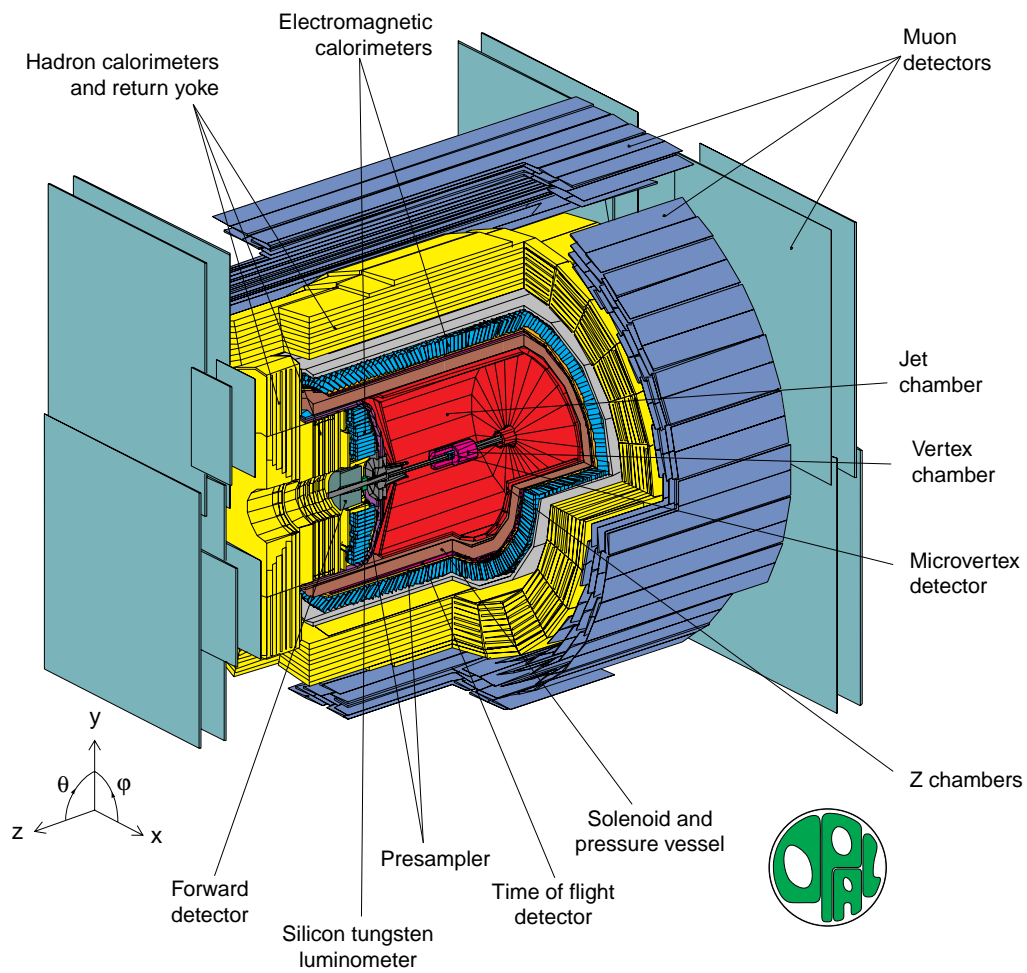


FIGURE 3.2: A schematic representation of the OPAL detector.

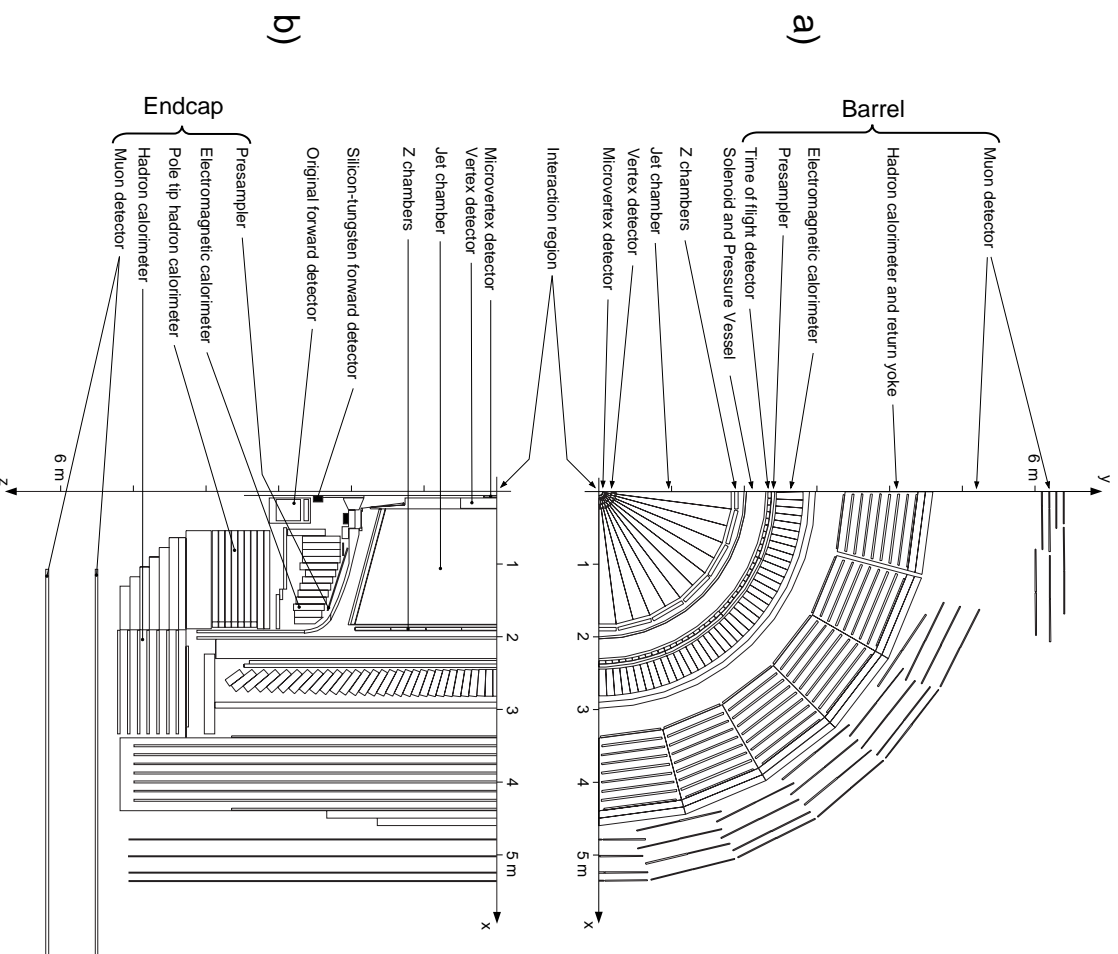


FIGURE 3.3: Cross-section diagrams of the OPAL detector, showing the positions of its subdetectors

3.2.1 TRACKING CHAMBERS

The tracking chambers are the innermost detectors, next to the beampipe. They allow for the measurement of interaction and decay vertices, momentum and charge of individual charged particles and their energy loss ($\frac{dE}{dx}$). The tracking chambers are comprised of the Silicon Microvertex Detector (SI), and the central tracking chambers, Central Vertex (CV), Central Jet (CJ) and Central Z (CZ).

SI—THE SILICON MICROVERTEX SUBDETECTOR

The SI detector[24] was installed in 1991 and upgraded in 1993. It was designed to give good measurement of interaction and decay vertices. It comprises two cylinders of radii 61mm and 75mm, with 12 ladders of silicon wafers on the inner cylinder and 15 on the outer. Each ladder has 5 wafers, each of which are 6cm×3cm in surface area, with readouts parallel to the beam axis every 50 μ m, and perpendicular to it every 100 μ m. The detector covers a range of $|\cos\theta| < 0.83$ and the resolution at the point of closest approach to the interaction point is 17 μ m in $r - \phi$, and 21 μ m in z .

CV—THE CENTRAL VERTEX CHAMBER

As with all of the Central Tracking drift chambers, CV[25] consists of chambers filled with a 88.2% : 9.8% : 2.0% mixture of argon, methane and isobutane through which run sense wires. The gas is at a pressure of 4 bar. A charged particle passing through the chambers will ionize the gas; the resultant electrons are accelerated toward the sense wire causing an avalanche effect and, hence, a current which is detected by the sense wires.

The CV chamber was the predecessor to SI in that it was designed to measure interaction vertex positions and gives a resolution of 55 μ m in $r - \phi$. It has an inner radius of 8.8cm and an outer radius of 23.5cm. It consists of two

systems of drift chambers; the inner contains axial sense wires whilst the outer chambers contain stereo sense wires, inclined at an angle of approximately 4 deg to the axial wires. The information from the inner and outer chambers together give a resolution on the position in z of a charged track of $700\mu\text{m}$.

CJ—THE CENTRAL JET CHAMBER

The Central Jet chamber[26] is one of the most important detectors in OPAL. It measures the trajectory of charged particles and, hence, their charge and momentum. Furthermore, the specific energy loss, $\frac{dE}{dx}$, of a particle is measured—aiding particle identification—by summing the charge received by the sense wires.

It is a cylindrical drift chamber, 4m long, consisting of 24 sectors separated by cathode wires. In each of the sectors 159 axial anode sense wires are arranged in radial planes. The trajectory of a particle is reconstructed from individual hits measured by the sense wire. The $r - \phi$ position of the hits is given by the radial position of the relevant wire and drift time, and the z -position is given by the difference between the signals at either end of the wire.

The resolution in the position is $135\mu\text{m}$ for $r - \phi$ and 6cm in z . The error on the momentum is given by

$$\frac{\sigma_p}{p^2} \sim 2 \cdot 10^{-3} \text{GeV}^{-1}. \quad (3.1)$$

CZ—THE CENTRAL Z CHAMBER

Outside of the CJ subdetector lie the 24 planar chambers which make up the Central Z subdetector[27]. As their name suggests, these chambers are intended to give a better measurement of a particles' position in the z -direction, and, hence, its sense wires run perpendicular to the beam pipe.

3.2.2 LOW-ANGLE SUBDETECTORS

The low-angle detectors are located next to the beampipe, but further out than the tracking chambers (much further out in the case of the Far Forward Monitors). The principal purpose of these detectors is to measure the luminosity that OPAL receives. This is done by identifying Bhabha events, for which the cross-section is very well known. In order to achieve a good measurement of the luminosity, the detectors must be at low enough angle that the statistics are high, and the acceptance of the individual detectors must be well measured. These subdetectors are also useful for the study of photon-photon interactions, and some are used to veto background events in searches for exotic particles.

FD—THE FORWARD DETECTOR

The Forward Detector[28, 29] itself consists of four subdetectors: the Forward Calorimeter, the Gamma Catcher, the Tube Chambers and the Far Forward Monitors.

The Forward Calorimeter is the main component of the Forward Detector; it is a lead scintillator sampling calorimeter, which contains 24 radiation lengths of material. The Gamma Catcher is a 7 radiation length lead scintillator ring, which was designed to cover the acceptance gap between the electromagnetic calorimeter and the Forward Calorimeter. The Tube Chambers consist of 3 layers of proportional tubes; two of which are mutually perpendicular, with the third at 45 deg to these. The tube chambers give a spatial resolution of 3mm. The Far Forward Monitors are pairs of lead scintillator calorimeters, positioned either side of the beam pipe at a distance of 7.85m from the interaction point.

SW—THE SILICON TUNGSTEN SUBDETECTOR

The Silicon Tungsten subdetector[30] was added to OPAL in 1993 to improve the luminosity measurement. They are sampling calorimeters, consisting of layers of tungsten with instrumented layers of silicon.

Apart from being used to measure the luminosity received by OPAL, none of the low-angle subdetectors are directly used in this analysis.

3.2.3 THE SOLENOID AND TIME OF FLIGHT COUNTERS

THE SOLENOID

The central tracking chambers are surrounded by the pressure vessel and solenoid. The purpose of the solenoid is simply to cause charged particles to move in a helical path, which allows measurement of their charge and momentum. OPAL's magnetic field is such that positively charged particles curl clockwise in OPAL's coordinate system and, conversely, negatively charged particles curl anticlockwise.

The solenoid itself is water-cooled and self-supporting. It provides a field of 0.435T.

TE & TB—TIME-OF-FLIGHT COUNTERS

Immediately outside the solenoid are the Time-of-Flight Counters, which measure the particles' flight time from the interaction point.

The TB subdetector consists of 160 trapezoidal scintillation counters at a radius of 2.360m. It provides coverage in the barrel region of the detector, and covers the range $|\cos\theta| < 0.82$; its time resolution is approximately 300ps. The timing information aids identification for particles with energy between

0.6 and 2.5 GeV, and also provides rejection of cosmic rays.

The TE[31] performs a similar function in the endcap region. It is made up of tiles of scintillator with embedded wavelength shifting optical fibre which reads out the signal to photomultiplier tubes. Installation of this subdetector first began in 1996, and was continued in 1997 to take the coverage closer to the beampipe, down to 43mrad. Its timing resolution is 3ns. This subdetector is particularly useful for the searches for exotic particle, and somewhat supersedes the Gamma Catcher (FE) subdetector in this respect.

3.2.4 THE CALORIMETERS

The calorimeters give the most important energy measurement for most particles. The calorimeters are arranged with the presampler and electromagnetic calorimeter in front, with the hadron calorimeter behind. This is for the simple reason that the hadronic particles tend to be more penetrating than the electrons and photons, which the electromagnetic calorimeter was principally designed to measure.

PE & PB—THE ELECTROMAGNETIC PRESAMPLER

The solenoid and the pressure vessel provide two radiation lengths, so that electromagnetic showering will have begun prior to the calorimeters. Because of this there is a presampler[32] to improve the resolutions of both the position and the energy. The presamplers work on the principal that the number of charged particles passing through the presampler is approximately equal to the amount of energy deposited in the previously traversed material.

The barrel presampler comprises 16 chambers containing two layers of streamer mode drift tubes. These chambers are positioned at a radius of 2.388m from the z-axis, and run a length of 6.623m, providing coverage over the range $|\cos\theta| < 0.81$. The endcap presampler is an arrangement of 32 thin

multiwire chambers operated in high gain mode. This presampler covers the range $0.83 < |\cos \theta| < 0.95$.

EE & EB—THE ELECTROMAGNETIC CALORIMETERS

Both the barrel and endcap electromagnetic calorimeters[33] consist of arrays of lead glass blocks; relativistic particles passing through the blocks emit Čerenkov radiation which is collected by photomultiplier tubes at the end of each block.

In the barrel region, there are 9440 blocks, each 37cm long (which gives 24.6 radiation lengths) and with a cross-section of approximately 10×10 cm. They are positioned at a radius of 2.455m and are oriented so that they point to a region between 55–158mm from the interaction point and 30mm from the z-axis; this geometry was used to prevent neutral particles from evading detection and gives coverage over $|\cos \theta| < 0.81$. In test beam conditions (i.e., with no material causing preshowers) the energy resolution of the barrel calorimeter was found to be

$$\frac{\sigma_E}{E} = 0.2\% + \frac{6.3\%}{\sqrt{E}}; \quad (3.2)$$

with preshowering, this resolution degrades by a factor of roughly 2, but half of this degradation is recovered by using the information from the presamplers.

The endcap calorimeter consists of 2264 blocks. In order for the subdetector to closely follow the domed shape of the pressure bell these blocks are of varying lengths (38cm, 420cm and 520cm, providing a minimum of 20.5 radiation lengths), and are aligned parallel to the z-axis. They provide coverage in the range $0.83 < |\cos \theta| < 0.95$. The energy resolution is approximately 1% in the energy region of 3–50GeV, which is the region relevant to the analysis presented in this thesis.

HP, HE & HB—THE HADRONIC CALORIMETERS

The hadronic calorimeter[34, 35, 36] consists of three units; the barrel and endcap calorimeters—as with the electromagnetic calorimeter—and also the “hadron poletip” calorimeter, which extends the coverage in the range $0.91 < |\cos \theta| < 0.99$, where the momentum resolution of the central detector grows worse.

The hadron calorimeter incorporates the iron return yoke for the magnetic field, which provides 4 or more interaction lengths over 97% of the total solid angle (the material traversed before reaching the hadron calorimeter provide another 2.2 interaction lengths). The calorimeters are planes of limited streamer chambers (for the barrel and endcap regions) or which are separated by 100mm thick layers of the iron yoke.

In the barrel region, there are 9 layers of detecting chambers separated by 8 layers of iron, which are located between radii of 3.39m and 4.39m; in the endcap region there are 8 layers of chambers and 7 of iron; in the poletip region there are 10 layers of chambers and 9 of iron. The iron layers are 100mm thick in the barrel and endcap regions and 80mm thick for the poletip; the gaps between the layers are 35mm, 25mm, and 10mm in the barrel, endcap, and poletip regions respectively. The gaps are made much smaller in the poletip region as the so as not to perturb OPAL’s magnetic field.

The chambers for each of the regions are limited streamer tube chambers; the barrel and endcap chambers are filled with a 75%:25% mixture of isobutane and argon and the poletip chambers are filled with a 55%:45% mixture of CO₂ and *n*-pentane. A particle passing through the a chamber ionizes the gas, causing charge to be deposited on the surfaces of the chamber; the charge is measured and read out by pads and strips which are located on the outer and inner surfaces of the chambers respectively.

The energy resolution of the combined detector varies depending on the

energy measured:

$$\frac{\sigma_E}{E} = \frac{100\%}{\sqrt{E}} \quad \text{for } E < 15\text{GeV} \quad (3.3)$$

$$\frac{\sigma_E}{E} = \frac{140\%}{\sqrt{E}} \quad \text{for } E \simeq 50\text{GeV}. \quad (3.4)$$

3.2.5 THE OUTER MUON DETECTORS

ME & MB—THE MUON CHAMBERS

The Muon Chambers are OPAL's outermost detectors and were principally designed, unsurprisingly, to detect muons. Any particle reaching them will have traversed roughly 1.3m of iron. This means that the probability of a pion—the particle which most closely resembles a muon in the detector—not having interacted before reaching the muon chambers is less than 0.1%.

In the barrel region[37] there are 110 drift chambers, which give coverage ranging from $|\cos\theta| < 0.68$ for four layers of chambers to $|\cos\theta| < 0.72$ for only one layer. This difference is due to the structural support for the detector. The chambers themselves are 1.2m wide and 900mm deep, and have a length of 10.4m, 8.4m or 6.0m. Each chamber consists of two cells, filled with a 90%:10% mixture of argon and ethane. An anode wire runs through each cell for the entire length of the chamber. Opposite the wire are readout pads, which measure the z-position to 2mm; the drift time gives the ϕ position to 1.5mm.

The endcap muon subdetector[38] is made up of four eight quadrant chambers and four patch chambers, as can be seen in figure 3.2. Each chamber consists of two layers of limited streamer tubes, aligned perpendicular to the beam axis with one layer vertical and the other horizontal. The chambers are filled with a 75%:25% mixture of argon and isobutane. The signal from the tubes is read out by strips of aluminium which are attached to the tubes perpendicular to the anode wire on one side and parallel to it on the other.

The coverage of the endcap muon chambers is $\sim 0.67 < |\cos \theta| < \sim 0.985$, and the spatial resolution is 3mm and 1mm respectively for the strips parallel and perpendicular to the anode wire.

3.2.6 THE TRIGGER

LEP typically provides a crossing rate of 45kHz; the vast majority of these crossings do not produce interesting events, and so should not be read out. The trigger[39, 40] provides a fast evaluation of an event, to determine whether it should be read out, and the data stored. The trigger will select an event either based on a single parameter—such as track multiplicity or transverse momentum—or else on a combination of the information from different sub-detectors in a single solid angle region. The 45kHz crossing rate is reduced to a rate of roughly 10Hz for events to be passed to the online data acquisition system.

3.2.7 DATA ACQUISITION

When the trigger selects an event the information from all of the sub-detectors is read out individually, combined and then passed to a filter[41]. Typically, 15–35% of all events selected by the trigger will be rejected by the filter. Assuming the event is not rejected, the information is then passed to the ROPE[42] (Reconstruction of OPAL Events) farm of HP UNIX workstations, which reconstructs the events using calibration constants from the individual subdetectors. After this reconstruction, the information is written to optical disk as a Data Summary Table (DST). Finally, this data is stored on tape and disk at the CERN's Meyrin site for offline analysis.

CHAPTER 4

EVENT RECONSTRUCTION AND DATA SELECTION

This chapter details the selection procedure applied to the events from the OPAL detector, which gives the data sample to be analysed. In order to describe the selection procedure it is first necessary to describe the different signal and background processes. The selection procedures used and their performances are slightly different for the 1997 & 1998 data sets, which were produced with different centre of mass energies; the differences in the procedures are small, and are detailed where relevant. The performances of the selections are summarised at the end of the chapter.

The details of the Monte Carlo samples used are given in Appendix A.

4.1 THE SIGNAL AND BACKGROUND PROCESSES

4.1.1 THE SIGNAL PROCESSES

THE PRINCIPAL SIGNAL: $W^+W^- \rightarrow q\bar{q}l\nu_l$

As mentioned in chapter 2, the main signal process—shown in figure 4.1—is W -pair production where one W -boson decays leptonically and the other hadronically. The two quarks each produce a high-multiplicity shower of par-

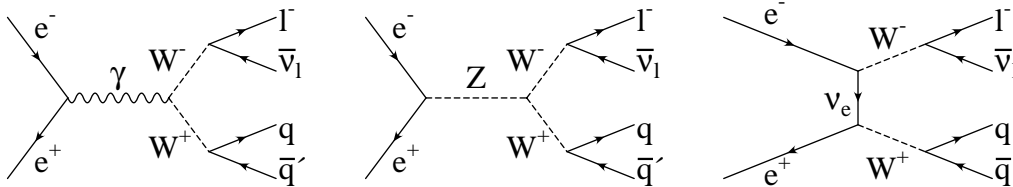


FIGURE 4.1: Feynman diagrams of the W -pair production leading to a $q\bar{q}'l\nu_l$ final state

ticles; the charged lepton will either be an electron or muon and, therefore, long lived; the neutrino, of course, is not directly observed but its presence is inferred through its missing 4-momentum.

Distributions of the fermions' energies from generator level Monte Carlo events are shown in figure 4.2. (Unless otherwise stated, all figures of

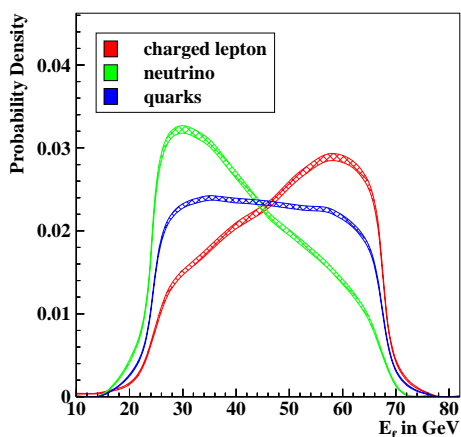


FIGURE 4.2: Energies of the fermions from $W^+W^- \rightarrow q\bar{q}'l\nu_l$ decays.

event distributions in this section show the generator level quantities from events generated at $\sqrt{s} = 183\text{GeV}$). As the decay fermions are all effectively massless, their energy spectra have similar means and limits. Distributions of their energies are roughly centred on a value of half E_{BEAM} , the beam energy, although there is a slight systematic shift downward due to initial state radiation (ISR); the spread in energy is due to the width and boost of the W bosons. The peaking in the energy spectra of the lepton and neutrino is due to forward peaking in $\cos\theta_l^*$ (defined in chapter 2), which leads to the charged lepton being preferentially boosted. This effect is not seen in the jet distributions as it is not possible to tell the fermion jet from the anti-fermion

jet.

The decay fermions from an individual W are reasonably well-separated, as shown in figure 4.3. And, in general, so are the fermions from different W s. Figure 4.3 shows the angular separation between the closest two fermions from different W bosons.

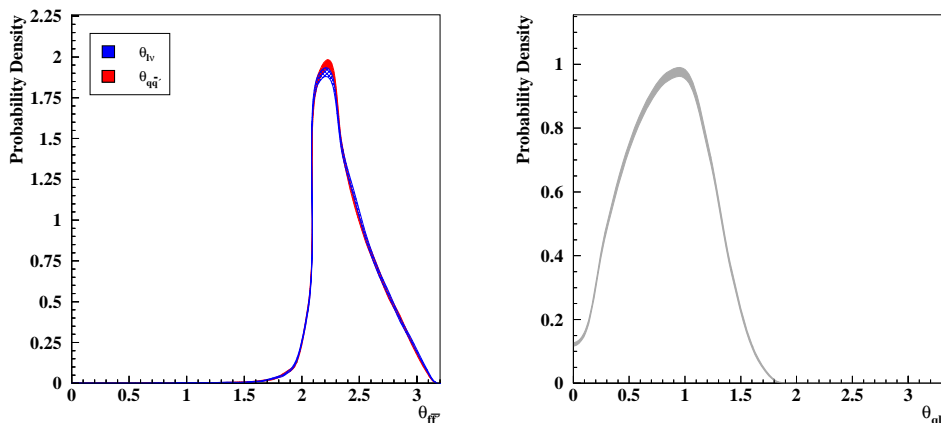


FIGURE 4.3: *The angular separation of fermions from $W^+W^- \rightarrow q\bar{q}'l\nu_l$ decays. The first plot shows that between the fermions from a single W boson; and the second, that between the two closest decay fermions from different W bosons.*

To summarise, the general $W^+W^- \rightarrow q\bar{q}'l\nu_l$ event shape has two high-multiplicity jets, an isolated charged lepton and missing 4-momentum.

NON-WW SIGNAL PROCESSES

As noted in chapter 1.2, the same $q\bar{q}'l\nu_l$ final state may also occur via diagrams other than the W pair production diagrams. As these diagrams lead to an identical final state, they will interfere with the W -pair production diagrams, and it is, therefore, appropriate to think of them as part of the signal.

Including the W -pair production diagrams, there are 20 leading order diagrams which give rise to a $q\bar{q}'e\nu_e$ final state and 10 to a $q\bar{q}'\mu\nu_\mu$ (or $q\bar{q}'\tau\nu_\tau$) final state; they are often referred to as “CC20” and “CC10”, respectively, where the prefix, CC, indicates that they involve charged currents. The CC10 diagrams may be regarded as being a subset of the CC20 diagrams, and, similarly, the W -pair production diagrams form a subset of them, referred to as “CC3”. Representations of all the diagrams are shown in figure 4.4. The 10 extra $q\bar{q}'e\nu_e$ diagrams arise through quasi- t -channel processes, and so may be thought of as being due to the colliding beams comprising electrons.

The $We\nu_e$ diagram, introduced in chapter 2, is the final diagram in figure 4.4. As previously mentioned, these diagrams contain the trilinear gauge vertices (although in practise it is only the diagram with the $WW\gamma$ vertex which contributes at LEP2 energies). In addition to this, the interference terms between the TGC-dependent diagrams and any other diagram will also depend on the coupling strengths. It is, therefore, important to consider these diagrams and their interferences when attempting to measure the T.G.C. strengths.

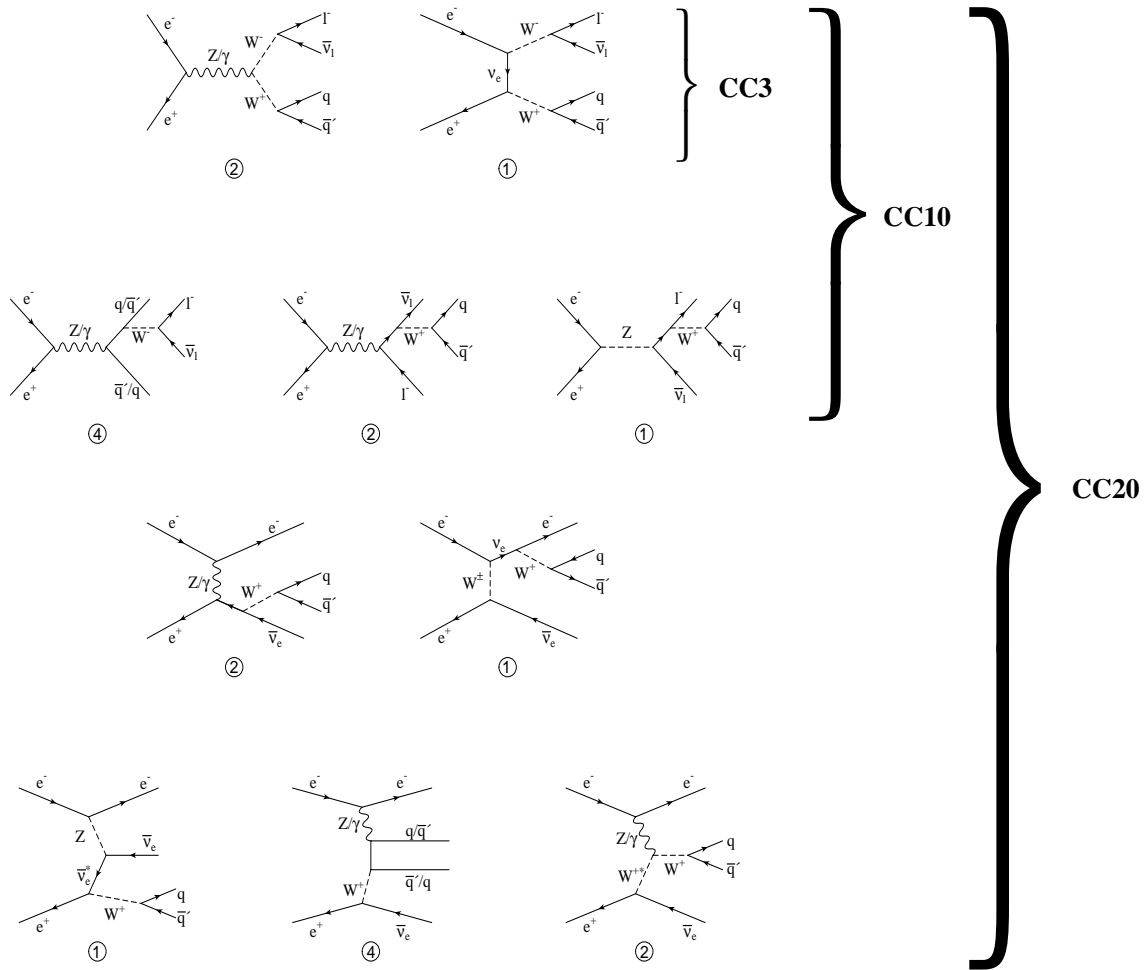


FIGURE 4.4: Pseudo-Feynman diagrams of the leading order charged current processes which give rise to a $q\bar{q}'l\nu_l$ final state. The number of true diagrams represented is given by the number underneath. For any multi-diagram representation, the extra diagrams are obtained through interchange of quark/antiquark pairs (denoted by q/\bar{q}' and \bar{q}'/q) or neutral current particles (denoted by Z^0/γ).

4.1.2 BACKGROUND PROCESSES

Given the nature of the signal events, contamination in the data sample must be anticipated from all high-multiplicity processes. Broadly, there are two main types: those which genuinely resemble the signal final state, and those that are generally dissimilar from the signal, but still contaminate the sample due to a high production rate. In the first class are misidentified $q\bar{q}'l\nu_l$ events and the neutral-current 4-fermion processes, and in the second are two-photon processes and fermion-pair production via Z^0/γ exchange.

MISIDENTIFIED CHARGED CURRENT EVENTS

The majority of events in this category are from $W^+W^- \rightarrow q\bar{q}'\tau\nu_\tau$ usually with the τ decaying leptonically. In addition to this, there is also a small accepted cross-section for cross-contamination, where true $q\bar{q}'e\nu_e$ events are accepted as $q\bar{q}'\mu\nu_\mu$ and vice versa. This latter case is negligible compared to the contribution from $W^+W^- \rightarrow q\bar{q}'\tau\nu_\tau$ events.

NEUTRAL CURRENT FOUR-FERMION PRODUCTION

Neutral current diagrams, shown in figure 4.5, give rise to $f\bar{f}f'\bar{f}'$ final states. There are 48 diagrams which contribute to the $e^-e^+q\bar{q}$ final state, and, of those, 24 may give rise to a $q\bar{q}\mu^-\mu^+$ or $q\bar{q}\tau^-\tau^+$ final state. The full set of NC diagrams is shown in figure 4.5. The 3rd diagram represents the production of pairs of Z^0 bosons which only becomes significant with \sqrt{s} above $\sim 183\text{GeV}$. This is regarded as an important background process, as it is almost indistinguishable from $q\bar{q}'l\nu_l$ if one of the leptons is not detected. The 5th diagram is the purely electrodynamic two-photon process; this is only a small contribution to the total two-photon cross-section, as it does not contain the hard QCD subprocess which is crucial for correct modelling of two-photon interactions.

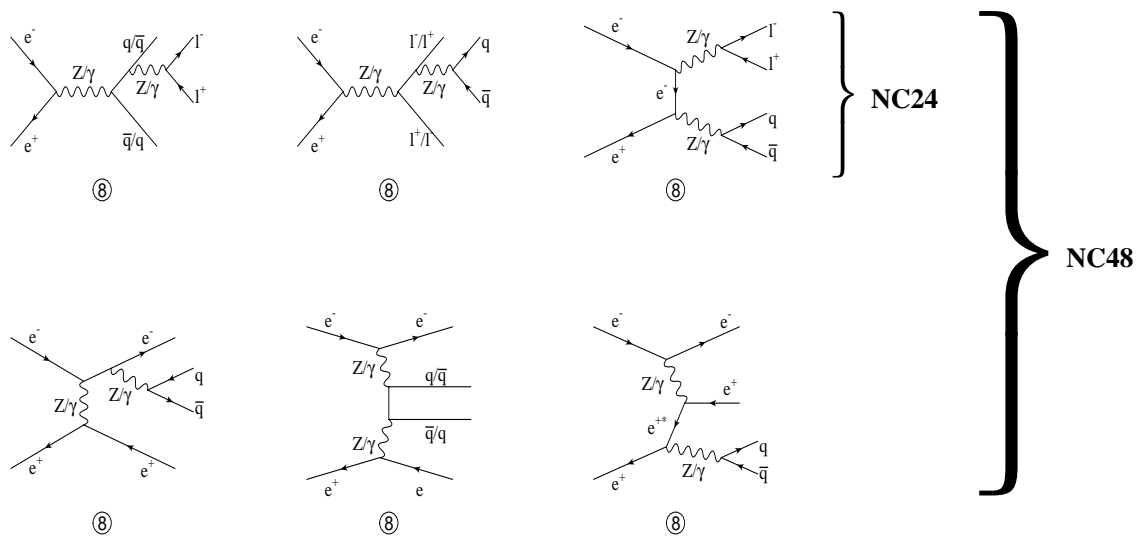


FIGURE 4.5: Pseudo-Feynman diagrams of the leading order neutral current processes which give rise to a $l^+l^-q\bar{q}$ final state. The number of true diagrams represented, shown underneath each diagram, are obtained as in figure 4.4.

THE 2-PHOTON BACKGROUND

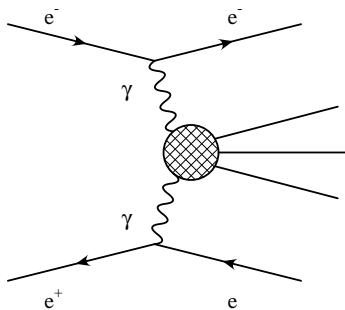


FIGURE 4.6: *The 2-photon interaction.*

The 2-photon process is shown in figure 4.6. There are two main types of 2-photon event: “untagged”, where both beam electrons are lost down the beam lines, and “tagged”, where one of the beam electrons (the “tag”) is detected. Only the tagged events give any contribution to the background as the tag may resemble the electron in $q\bar{q}'l\nu_e$ events. Generally, the invariant mass of the hadronic system in these events is very low compared with that of the signal but the process has a very high cross-section, so unusual events may be accepted. This is probably the least understood of

all the $W^+W^- \rightarrow q\bar{q}'l\nu_l$ background processes, as the events which resemble the signal process are not well modelled at present. Fortunately, it is a relatively small background, and does not contribute a large systematic error.

THE Z^0/γ BACKGROUND

The Z^0/γ background (shown in figure 4.7), is, in general, dissimilar from the signal process. However, its cross-section is approximately 25 times larger than the signal’s, and so atypical event shapes may contribute to the accepted background. Frequently the photon is radiated with such an energy that the Z^0 is on-shell. This means that the jets produced will be boosted and will also have a similar invariant mass to jets from W-decay. If, in addition, a track from one of the jets resembles a lepton candidate the event will look reasonably sim-

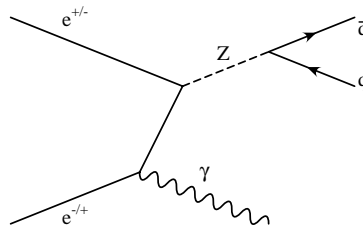


FIGURE 4.7: *Radiative $f\bar{f}$ production.*

ilar to the signal process. Alternatively, the initial state photon may convert to an electron-positron pair, one of which may resemble a lepton candidate.

4.2 THE MONTE CARLO SAMPLES

The expected accepted levels of signal and background are evaluated using Monte Carlo generated events which have been processed by GOPAL[43], the OPAL detector simulation package which is based on GEANT[44]. Several different Monte Carlo generators are used, as appropriate to the process being evaluated. Apart from the HERWIG [45] generated samples, all the samples have jet fragmentation by JETSET [46]; the HERWIG samples use the HERWIG fragmentation routines.

4.2.1 THE FOUR-FERMION SIGNAL AND BACKGROUND PROCESSES

The `grc4f` [47] generator is used to generate samples of the Standard Model CC3 process and of the full four-fermion processes; EXCALIBUR [48] is used to generate similar samples, but with anomalous coupling strengths. Both can generate events using all of the CC20 and NC48 diagrams or a subset of them. In practise, the QED 2-photon diagram is omitted as its behaviour is better modelled by dedicated 2-photon generators. This means that its interference terms with the other NC48 diagrams are neglected, but, from phase-space considerations, this is expected to be a small effect; it should certainly be small compared with the uncertainty associated with the total 2-photon process.

It is standard for (at least) two separate 4-fermion samples to be generated, one including $e^-e^+\bar{f}f$ final states, and the other with all other diagrams. This is because the $e^-e^+\bar{f}f$ final states have a large cross-section compared with the other 4-fermion diagrams due to the t-channel events with soft photons. It should be noted that the two categories used for event generation are not the same as the CC and NC classes of the 4-fermion processes. For the evaluation of the selection at $\sqrt{s} = 183\text{GeV}$ two samples of $e^-e^+q\bar{q}$ and $e^-e^+\tau^-\tau^+$ events

were used; for that at $\sqrt{s} = 189\text{GeV}$, two samples with combined $e^-e^+q\bar{q}$ and $e^-e^+\tau^-\tau^+$ final states but separated into s-channel and t-channel production diagrams were used. The 189GeV samples neglects some interference effects between the two channels, but this is expected to be insignificant compared with the statistical error.

In addition to the four-fermion generators, others such as KORALW [49] and PYTHIA (see next section) are also used to generate CC3 events. These are used principally for tuning and testing the selection algorithm and for the evaluation of systematic errors in the modelling of the signal event shape.

4.2.2 OTHER BACKGROUND PROCESSES

The $Z^0/\gamma \rightarrow q\bar{q}$ background is simulated by the PYTHIA [50, 51] and HERWIG generators. PYTHIA is a widely-used generator which was designed to simulate collisions between e^+e^- , pp and ep particles to produce multiparticle final-states.

Modelling of the 2-photon background requires dedicated generators, because, as alluded to previously, the full 2-photon process involves QCD interactions of low-virtuality photons and is not well understood, particularly in the regions of phase-space from where the accepted events originate. Unlike the other processes studied it is not well modelled by applying hadronization to final-state fermions. The background samples used were generated by PHOJET [52] and HERWIG.

4.3 SELECTING THE DATA SAMPLE — THE WW AND WV UTILITY PACKAGES

The WW package[53] consists of a set of utility routines which perform a wide variety of tasks, principally for study of W -pair production events. Using its routines, individual tracks and clusters are selected and associated to form events which are then categorized using relative likelihood functions.

The WV package[54] is complimentary to WW, and oriented specifically for studies of the triple gauge vertex couplings. WV routines perform kinematic fits on selected events and calculate the T.G.C. angular variables.

4.3.1 EVENT RECONSTRUCTION

The first stage in the reconstruction is to combine the information from OPAL's subdetectors into an event. The data from OPAL are stored as clusters from the calorimeters and individual hits which form tracks in the jet chambers. Quality cuts are performed on these raw data to ensure that only well-measured data are analysed.

4.3.2 THE LIKELIHOOD EVENT SELECTION

The selection[56] for $W^+W^- \rightarrow q\bar{q}'e\nu_e$ and $W^+W^- \rightarrow q\bar{q}'\mu\nu_\mu$ events is performed in four steps:

- Identification of a lepton candidate.
- Loose preselection cuts.
- Application of a likelihood function on 10 variables.

- Event categorization.

These form the WW selection routine which is developed by the OPAL W mass and W-pair cross-section groups.

The ideal event selection for a T.G.C. analysis differs from that for the analyses of the W-mass and W-pair cross-section in two main respects: i) the cross-section measurement only uses the number of events selected, and, therefore, does not require accurate measurements of the event kinematics; T.G.C. studies need events with the correct lepton candidate and well-measured hadronic jets; ii) the mass analyses tend to avoid using any cuts which are correlated with the mass of the reconstructed W particles as this would introduce a bias into the measured value; TGC studies should not be sensitive to such a bias, and are free to improve the data sample through the use of mass-based cuts. Therefore, both to improve the quality of the signal events in the data sample and to reject more of the background, additional hard cuts are applied for T.G.C. studies (these are described in §4.3.3).

IDENTIFICATION OF THE LEPTON CANDIDATES

Two lepton candidates are selected for each event, one as the best electron candidate and one as the best muon, no matter how improbable they each are. The selection of these candidates does not require explicit lepton identification, but instead uses a multivariate likelihood function. The likelihood function is based upon direct comparison with Monte Carlo-generated, high statistics histograms; two sets of histograms are used—one for each flavour of lepton candidate. The variables used in the likelihood function are as follows: the energy loss of the track through the tracking chambers ($\frac{dE}{dx}$); the energy deposited in the electromagnetic calorimeter; the number of hits in the hadron calorimeter; and the number of hits in the muon chambers.

A likelihood is calculated for each track in the event by multiplying the probabilities for each variable, obtained from the reference histograms. This is performed for both sets of reference histograms giving L_e , the likelihood that

the track arose from an e^\pm , and L_μ , the likelihood that it arose from a μ^\pm . The two tracks with the highest values of L_e and L_μ are taken as the electron and muon candidates respectively. No events are rejected at this stage.

PRESELECTION CUTS

The preselection is comprised of a set of loose cuts, which are designed to eliminate events which are clearly not $W^+W^- \rightarrow q\bar{q}l\nu_l$. It succeeds in removing almost all 2-photon events from the sample and most $Z^0/\gamma \rightarrow q\bar{q}$ events.

The preselection is comprised of the following cuts. Unless stated, the preselection cuts are the same for the 183GeV and 189GeV selections.

- General cuts:

- ◊ $N_{CT} > 7$ —the number of tracks in the central tracking chambers.
- ◊ $N_{EC} > 5$ —the number of ECAL clusters.
- ◊ $0.3 < R_{vis} < 1.2$ —the fractional visible energy in the event.
- ◊ $E_{lepton} > 10\text{GeV}$ —the energy of the candidate lepton. This is calculated using the electromagnetic calorimeter energy for electrons and using the track momentum for the muons.
- ◊ $L_e > 10^{-9}$ —the selection likelihood for the electron candidate.

OR

$L_\mu > 10^{-8}$ at $\sqrt{s} = 183\text{GeV}$, $L_\mu > 10^{-9}$ at $\sqrt{s} = 189\text{GeV}$ —the selection likelihood for the muon candidate.

- Cuts to remove $Z^0/\gamma \rightarrow q\bar{q}$ events:

- ◊ $E_\gamma < ((\sqrt{s} - M_{Z^0}) - 10 (\simeq 88\text{GeV}))$ —energy of most energetic isolated photon. Note that the quantity $(\sqrt{s} - M_{Z^0})$ is equal to the energy of a single initial state photon such that the collision energy of the event is that of the mass of an on-shell Z^0 boson.

- ◇ $E_{FD} < 40\text{GeV}$ at $\sqrt{s} = 183\text{GeV}$, $E_{FD} < ((\sqrt{s} - M_{Z^0}) - 10\text{GeV})$ at $\sqrt{s} = 189\text{GeV}$ —the energy in the calorimeters of the low angle subdetectors. The cut at $\sqrt{s} = 189\text{GeV}$ is essentially the same as the previous E_γ cut, but specific to the Forward Detectors, which are otherwise generally not used in the analysis.
 - ◇ $\cos\theta_{L_{\text{PMIS}}} < 0.9$ —the cosine of the angle between the lepton track and the direction of the missing momentum.
 - ◇ $P(\sqrt{s'}) < 0.01$; the probability obtained in a kinematic fit to find $\sqrt{s'}$. This cut is only applied if the lepton candidate appears to have originated from conversion of a photon, and the kinematic fit converged.
- Cuts to remove $Z^0/\gamma \rightarrow q\bar{q}$ events, applied only in the $q\bar{q}'e\nu_e$ channel if the energy of the electron candidate is within 12GeV of $(\sqrt{s} - M_{Z^0})$, in order to exclude events where an initial state photon converts to an electron-positron pair:
 - ◇ The event is rejected if the track of the lepton candidate and an oppositely charged track appear to have originated from conversion of a photon.
 - ◇ $5 < \frac{dE}{dx} < 15\text{keV cm}^{-1}$; the energy loss of the particle in the tracking chambers. The event will also be rejected if $\frac{dE}{dx}$ is not well-measured.
 - ◇ $|\mathbf{p}_e| > 10$; the scalar momentum of the electron. This cut is only applied if the electron is within $\sim 32^\circ$ of the beampipe.
- The following cut is intended to remove tagged two-photon events:
 - ◇ $\sqrt{s'} > 50\text{GeV}$ at 183GeV , $\sqrt{s'} > 60\text{GeV}$ for the $q\bar{q}'e\nu_e$ selection and $\sqrt{s'} > 90\text{GeV}$ for the $q\bar{q}'\mu\nu_\mu$ selection at 189GeV . $\sqrt{s'}$ is the estimated invariant mass of the incident electron-positron system (i.e., omitting any clusters or tracks assumed to be due to initial state photons).

- The following cut is intended to remove tagged two-photon events in the $q\bar{q}'e\nu_e$ channel:
 - ◇ $\cos\theta_{mis} \lesssim \pm 0.975$; the cosine of the polar angle of the missing momentum. This cut is intended to reject 2-photon events where the missing momentum is actually due to the antitag; hence the cut value is positive or negative depending on whether the lepton candidate is selected as a positron or electron respectively.

The preselection is approximately 90% efficient for the signal events. Plots of some of the preselection variables showing the cut values are given in figure 4.8.

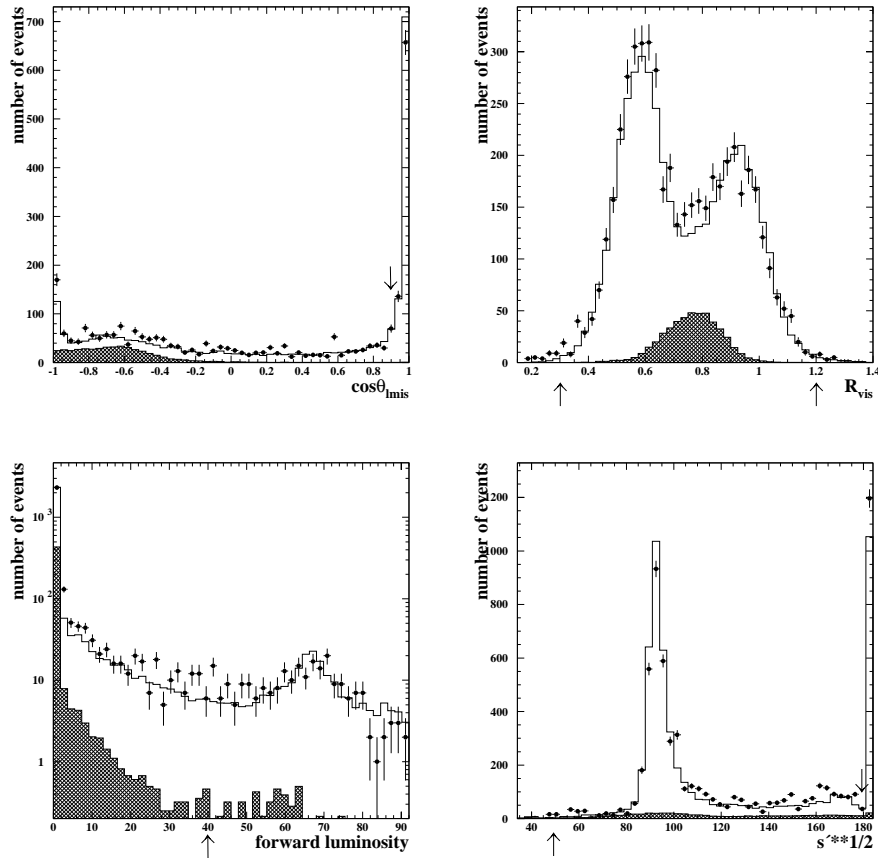


FIGURE 4.8: Distributions of some of the variables used in the preselection of the $q\bar{q}'l\nu_l$ selection algorithm of the WW package. The points are the 183GeV data, the hatched histogram is the simulated W-pair signal (increased fourfold for clarity), and the open histogram is the sum of the simulated signal and background from $Z^0/\gamma \rightarrow q\bar{q}$ and four-fermion processes. The preselection cuts are indicated by arrows pointing to the x-axis.

RELATIVE LIKELIHOOD SELECTION

The main likelihood selection uses the following variables:

- R_{vis} ;
- $\cos \theta_{l_{mis}}$;
- $\cos \theta_{mis}$;
- $\sqrt{s'}$;
- $P(\sqrt{s'}) < 0.01$;
- L_e or L_μ ;
- $\cos \theta_{lq}^{\text{MIN}}$ —the smaller of the angles between the lepton candidate and each of the two jets.
- $\cos \theta_{qmis}^{\text{MIN}}$ —the smaller of the angles between the missing momentum and each of the two jets.

Some examples of the simulated distributions of these variables are shown in figure 4.9; the difference in the distributions of R_{vis} and $\cos \theta_{l_{mis}}$ after the preselection cuts may be seen by comparison with figure 4.8. Likelihoods are formed from these variables in the same way as for the identification of the lepton candidates. Three likelihoods are calculated for each event; $L^{\text{q}\bar{\text{q}}'e\nu_e}$ and $L^{\text{q}\bar{\text{q}}'\mu\nu_\mu}$ the likelihood that it is a $W^+W^- \rightarrow \text{q}\bar{\text{q}}'e\nu_e$ or $W^+W^- \rightarrow \text{q}\bar{\text{q}}'\mu\nu_\mu$ event, and $L^{\text{q}\bar{\text{q}}}$, that of it being a $Z^0/\gamma \rightarrow \text{q}\bar{\text{q}}$ event. $Z^0/\gamma \rightarrow \text{q}\bar{\text{q}}$ events are singled out as they form the largest background contribution (excluding $W^+W^- \rightarrow \text{q}\bar{\text{q}}'\tau\nu_\tau$, addressed in the Event Categorisation). The relative likelihood (for the $\text{q}\bar{\text{q}}'e\nu_e$ selection in this case) is then

$$\mathcal{L}^{\text{q}\bar{\text{q}}'e\nu_e} = \frac{L^{\text{q}\bar{\text{q}}'e\nu_e}}{L^{\text{q}\bar{\text{q}}'e\nu_e} + f \times L^{\text{q}\bar{\text{q}}}},$$

where f is the estimated ratio of preselected background to signal cross-section, evaluated using simulated event samples. This relative likelihood has little

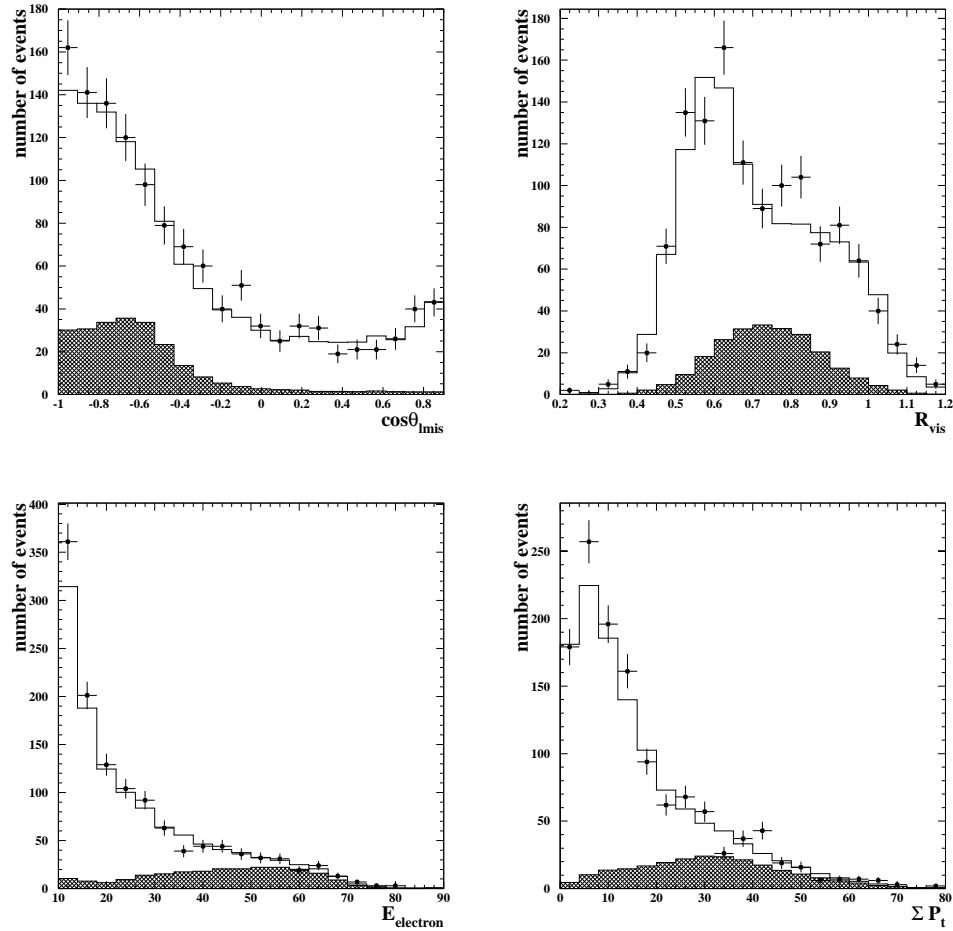


FIGURE 4.9: Distributions of some of the variables used in the relative likelihood function of the $q\bar{q}'l\nu_l$ selection algorithm of the WW package. The points are the 183GeV data, the hatched histogram is the simulated W-pair signal, and the open histogram is the sum of the simulated signal and background from $Z^0/\gamma \rightarrow q\bar{q}$ and four-fermion processes.

meaning, but is chosen simply as it is a good discriminator in such algorithms where it is assumed that there are two possible outcomes, each with a known probability. Any events with $\mathcal{L}^{q\bar{q}'e\nu_e} > 0.5$ or $\mathcal{L}^{q\bar{q}'\mu\nu_\mu} > 0.5$ are selected as $q\bar{q}'e\nu_e$ or $q\bar{q}'\mu\nu_\mu$ respectively. If two (or more) relative likelihoods give a value of

greater than 0.5, new likelihoods are calculated using a subset of the original variables to discriminate between the two cases.

Plots of the relative likelihood distribution for $q\bar{q}'e\nu_e$ and $q\bar{q}'\mu\nu_\mu$ events are given in figure 4.10

The only difference between this section of the selection for the 183 GeV and 189 GeV data samples is the distributions used to form the likelihoods; the same variables are used.

EVENT CATEGORISATION

The relative likelihood selected sample will also select many $q\bar{q}'\tau\nu_\tau$ events so new relative likelihoods, corresponding to different τ decay modes, are calculated for each event. The same variables as in the first relative likelihood selections are used. The expressions used are exactly analogous to the previous expression; for any particular decay mode there is a relative likelihood function such as

$$\mathcal{L}^{q\bar{q}'\tau\nu_\tau} = \frac{L^{q\bar{q}'\tau\nu_\tau}}{L^{q\bar{q}'\tau\nu_\tau} + f' \times L^{q\bar{q}'l\nu_l}}$$

Any event with $\mathcal{L}^{q\bar{q}'\tau\nu_\tau} > 0.5$ in any mode is reclassified as a $q\bar{q}'\tau\nu_\tau$ event, and is removed from the $q\bar{q}'e\nu_e$ or $q\bar{q}'\mu\nu_\mu$ event sample.

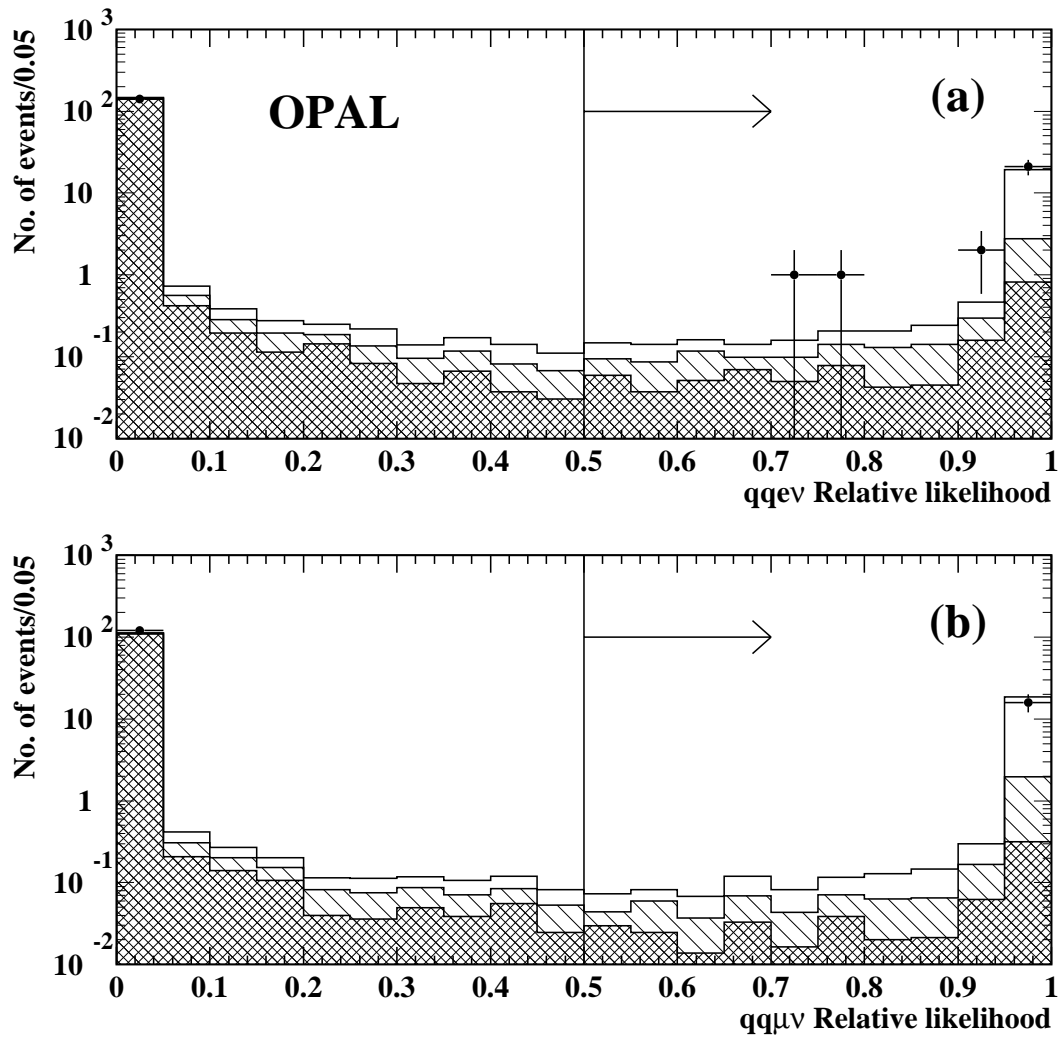


FIGURE 4.10: *Distribution of the relative likelihood for the selection of $q\bar{q}'e\nu_e$ and $q\bar{q}'\mu\nu_\mu$ events. The unhatched histogram shows the relative likelihood obtained from CC3 signal events; the singly hatched histogram shows that from $q\bar{q}'\tau\nu_\tau$ events; and the doubly hatched histogram shows that from the other background processes.*

EXAMPLES OF EVENTS SELECTED BY THE WW LIKELIHOOD SELECTION

Figures 4.12 and 4.11 show two events selected by the likelihood selection, displayed using GROPE [57], the graphical tool for displaying information from OPAL's subdetectors. The first of these events is selected as a $q\bar{q}'\mu\nu_\mu$ event at $\sqrt{s} = 183\text{GeV}$ and the other was selected as a $q\bar{q}'e\nu_e$ event at $\sqrt{s} = 189\text{GeV}$. The $q\bar{q}'\mu\nu_\mu$ event is viewed from the side of the detector so that hits in the endcap subdetectors are visible, whilst the $q\bar{q}'e\nu_e$ is viewed from one end of the detector. In these plots, the orange arrow represents the direction of the missing momentum; the other coloured lines in the central region represent the tracks left by charged particles in the tracking chamber; the yellow and pink blocks represent the energy deposited in the electromagnetic and hadronic calorimeters respectively; and the red arrow represents hits in the muon chambers.

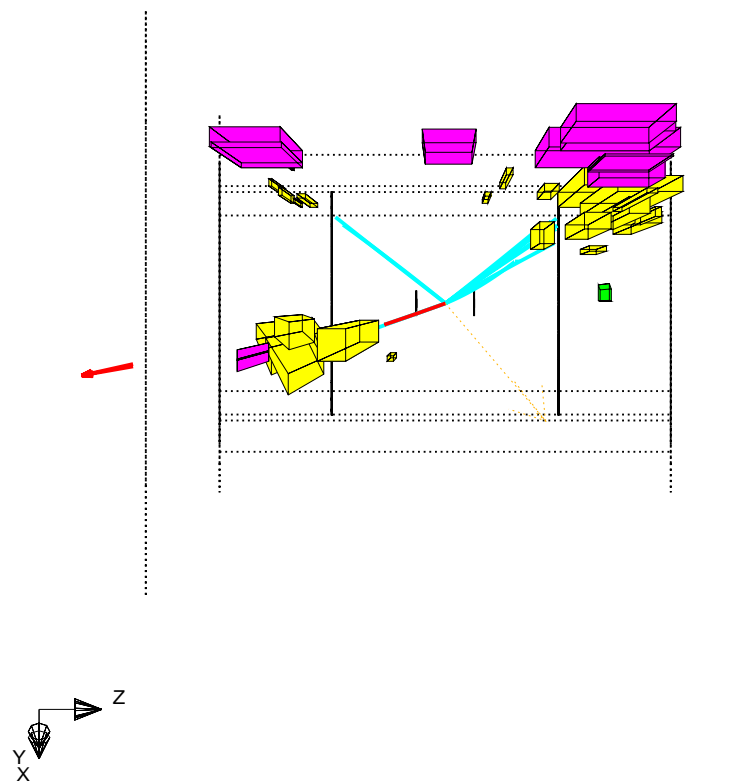
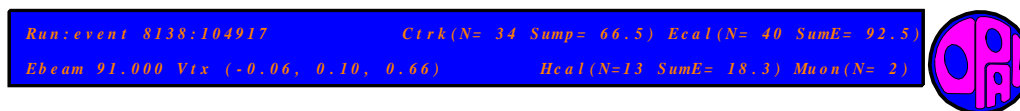


FIGURE 4.11: An event selected as $q\bar{q}'\mu\nu_\mu$ at $\sqrt{s} = 183\text{ GeV}$, displayed using GROPE.

```
Run:event 9272: 33572      Ctrk(N= 45 Sump=128.8) Ecal(N= 64 SumE=114.4)
Ebeam 94.500 Vtx ( -.01,  .09,-1.57) Hcal(N=28 SumE= 20.9) Muon(N= 1)
```

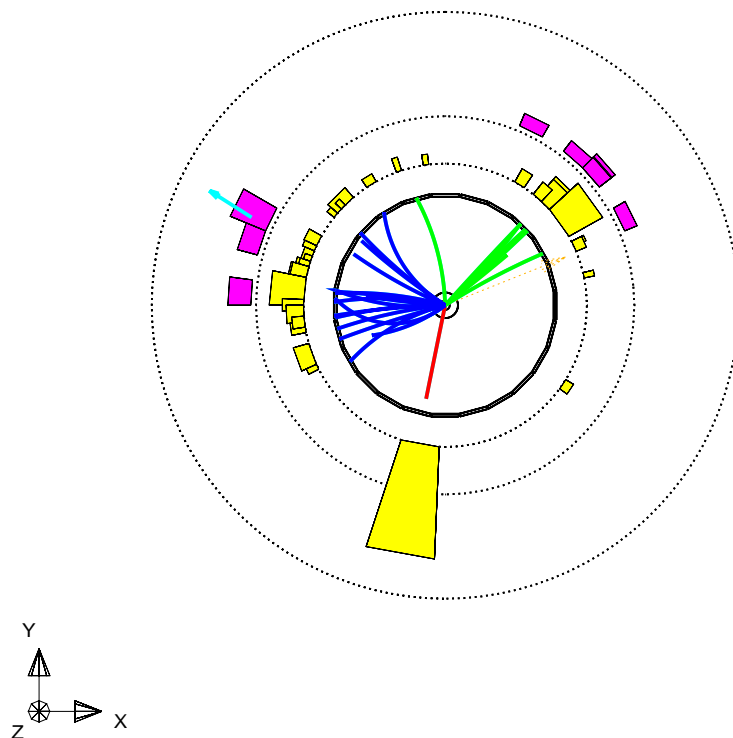


FIGURE 4.12: An event selected as $q\bar{q}'e\nu_e$ at $\sqrt{s} = 189\text{GeV}$, displayed using GROPE.

4.3.3 KINEMATIC FITTING.

As previously noted, TGC studies can use cuts which make use of the known W-mass to reduce the level of background accepted. Kinematic fits are performed[54] to provide this extra background rejection and also to give improved values of the event kinematics. In any given event the measured quantities—the 4-momenta of the charged lepton and the jets—have an associated error due to the detector resolution. In addition to this there are four unmeasured quantities: the 4-momentum of the neutrino. Using kinematic constraints, the measured quantities may be fitted within their errors to calculate the most likely 4-momenta for each of the four fermions. The kinematic fits are performed by the WV package, which also calculates the T.G.C. angles, used in the analysis of the next chapter.

The simplest fit uses five constraints: four from conservation of energy and momentum and the last from the masslessness of the neutrino. This gives one over-constraint, and so this fit is termed the “1c fit”. In addition to these five constraints, it is possible to include an additional contribution from the invariant mass of the charged lepton-neutrino system and another from that of the dijet system. The correct form with which to fit these masses is a Breit-Wigner with a central value of the world-average value of the W mass. However, this is difficult to incorporate into a kinematic fit, and so it is approximated by a gaussian distribution; the width and central value of this gaussian is altered at each iteration of the fit so that the mass value given by the last iteration has the same probability as that given by the—correct—Breit-Wigner distribution. The additional two mass constraints give seven constraints overall, and so this is a triply over-constrained (3c) fit. The acceptance of signal and rejection of background was studied by the author[55] using $\sqrt{s} = 172\text{GeV}$ simulated data, which contributed to the inclusion of an additional cut on the sample such that any event which does not pass one of the fits at the 99.9% level is rejected.

As is illustrated in figure 4.13, the 3c-fit gives the best measurement of the kinematic variables, and the 1c-fit gives a small improvement over the

raw measured quantities. shows distributions of the energy resolution for the charged lepton in selected $W^+W^- \rightarrow q\bar{q}'l\nu_l$ events and of the resolution of the cosine of the W production angle (which is the same as the direction in the detector frame of the hadronic system).

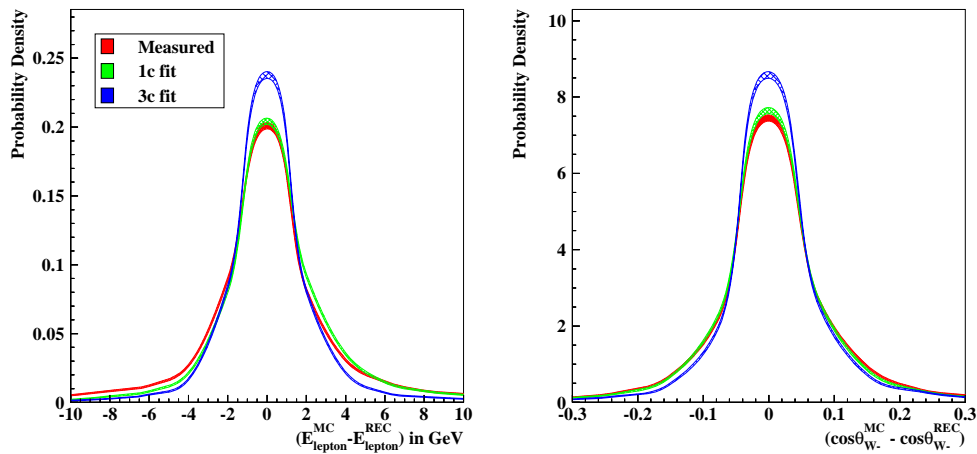


FIGURE 4.13: Distributions of the resolution of the energy of charged leptons from $W^+W^- \rightarrow q\bar{q}'l\nu_l$ events.

4.3.4 THE EFFECT OF THE SELECTION ON KINEMATIC VARIABLES

The plots in 4.14 show the effect of the selection algorithm on the lepton energy, E_L , and the cosine of the W production angle, $\cos\theta_W$. Three distributions are shown in each plot; the first shows the generator level quantities; the second shows the same quantities but only for those events that were selected; the third shows the reconstructed quantities for events that were selected. The second plots allow the effect of the selection algorithm on the distributions to be—somewhat—separated from that of the detector resolution. Both the acceptance and the detector resolution tend to soften the distributions. As it is precisely the shape of the distributions of $\cos\theta_W$ and other derived variables which are measured in T.G.C. studies, it is obvious that neglecting such effects could lead to a biased measurement.

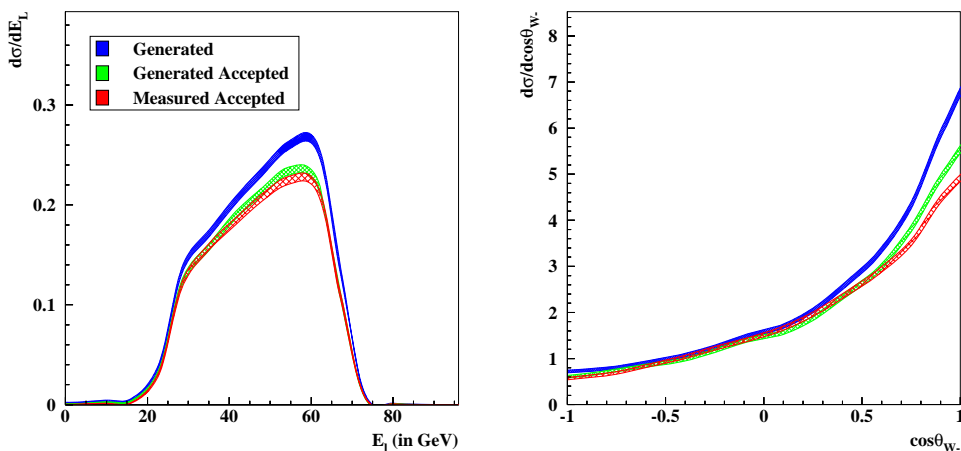


FIGURE 4.14: Distributions of the lepton energy, E_L , and the cosine of the W production angle, $\cos\theta_W$, for all $W^+W^- \rightarrow q\bar{q}l\nu_l$ events showing generator level quantities, for selected events showing the generator level quantities, and for selected events showing the reconstructed quantities.

4.4 THE PERFORMANCE OF THE SELECTION ALGORITHM

4.4.1 THE SELECTED DATA SAMPLE

The run in 1997 was at a centre of mass energy of 183GeV, and the integrated luminosity was 57.0pb^{-1} ; 111 events were selected as $q\bar{q}'e\nu_e$, and 114 as $q\bar{q}'\mu\nu_\mu$. In 1998 the centre of mass energy was 189GeV and the integrated luminosity was 183.1pb^{-1} ; 360 events were selected as $q\bar{q}'e\nu_e$, and 387 as $q\bar{q}'\mu\nu_\mu$. The distributions in the angular variable phase-space (described in §2.2.3) of the event sample are shown in figure 4.15, with distributions from Standard Model Monte Carlo W-pair events.

The number of events selected may be compared with the predictions obtained from Monte Carlo samples, given in the following section.

4.4.2 EXPECTED SIGNAL AND BACKGROUND CROSS-SECTIONS

The expected accepted signal and background levels are found by performing the selection algorithms on fully simulated Monte Carlo samples; the results for the 183GeV and 189GeV selections are shown in tables 4.1 and 4.2 respectively. At both energies the `grc4f` generator was used for the CC3 samples; the other generators used were as previously described.

The error on the predicted numbers and cross-sections in these tables is calculated from the Binomial standard deviation of the number of accepted

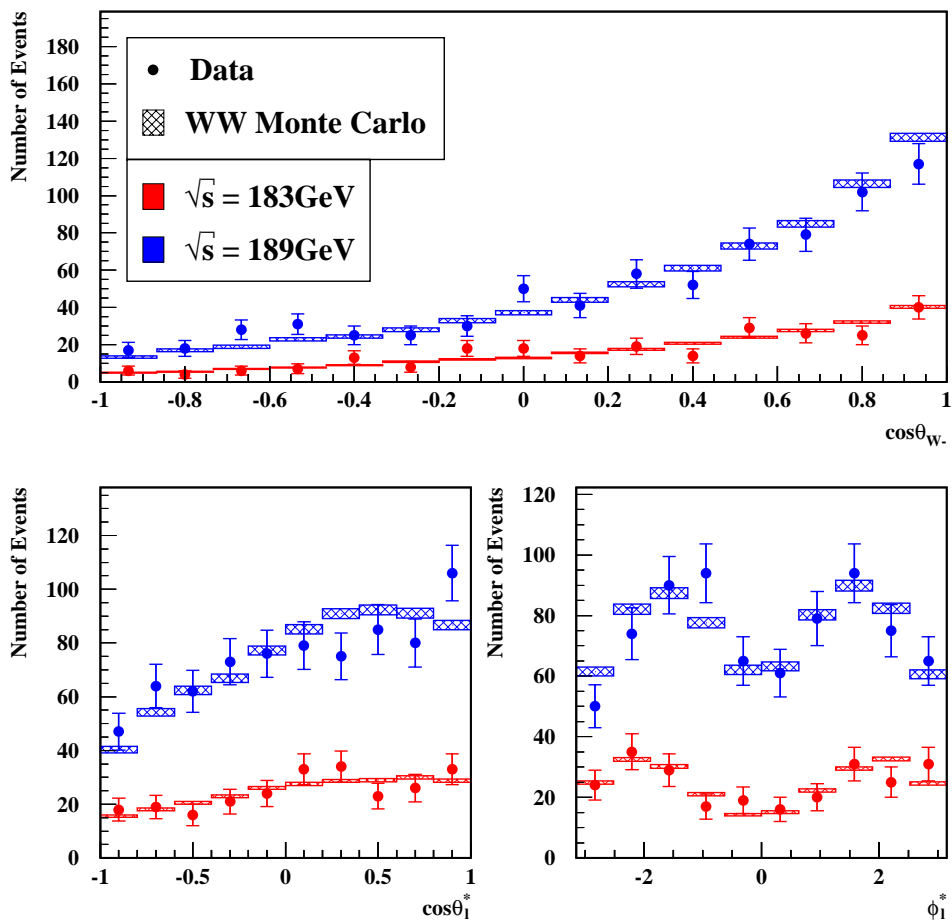


FIGURE 4.15: Plots showing the distributions of the data sample in the angular variable phase-space; distributions from Standard Model W -pair events are also shown for comparison.

Process	N_{MC}^{TOT}	$N_{MC}^{ACC:q\bar{q}e\nu_e}$	$N_{MC}^{ACC:q\bar{q}\mu\nu_\mu}$	$\lambda_{MC}^{ACC:q\bar{q}e\nu_e}$	$\sigma_{MC}^{ACC:q\bar{q}e\nu_e}$ (in fb)	$\lambda_{MC}^{ACC:q\bar{q}\mu\nu_\mu}$	$\sigma_{MC}^{ACC:q\bar{q}\mu\nu_\mu}$ (in fb)
$W^+W^- \rightarrow q\bar{q}'e\nu_e$	13855	11860	15	106.21 ± 0.37	1853.6 ± 6.4	0.13 ± 0.03	2.3 ± 0.6
$W^+W^- \rightarrow q\bar{q}'\mu\nu_\mu$	14139	6	12537	0.05 ± 0.03	0.9 ± 0.6	112.27 ± 0.34	1959.4 ± 5.9
$q\bar{q}'\tau\nu_\tau$	14168	590	492	5.28 ± 0.22	92.2 ± 3.8	4.41 ± 0.20	76.9 ± 3.4
$q\bar{q}'\bar{l} \ \& \ q\bar{q}'l\nu_l^a$ (no e^+e^-)	40566 ^b	9879	10327	-0.4 ± 1.5	-7 ± 26	4 ± 1.5	72 ± 27
$\bar{l}l'\bar{l}' \ \& \ l^{-\bar{l}'}l^+\nu_l$ (no e^+e^-)	15090	3	4	0.03 ± 0.02	0.6 ± 0.3	0.05 ± 0.02	0.8 ± 0.4
$q\bar{q}q'\bar{q}' \ \& \ q'\bar{q}''q''l'\bar{q}'''$	39312	19	27	0.22 ± 0.05	3.8 ± 0.9	0.31 ± 0.06	5.4 ± 1.0
$e^-e^+q\bar{q}$	133677	247	1	2.83 ± 0.18	49.4 ± 3.1	0.01 ± 0.01	0.2 ± 0.2
$e^-e^+\tau^-\tau^+$	9378	1	0	0.01 ± 0.01	0.2 ± 0.2	< 0.03	< 0.6
$Z^0/\gamma \rightarrow q\bar{q}$	500000	185	64	2.28 ± 0.17	40.0 ± 2.9	0.79 ± 0.10	13.7 ± 1.7
2-photon	168177	5	0	0.57 ± 0.25	10.0 ± 4.5	< 0.3	< 6

^aThis entry represents an attempt to quantify the additional accepted cross-section from CC20 processes (such as $e^+e^- \rightarrow We\nu_e \rightarrow q\bar{q}'l\nu_l$; see figure 4.4) and NC48 processes (such as $e^+e^- \rightarrow Z^0Z^0 \rightarrow q\bar{q}l\bar{l}$; see figure 4.5). However the CC20 processes necessarily include the CC3 processes. Therefore, in order to evaluate the *additional* cross-section, the accepted CC3 levels must be subtracted from the total $q\bar{q}l\bar{l}$ & $q\bar{q}'l\nu_l$ cross-section; as the additional cross-section is small compared with the CC3 cross-section, it has a large associated error.

^bThe total number and absolute number accepted include all the CC3 events, and so are not terribly meaningful.

TABLE 4.1: *The performance of the selection algorithm at $\sqrt{s} = 183\text{GeV}$, evaluated using fully simulated Monte Carlo generated samples. N_{MC}^{TOT} is the total number of events in the sample; $N_{MC}^{ACC:q\bar{q}l\nu_l}$ is the number of events selected as being $q\bar{q}'l\nu_l$ (with l being e or μ as normal); $\lambda_{MC}^{ACC:q\bar{q}l\nu_l}$ is the corresponding number of events expected in the data sample; and $\sigma_{MC}^{ACC:q\bar{q}l\nu_l}$ is the accepted cross-section. For those processes where no events are selected the 95% confidence level limit on the expected accepted number of events and corresponding cross-section are quoted; the contribution from such processes to the total cross-section is assumed to be zero.*

Process	N_{MC}^{Tot}	$N_{MC}^{Acc:q\bar{q}e\nu_e}$	$N_{MC}^{Acc:q\bar{q}\mu\nu_\mu}$	$\lambda_{MC}^{Acc:q\bar{q}e\nu_e}$	$\sigma_{MC}^{Acc:q\bar{q}e\nu_e}$ (in fb)	$\lambda_{MC}^{Acc:q\bar{q}\mu\nu_\mu}$	$\sigma_{MC}^{Acc:q\bar{q}\mu\nu_\mu}$ (in fb)
$W^+W^- \rightarrow q\bar{q}e\nu_e$	11954	9852	14	368.9 ± 1.5	1970 ± 8	0.52 ± 0.14	2.8 ± 0.7
$W^+W^- \rightarrow q\bar{q}\mu\nu_\mu$	12014	14	10039	0.52 ± 0.14	2.8 ± 0.7	375.9 ± 1.5	2008 ± 8
$q\bar{q}\tau\nu_\tau$	12039	591	456	22.1 ± 0.9	118 ± 5	17.1 ± 0.8	91 ± 4
llqq (CC3 Removed) ^a	43396	10334	10689	-5 ± 3	-28 ± 18	5 ± 4	29 ± 19
$\bar{l}l\bar{l}'$ (no e^+e^-)	15855	4	3	0.15 ± 0.07	0.8 ± 0.4	0.11 ± 0.06	0.6 ± 0.3
$q'\bar{q}'q''\bar{q}''$	42088	3	28	0.11 ± 0.06	0.6 ± 0.3	1.0 ± 0.2	56 ± 1
$e^-e^+\bar{f}f$ (s-channel)	41402	228	2	1.71 ± 0.11	9.12 ± 0.60	0.01 ± 0.01	$8 \cdot 10^{-5} \pm 6 \cdot 10^{-5}$
$e^-e^+\bar{f}f$ (t-channel)	289810	84	2	3.14 ± 0.34	16.8 ± 1.8	0.07 ± 0.05	0.0004 ± 0.0003
$Z^0/\gamma \rightarrow q\bar{q}$	500000	136	73	5.03 ± 0.43	26.8 ± 2.3	2.70 ± 0.32	14.4 ± 1.7
2-photon	150000	5	0	1.9 ± 0.8	10 ± 4	< 1.1	< 6.0

^aSee table 4.1 for notes on these entries

TABLE 4.2: The performance of the selection algorithm at $\sqrt{s} = 189\text{GeV}$, evaluated using fully simulated Monte Carlo generated samples. The symbols are as in table 4.1.

events:

$$\begin{aligned}
 \Delta\lambda_{\text{MC}}^{\text{Acc}} &= \sqrt{N_{\text{MC}}^{\text{Tot}} p^{\text{Acc}} (1 - p^{\text{Acc}})} \times \frac{\mathcal{L}_D}{\mathcal{L}_{\text{MC}}} \\
 &= \sqrt{N_{\text{MC}}^{\text{Tot}} \frac{N_{\text{MC}}^{\text{Acc}}}{N_{\text{MC}}^{\text{Tot}}} \left(1 - \frac{N_{\text{MC}}^{\text{Acc}}}{N_{\text{MC}}^{\text{Tot}}}\right)} \times \frac{\mathcal{L}_D}{\mathcal{L}_{\text{MC}}} \\
 &= \sqrt{N_{\text{MC}}^{\text{Acc}} \left(1 - \frac{N_{\text{MC}}^{\text{Acc}}}{N_{\text{MC}}^{\text{Tot}}}\right)} \times \frac{\mathcal{L}_D}{\mathcal{L}_{\text{MC}}}
 \end{aligned}$$

and

$$\Delta\sigma_{\text{MC}}^{\text{Acc}} = \sqrt{N_{\text{MC}}^{\text{Acc}} \left(1 - \frac{N_{\text{MC}}^{\text{Acc}}}{N_{\text{MC}}^{\text{Tot}}}\right)} \frac{1}{\mathcal{L}_{\text{MC}}}.$$

$\Delta\sigma_{\text{MC}}^{\text{Acc}}$ is the error on the accepted cross-section, $\Delta\lambda_{\text{MC}}^{\text{Acc}}$ is the error on the predicted number of accepted events for a luminosity of \mathcal{L}_D , and $N_{\text{MC}}^{\text{Acc}}$ is the number of Monte Carlo events accepted from a sample of $N_{\text{MC}}^{\text{Tot}}$ events, corresponding to a luminosity of \mathcal{L}_{MC} . These errors are not gaussian for small $N_{\text{MC}}^{\text{Acc}}$, as in, for example, the 2-photon sample where only 8 events in the simulated sample were accepted. However, as the absolute errors due to these small numbers happen to be reasonably small compared with the absolute errors due to the larger numbers, the overall errors on the accepted background cross-section, on the efficiency and on the purity are unaffected.

From tables 4.1 & 4.2 it may be seen that the largest background process is, unsurprisingly, $W^+W^- \rightarrow q\bar{q}'\tau\nu_\tau$, and the next largest are “llqq(CC3 removed)” and $Z^0/\gamma \rightarrow q\bar{q}$. The “llqq(CC3 removed)” cross-section is calculated by subtracting the accepted $W^+W^- \rightarrow q\bar{q}'l\nu_l$ cross-section from the accepted cross-section for 4-fermion events without final state e^-e^+ pairs; as these numbers are both large compared with the difference between them (i.e.,

as the $q\bar{q}'l\nu_l$ cross-section is dominated by the CC3 process) the calculated background cross-section has a suitably large error; when this contribution is calculated as negative, it is omitted from the purity calculation.

4.4.3 EFFICIENCY AND PURITY

In the discussion of the first section of this chapter, it was seen that the difference between signal and background processes was not unequivocal; there are the inseparable, interfering charge current processes which must, literally, be signal because their final state is indistinguishable from that of W-pair decay; conversely, there are misidentified $W^+W^- \rightarrow q\bar{q}'\tau\nu_\tau$ events which arise from a final state and yet are more often considered as signal than the interfering charge current processes. Both have some sensitivity to the TGC strengths. It is not unambiguous what may be defined as the efficiency and purity.

However, as the efficiency and purity are properties of the selection algorithm which is tuned on CC3 events, the efficiency and purity are defined as

$$E_{W^+W^- \rightarrow q\bar{q}'l\nu_l} = \frac{\sigma_{W^+W^- \rightarrow q\bar{q}'l\nu_l}^{\text{Acc}}}{\sigma_{W^+W^- \rightarrow q\bar{q}'l\nu_l}^{\text{Tot}}}$$

$$P_{W^+W^- \rightarrow q\bar{q}'l\nu_l} = \frac{\sigma_{W^+W^- \rightarrow q\bar{q}'l\nu_l}^{\text{Acc}}}{\sigma^{\text{Acc}}}$$

where $\sigma_{W^+W^- \rightarrow q\bar{q}'l\nu_l}^{\text{Acc}}$ is the accepted $W^+W^- \rightarrow q\bar{q}'l\nu_l$ cross-section from a total cross-section of $\sigma_{W^+W^- \rightarrow q\bar{q}'l\nu_l}^{\text{Tot}}$, and σ^{Acc} is the total cross-section for events selected by the algorithm.

The efficiencies are obtained by using the selection algorithm on large samples of fully simulated CC3 events generated with `grc4f`, and are as follows:

At $\sqrt{s} = 183\text{GeV}$:

$$\begin{aligned} E_{W^+W^- \rightarrow q\bar{q}' e\nu_e} &= 85.6 \pm 0.3\% \\ E_{W^+W^- \rightarrow q\bar{q}' \mu\nu_\mu} &= 88.6 \pm 0.3\%. \end{aligned}$$

And at $\sqrt{s} = 189\text{GeV}$:

$$\begin{aligned} E_{W^+W^- \rightarrow q\bar{q}' e\nu_e} &= 82.4 \pm 0.3\% \\ E_{W^+W^- \rightarrow q\bar{q}' \mu\nu_\mu} &= 83.6 \pm 0.3\%. \end{aligned}$$

The accepted cross-sections for the signal and total background are obtained as in tables 4.1 & 4.2:

At $\sqrt{s} = 183\text{GeV}$:

$$\begin{aligned} \sigma_{W^+W^- \rightarrow q\bar{q}' e\nu_e}^{\text{SIG}} &= 1876 \pm 7\text{fb} \\ \sigma_{W^+W^- \rightarrow q\bar{q}' e\nu_e}^{\text{BG}} &= 201 \pm 27\text{fb} \\ \sigma_{W^+W^- \rightarrow q\bar{q}' \mu\nu_\mu}^{\text{SIG}} &= 1905 \pm 6\text{fb} \\ \sigma_{W^+W^- \rightarrow q\bar{q}' \mu\nu_\mu}^{\text{BG}} &= 176 \pm 27\text{fb} \end{aligned}$$

which gives purities of

$$\begin{aligned} P_{W^+W^- \rightarrow q\bar{q}' e\nu_e} &= 90.3 \pm 2.5\% \\ P_{W^+W^- \rightarrow q\bar{q}' \mu\nu_\mu} &= 91.6 \pm 2.5\%. \end{aligned}$$

and at $\sqrt{s} = 189\text{GeV}$:

$$\sigma_{W^+W^- \rightarrow q\bar{q}' e\nu_e}^{\text{SIG}} = 1970 \pm 8\text{fb}$$

$$\sigma_{W^+W^- \rightarrow q\bar{q}' e\nu_e}^{\text{BG}} = 185 \pm 19\text{fb}$$

$$\sigma_{W^+W^- \rightarrow q\bar{q}' \mu\nu_\mu}^{\text{SIG}} = 2008 \pm 8\text{fb}$$

$$\sigma_{W^+W^- \rightarrow q\bar{q}' \mu\nu_\mu}^{\text{BG}} = 144 \pm 20\text{fb}$$

which gives purities of

$$P_{W^+W^- \rightarrow q\bar{q}' e\nu_e} = 91.4 \pm 1.7\%$$

$$P_{W^+W^- \rightarrow q\bar{q}' \mu\nu_\mu} = 93.3 \pm 1.9\%.$$

These are quoted only to provide information about the performance of the selection procedure; the efficiency and purity do not directly enter the analysis.

CHAPTER 5

THE NEAR NEIGHBOUR MAXIMUM LIKELIHOOD ANALYSIS

There are several extant methods for measuring the Triple Gauge Couplings, each with their own strengths and weaknesses. The Near Neighbour Maximum Likelihood (N.N.M.L.) method used in this thesis and described in this chapter was developed to utilise OPAL's detector-simulated Monte Carlo samples, and thereby automatically incorporate the effects of detector resolution and acceptance.

At its simplest, the method performs a single-parameter fit using reference samples of a single process (described in section §5.2). This bare method is sufficiently flexible that it may be naturally extended to incorporate any number of accepted processes (section §5.4), and to fit to an arbitrary number of TGC parameters (section §5.5).

5.1 INTRODUCTION TO THE N.N.M.L. METHOD

The N.N.M.L. analysis essentially consists of three stages:

- i.) Differential cross-sections are evaluated at several T.G.C. values for each data point in the sample to be analyzed. This is achieved using a Near Neighbour weighting method on large Monte Carlo reference samples, each generated with a different T.G.C. strength.

- ii.) The differential cross-sections for a given data point are fit to a quadratic function (given explicitly in equation 5.19 following from the form of the cross-section given in §2.2.1), to give the differential cross-sections as functions of the T.G.C. parameter. Hence, the probability density function is obtained.
- iii.) A maximum likelihood fit is performed on the probability density functions to determine the T.G.C. strength which makes the test sample most probable.

The Near Neighbour weighting method is used in the first stage. It is a general method of measuring a probability density (or, equivalently, a differential cross-section) from a distribution of discrete points. The principle of such a weighting technique is simple, but the mathematical framework to describe it in its general form may seem somewhat laborious. For this reason, it is worth describing a prototypical N.N.M.L. method so that the formal derivation may be presented within some practical context[†].

A reference sample is distributed in a phase-space consisting of the variables in which the differential cross-section is desired (in the case of this analysis, $\cos\theta_W$, $\cos\theta_l^*$ and ϕ_l^* , as described in §2.2.3, and illustrated in figures 2.4 & 4.15). Small volumes are constructed within this phase-space at the positions of each event in the data sample; the measured differential cross-section at each point is proportional to the number of reference events which fall within that volume. This relationship is simply expressed as

$$d\sigma = \frac{N_V}{\mathcal{L}V} \quad (5.1)$$

where V is the elemental volume, N_V is the number of events within that volume, and \mathcal{L} is the luminosity of the reference sample. This procedure is the simplest form of the Near Neighbour weighting method.

This cross-section measurement is repeated for several reference samples, each generated with a different T.G.C. strength. This gives several discrete

[†]See also, for example, *A General Method of Estimating Physical Parameters from a Distribution with Acceptance and Smearing Effects*[58] for a similar method.

values of the differential cross-section for each data point, which are then fitted to a quadratic function to obtain the differential cross-section—and, hence, the probability density—as a function of the T.G.C. parameter. The probability density functions are then used in a maximum likelihood fit to measure the T.G.C. strength of the sample. This prototypical method is shown schematically in figure 5.1.

As outlined, this method is similar to a binned maximum likelihood method; the principal difference is that the reference samples are measured only in the vicinity of the test data points which means that the whole phase space need not be populated as fully as would be required for the traditional binning method.

The description of the mathematical formalism will show that the method may be generalized so that the hard-edged bins are replaced by weighting functions, and the prototypical method emerges as one particular instance of the general method. The development of non-binned fitting methods might in itself be considered as a good motivation to investigate the general method.

It ought to be stressed that the mathematical detail described below is principally included to justify the extension to the use of general weighting functions.

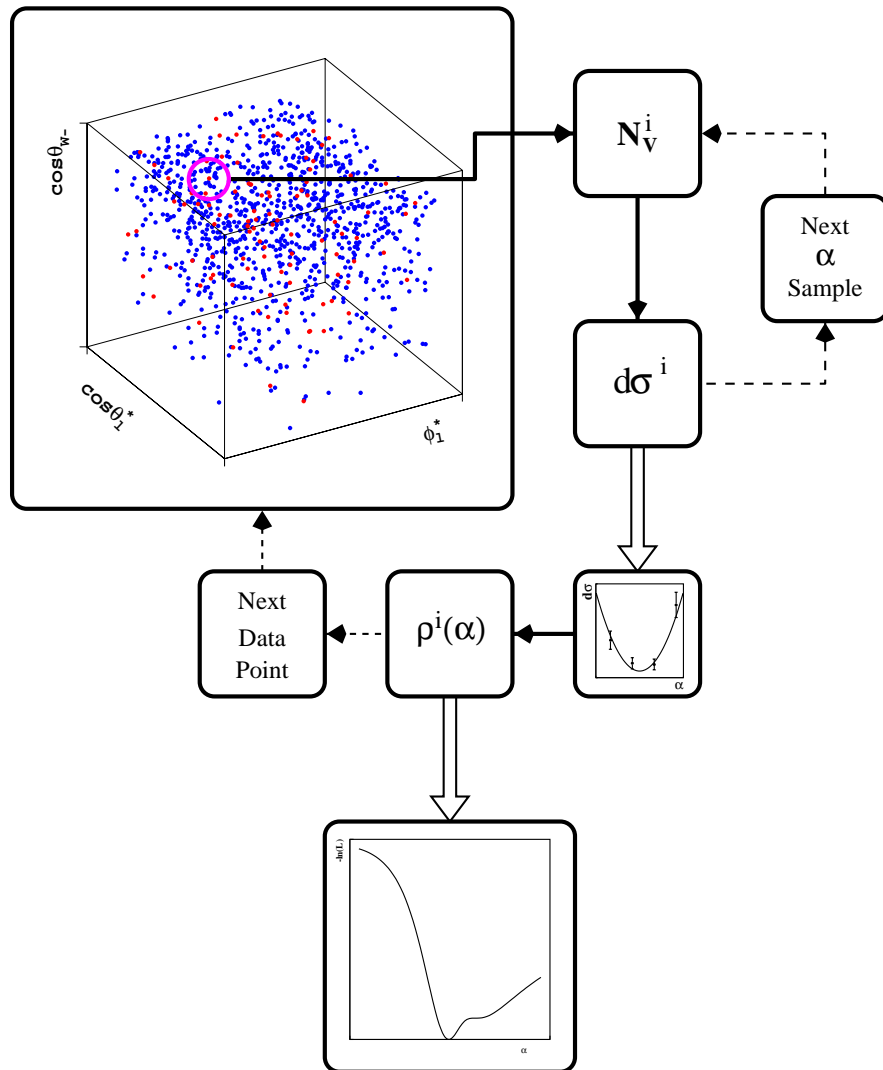


FIGURE 5.1: Schematic representation of the prototypical N.N.M.L. analysis method. The blue points represent the simulated reference sample events, and the red points represent those from the data sample to be analyzed; the purple circle represents the spherical volume centred on the data point.

5.2 THE SINGLE-PARAMETER N.N.M.L. METHOD

5.2.1 MEASURING THE DIFFERENTIAL CROSS-SECTION FROM A MONTE CARLO SAMPLE

The method of extracting the differential cross-section from a Monte Carlo reference sample is developed from the following identity for the Dirac delta function in terms of the differential cross-section, $d\sigma(\mathbf{x})$, at a point, \mathbf{x} , in an infinite, n -dimensional parameter-space:

$$d\sigma(\mathbf{x}) = \int_{V_\infty} \delta(\mathbf{x}' - \mathbf{x}) d\sigma(\mathbf{x}') d^n x'. \quad (5.2)$$

This does not seem very useful, as the differential cross-section function on the right-hand side is identical to that on the left; however, the simultaneous replacement of the right-hand term by a known reference distribution, and of the Dirac delta function by a true, analytic function means that equation 5.2 becomes an expression for a measured differential cross-section.

Upon substituting for the delta function with a limiting function with an inherent length scale, r_0 ,

$$\delta(\mathbf{x}' - \mathbf{x}) = \lim_{r_0 \rightarrow 0} \Delta(\mathbf{x}' - \mathbf{x}; r_0), \quad (5.3)$$

equation 5.2 becomes

$$d\sigma(\mathbf{x}) = \lim_{r_0 \rightarrow 0} \int_{V_\infty} \Delta(\mathbf{x}' - \mathbf{x}; r_0) d\sigma(\mathbf{x}') d^n x'. \quad (5.4)$$

$\Delta(\mathbf{x}' - \mathbf{x}; r_0)$ is a kernel of an integral equation, and may be one of a number of functions[59]; for example:

- The “Tophat” kernel

$$\Delta(\mathbf{x}; r_0) = \begin{cases} 0, & -r_0 < |\mathbf{x}| \\ \left(\frac{1}{V_n(r_0)}\right), & -r_0 \leq |\mathbf{x}| \leq r_0 \\ 0, & |\mathbf{x}| < r_0 \end{cases} \quad (5.5)$$

- The “Gaussian” kernel

$$\Delta(\mathbf{x}; r_0) = \left(\frac{1}{r_0 \sqrt{2\pi}}\right)^n \exp\left\{\frac{-\mathbf{x}^2}{2r_0^2}\right\} \quad (5.6)$$

- The “Cauchy” kernel

$$\Delta(\mathbf{x}; r_0) = \left(\frac{1}{r_0 \pi}\right)^n \frac{1}{1 + \frac{\mathbf{x}^2}{r_0^2}}, \quad (5.7)$$

where $V_n(r_0)$ is the volume of a hypersphere of radius r_0 in an n -dimensional space. The form of these functions are shown in figure 5.2.

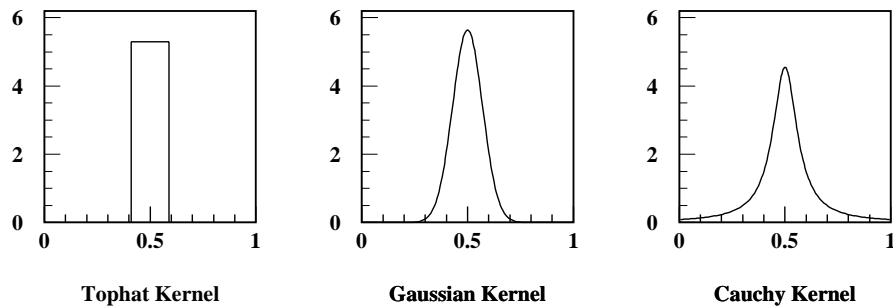


FIGURE 5.2: Illustrations of three different kernels.

The reference distribution is taken from large Monte Carlo reference samples. The probability density of an infinitely large reference sample is given

by

$$\rho(\mathfrak{x}) = \lim_{N \rightarrow \infty} \frac{1}{N} \sum_{j=1}^N \delta(\mathfrak{x} - \mathfrak{x}_j), \quad (5.8)$$

so that the differential cross-section is given by

$$d\sigma(\mathfrak{x}) = \lim_{N \rightarrow \infty} \frac{\sigma}{N} \sum_{j=1}^N \delta(\mathfrak{x} - \mathfrak{x}_j) \quad (5.9)$$

$$= \lim_{N \rightarrow \infty} \frac{1}{\mathcal{L}} \sum_{j=1}^N \delta(\mathfrak{x} - \mathfrak{x}_j) \quad (5.10)$$

where the \mathfrak{x}_j are the positions of the N individual points in the reference sample, and \mathcal{L} is the luminosity of the reference sample.

So the idealized expression for a differential cross-section measured from an infinite simulated sample is then

$$\begin{aligned} d\sigma(\mathfrak{x}) &= \int_{V_K} \lim_{r_0 \rightarrow 0} \Delta(\mathfrak{x}' - \mathfrak{x}; r_0) \lim_{N \rightarrow \infty} \frac{1}{\mathcal{L}} \left(\sum_{j=1}^N \delta(\mathfrak{x}' - \mathfrak{x}_j) \right) d^n x' \\ &= \lim_{r_0 \rightarrow 0} \lim_{N \rightarrow \infty} \frac{1}{\mathcal{L}} \sum_{j=1}^N \left(\int_{V_K} \Delta(\mathfrak{x}' - \mathfrak{x}; r_0) \delta(\mathfrak{x}' - \mathfrak{x}_j) d^n x' \right) \\ &= \lim_{r_0 \rightarrow 0} \lim_{N \rightarrow \infty} \frac{1}{\mathcal{L}} \sum_{j=1}^N \Delta(\mathfrak{x}_j - \mathfrak{x}; r_0). \end{aligned} \quad (5.11)$$

Obviously, infinitely large reference samples are impossible. The realistic case where N is finite necessitates the simultaneous removal of the limit of infinitesimal r_0 , so that equation 5.11 becomes an approximation to the true differential cross-section:

$$\begin{aligned} d\sigma_{r_0}(\mathfrak{x}) &= \frac{1}{\mathcal{L}} \sum_{j=1}^N \Delta(\mathfrak{x}_j - \mathfrak{x}; r_0). \\ &\simeq d\sigma(\mathfrak{x}) \end{aligned} \quad (5.12)$$

This is the defining equation for the Near Neighbour method, whereby a differential cross-section is measured from a simulated reference sample. Using

the Tophat kernel the original, binned, form is recovered in terms of N_{r_0} , the number of events within a volume of radius r_0 :

$$d\sigma_{r_0}(\mathfrak{x}) = \frac{1}{\mathcal{L}} \sum_{j=1}^N \left(\frac{1}{V_n(r_0)} \right), \quad -r_0 \leq |\mathfrak{x}| \leq r_0 \quad (5.13)$$

$$= \frac{N_{r_0}}{\mathcal{L}V_n(r_0)}, \quad (5.14)$$

which is exactly the form given in equation 5.1.

The derivation so far has been based on a reference sample distributed in an infinite phase-space, but T.G.C. studies tend to use angular variables which have definite limits on their values, which in turn means that the space is finite. As described in chapter 2, §2.2.3, this analysis uses a phase-space of $\cos \theta_W$, $\cos \theta_l^*$ and ϕ_l^* ; each of these variable is scaled and shifted so that their range runs from 0 to 1. To take the finite phase-space into account it is not necessary to modify equation 5.12, only to use modified kernels. The kernels of equations 5.5–5.7 are normalised such that their integral over all space is equal to unity, as in the Dirac delta function; the modified kernels must have this same normalisation, but in a finite space of volume V_K :

$$\Delta(\mathfrak{x}; r_0) = \begin{cases} 0, & -r_0 < |\mathfrak{x}| \\ \left(\frac{1}{V'_n(\mathfrak{x}; r_0)} \right), & -r_0 \leq |\mathfrak{x}| \leq r_0 \\ 0, & |\mathfrak{x}| < r_0 \end{cases} \quad (5.15)$$

$$\Delta(\mathfrak{x}; r_0) = \left(\int_{V_K} \exp \left\{ \frac{-\mathfrak{x}'^2}{2r_0^2} \right\} d^n x' \right)^{-1} \exp \left\{ \frac{-\mathfrak{x}^2}{2r_0^2} \right\} \quad (5.16)$$

$$\Delta(\mathfrak{x}; r_0) = \left(\int_{V_K} \frac{d^n x'}{1 + \frac{\mathfrak{x}'^2}{r_0^2}} \right)^{-1} \frac{1}{1 + \frac{\mathfrak{x}^2}{r_0^2}}. \quad (5.17)$$

$V'_n(\mathfrak{x}; r_0)$ is the same as the previously defined $V_n(r_0)$ except that it may be cut-off if it is within r_0 of a phase-space boundary.

Using equation 5.12, the probability density at any position may be evaluated at any value of the T.G.C. parameters for which there exists a Monte

Carlo reference sample. The value obtained is approximate because the finite statistics of the reference sample compel r_0 to be finite; in the limit of infinite statistics r_0 may become infinitesimal and the measurement would become exact; it is the number of events in the reference sample, N , which determines the size of r_0 and, therefore, the accuracy of the calculated probability density. There is no obvious reason to have the same value of r_0 for different data events, so that, for example, a data event in a region of high statistics may have a lower value of r_0 than one in a sparse region. The different methods of choosing a value for r_0 to use are investigated later.

The important thing to note about the expression for $d\sigma_{r_0}^{\alpha_0}(\mathbf{x})$ is that it automatically contains all experimental effects contained in the reference sample—e.g., resolution, acceptance, jet reconstruction etc. etc.—which may be difficult to incorporate in other T.G.C. analyses.

5.2.2 EXTRAPOLATING THE PROBABILITY DENSITY AS A FUNCTION OF THE T.G.C. STRENGTH

A maximum likelihood fit requires a continuous probability density which varies as a function of the fit-parameter, in this case, the T.G.C. strength, α ; equation 5.12 only evaluates the differential cross-section at discrete values of the coupling strength, but these may be used to find the probability density function.

Almost by definition, the reference probability density is given by

$$\rho^\alpha(\mathbf{x}) = \frac{d\sigma^\alpha(\mathbf{x})}{\sigma^\alpha} \quad (5.18)$$

where $d\sigma(\mathbf{x}, \alpha)$ and $\sigma(\alpha)$ are, respectively, the differential and total cross-sections for the reference process with a parameter value of α .

As mentioned in Chapter 1.2, the Lagrangian for the reference process (whether it involves only the CC3 diagrams or the full set of CC20) depends

on the triple gauge coupling parameters linearly, and so the cross-section (differential or total) must depend on them quadratically. In the W-model, for example, the elemental cross-section is

$$d\sigma(\mathbf{x}, \alpha_W) = d\sigma^{\text{SM-SM}}(\mathbf{x}) + \alpha_W d\sigma^{\text{SM-W}}(\mathbf{x}) + \alpha_W^2 d\sigma^{\text{W-W}}(\mathbf{x}), \quad (5.19)$$

assuming all the other T.G.C.s in the Lagrangian are zero. To explain the notation, $d\sigma^{\text{SM-SM}}(\mathbf{x})$ is the Standard Model differential cross-section; $d\sigma^{\text{SM-W}}(\mathbf{x})$ is the differential cross-section term arising from the W-model term in the Lagrangian, \mathcal{L}_W , multiplied with that of the Standard Model; and $d\sigma^{\text{W-W}}(\mathbf{x})$ is that arising solely from the W-model Lagrangian terms. It should be noted that equation 5.19 is valid for both the CC3 W-pair production cross-section and for the full CC20 cross-section, and that, obviously, it holds for any of the T.G.C. parameters.

The equation describing any arbitrary parabola has three parameters, and so a minimum of three points on that parabola are needed to constrain it exactly; if more than three points are used the parabola is overconstrained and a weighted least squares fit may be performed. (It should be noted that it is not obvious for all choices of kernel what the error on the value given by equation 5.12 should be; rather than interrupt the derivation of the method, this shall be discussed when considering the choice of kernel in section §5.3). So, by evaluating equation 5.12 at any single point from three or more reference samples generated with different T.G.C. strengths, and fitting a parabola to these discrete values, the differential cross-section at that point may be obtained as a function of the coupling strength.

Upon integrating equation 5.19 over any arbitrary volume, V , it is seen that the integrated cross-section, $\sigma_V(\alpha_W)$, shows the same quadratic behaviour independent of the size or shape of V :

$$\begin{aligned} \sigma_V(\mathbf{x}, \alpha_W) &= \int_V d\sigma(\mathbf{x}, \alpha_W) \\ &= \int_V d\sigma^{\text{SM-SM}}(\mathbf{x}) + \alpha_W \int_V d\sigma^{\text{SM-W}}(\mathbf{x}) + \alpha_W^2 \int_V d\sigma^{\text{W-W}}(\mathbf{x}) \end{aligned} \quad (5.20)$$

The extension to the total cross-section is therefore

$$\sigma(\alpha_W) = \sigma^{\text{SM-SM}} + \alpha_W \sigma^{\text{SM-W}} + \alpha_W^2 \sigma^{\text{W-W}}. \quad (5.21)$$

The parabolic behaviour of the cross-section with the $\alpha_{W\phi}$ parameter (defined in §2.1.1 of chapter 2) is illustrated in the plots in figure 5.3. The top left-hand plot shows the discrete values of the total cross-sections—and associated error—overlaid with the fitted parabola; the other plots show the same but for the differential cross-section at five arbitrary points in phase-space, measured using equation 5.12 with the Gaussian kernel.

Now the probability density function at a given point is simply given by the quotient of the differential cross-section parabola at that point and the total cross-section parabola:

$$\rho_{r_0}(\mathbf{x}, \alpha) = \frac{d\sigma(\mathbf{x}, \alpha)}{\sigma(\alpha)}. \quad (5.22)$$

5.2.3 MAXIMUM LIKELIHOOD FITTING OF THE DATA SAMPLE

Using the expression in 5.22 the probability density is evaluated for each of the N_{DATA} data points. The negative log likelihood (N.L.L.) may then be formed as

$$\mathcal{L}(\alpha) \equiv -\ln L(\alpha) \quad (5.23)$$

$$= \sum_{i=1}^{N_{\text{DATA}}} -\ln \rho_{r_0}(\mathbf{x}_i, \alpha). \quad (5.24)$$

Equation 5.23 defines $\mathcal{L}(\alpha)$ as the negative logarithm of $L(\alpha)$, the product of the individual probability densities. The minimum of this expression occurs at the value of α which makes the data sample most likely to have occurred, which is the best estimate of the true value of α which may be obtained using only the distribution of the data events. As already seen, the total cross-section—and, therefore, the total event rate—is also dependent on the T.G.C.s and so

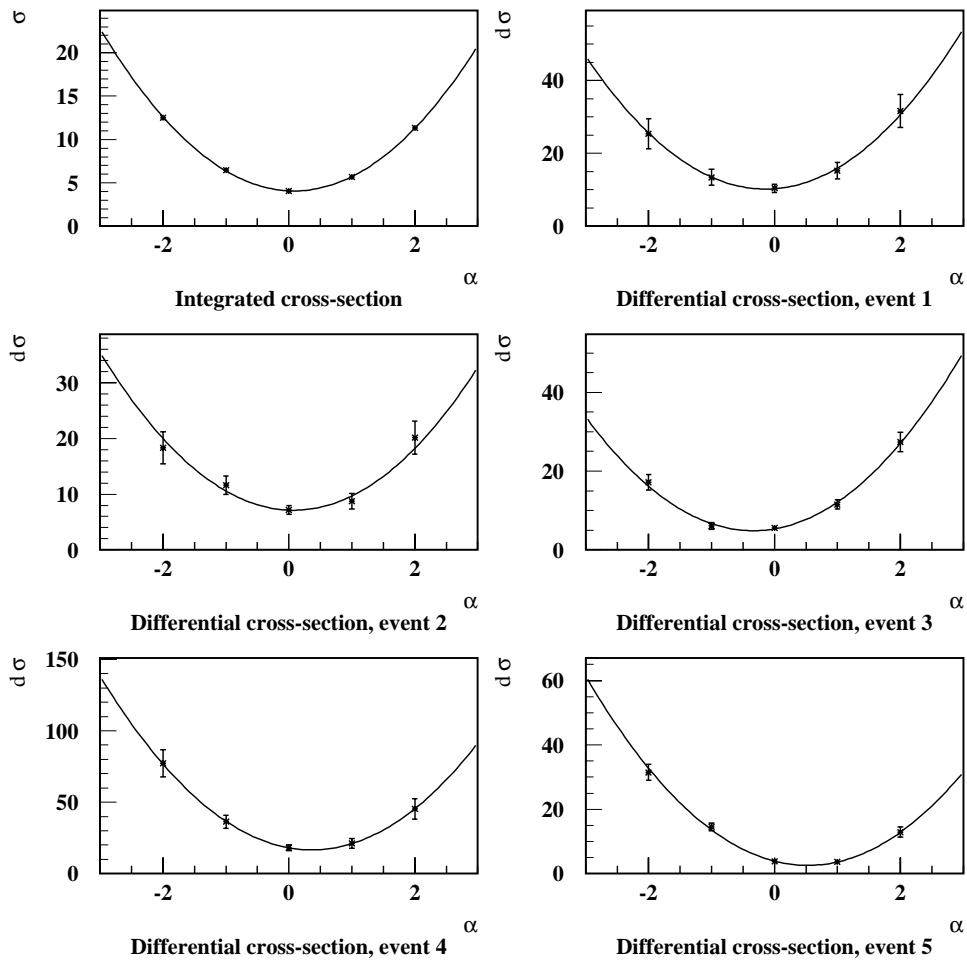


FIGURE 5.3: Discrete values (with error) of the total and differential cross-sections at five values of the $\alpha_{W\phi}$ parameter, overlaid with the fitted parabola.

it is appropriate to perform an extended maximum likelihood fit according to the following expression:

$$\mathcal{L}_E(\alpha) \equiv -\ln \left(\left[\prod_{i=1}^{N_{\text{DATA}}} \rho_{r_0}(\mathbf{x}, \alpha) \right] P(N_{\text{DATA}}; \lambda(\alpha)) \right) \quad (5.25)$$

$$\sim \mathcal{L}(\alpha) + \lambda(\alpha) - N_{\text{DATA}} \ln \lambda(\alpha), \quad (5.26)$$

where $\lambda(\alpha)$ is the mean expected number of data events for a T.G.C. value of α , and $P(N_{\text{DATA}}; \lambda(\alpha))$ is the standard Poisson probability:

$$P(N_{\text{DATA}}; \lambda(\alpha)) = e^{-\lambda(\alpha)} \frac{\lambda(\alpha)^{N_{\text{DATA}}}}{N_{\text{DATA}}!}. \quad (5.27)$$

(Equation 5.25 defines the negative extended log likelihood (N.E.L.L.); the expression labelled 5.26 is not an equality because a $\ln N_{\text{DATA}}!$ term is omitted as it doesn't depend on the fit parameter, α , and therefore cannot effect the fit results. It is this second expression which is used in the extended likelihood fits). The N.E.L.L. should give the best estimate of α in the simplest case where there is no accepted background and only one T.G.C. is allowed to vary. Unless stated otherwise, all quoted fit results are found using the extended log likelihood fit.

The maximum likelihood fits are performed by the MINUIT [60, 61] function minimization package.

5.3 CONFIGURATION AND PERFORMANCE OF THE N.N.M.L.

It is worth considering now how the simple single-parameter fit is used in practise at this point, so that the extensions of the method may build on this. The principal choice to make is which kernel should be used in equation 5.12, and, subsequently, how the value of the length scale, r_0 , should be chosen. However, prior to a comparison of the performance of the kernels, the error on the value of the differential cross-section from equation 5.12—deferred from §5.2.2—must be discussed.

5.3.1 THE STATISTICAL ERROR IN THE PARABOLIC FIT

When using the Tophat kernel the weight obtained for each data event from any reference sample is simply the number of reference events which fall within some arbitrary spherical volume, multiplied by an appropriate scale factor; in this respect, it has similarities with a normal histogramming method. In particular, the error on the measured differential cross-section is easily obtained; from equations 5.15 and 5.12, the differential cross-section measured from a MC reference sample using the Tophat kernel is given by:

$$d\sigma^{\alpha_1}(\mathbf{x}) = \frac{1}{\mathcal{L}} \sum_{j=1}^N \Delta(\mathbf{x} - \mathbf{x}_j; r_0) \quad (5.28)$$

$$= \frac{N_{r_0}}{\mathcal{L}V'_n(r_0)} \quad (5.29)$$

where N_{r_0} is the number of reference points within a distance of r_0 of the data point at position \mathbf{x} . Hence, the error on the differential cross-section is then

$$\Delta d\sigma^{\alpha_1}(\mathbf{x}) = \frac{\sqrt{N_{r_0}}}{\mathcal{L}V'_n(r_0)}, \quad (5.30)$$

assuming that there are sufficient reference points within the volume so that the Poisson standard deviation, \sqrt{N} , is a good approximation to the Gaussian standard deviation. In the case of the Gaussian and Cauchy kernels there is no definite volume defined by r_0 , and so it is harder to get a handle on the error on the measured differential cross-sections.

As has been stated previously, when measuring the differential cross-section it is important to choose as small a value of r_0 as is practicable, which is determined by the population of the reference samples. Hence, the error on the differential cross-section measured from a reference sample should reflect the population of that reference sample, as is the case in the Tophat kernel. But, for a general kernel, there is no simple and obvious form for the error. However, assuming that both the measured differential cross-section and its error should be approximately independent of the choice of kernel, it is possible to obtain a tentative expression for the the error using an arbitrary kernel:

$$\begin{aligned}
 d\sigma^{\text{GK}}(\mathbf{x}) &\simeq d\sigma^{\text{TK}}(\mathbf{x}) & (5.31) \\
 \Delta d\sigma^{\text{GK}}(\mathbf{x}) &\simeq \Delta d\sigma^{\text{TK}}(\mathbf{x}) \\
 &= \frac{\sqrt{N_{r_0^{\text{TK}}}}}{\mathcal{L}V'_n(r_0^{\text{TK}})} \\
 &= \sqrt{\frac{d\sigma^{\text{TK}}(\mathbf{x})}{\mathcal{L}V'_n(r_0^{\text{TK}})}} \\
 &\simeq \sqrt{\frac{d\sigma^{\text{GK}}(\mathbf{x})}{\mathcal{L}V'_n(r_0^{\text{TK}})}}. & (5.32)
 \end{aligned}$$

Hence, it is asserted that the error on the differential cross-section varies as the square root of the differential cross-section itself. Unfortunately, there is no easy way to relate the Tophat kernel length scale, r_0^{TK} , to that of another kernel, r_0^{GK} , and so it is not possible to evaluate the last expression exactly. But, so long as the same value of r_0 is used for any single data event, this will not affect the results of the parabolic fit, as it will scale the error on each of the points on the fit equally.

The effectiveness of expression 5.32 is tested by plotting the values of χ^2

obtained from parabolic fits to the differential cross-sections obtained with different kernels. As r_0^{TK} is not known, neither is $V'_n(r_0^{\text{TK}})$; the normalisations given in equations 5.15 and 5.17 are used on the grounds that they should be of the right order of magnitude. Figure 5.4 shows the plots comparing the χ^2 values obtained with the Tophat, Gaussian and Cauchy kernels. Each plot shows χ^2 values from 5000 Standard Model events fitted against $\alpha_W(\equiv \lambda)$ model reference samples; each plot shows results obtained using the five 183GeV samples, and also using the seven 189GeV samples.

It can be seen from the plots that the shapes of the χ^2 values obtained with the Gaussian and Cauchy kernels have the correct distributions[62], although the errors for both are overestimated (but, as noted above, this makes no difference to the fitted paraboli). It is worth noting that the χ^2 plots were made using a global value of r_0 , but demonstrates that the error estimation would be reasonable even if different values of r_0 were used for individual events. Examples of the paraboli obtained at different data points using individual values of r_0 were previously shown in figure 5.3, further demonstrating that the error estimation seems reasonable.

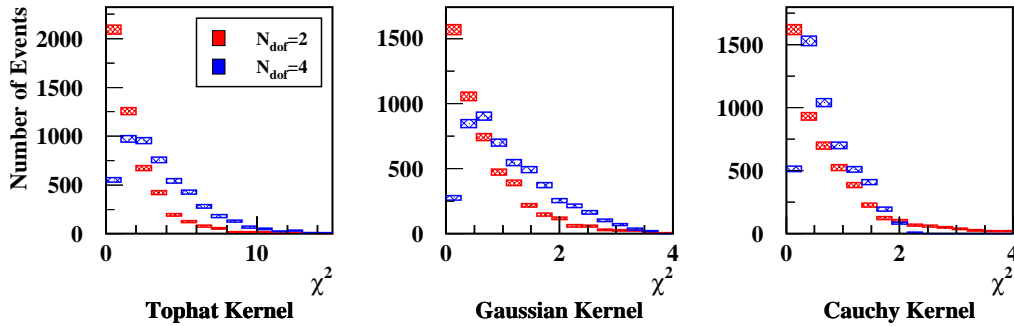


FIGURE 5.4: χ^2 distributions, comparing the values obtained using the Gaussian and Cauchy kernels with an approximate error and those obtained using the Tophat kernel with a Poisson error.

5.3.2 COMPARING THE DIFFERENT KERNELS

The studies to determine the most effective kernel are performed using simulated data samples of Monte Carlo events (details of all the Monte Carlo samples used in the analysis presented in this thesis are given in Appendix A). The samples are taken at random from a large Monte Carlo sample using a “quick and dirty” random number generator[63]. In this way, any internal ordering in the parent sample will be removed from the subsample; furthermore, this procedure allows for a subsample from a given file to be completely and unambiguously specified by its required size and the number upon which the random selection is seeded.

In order to evaluate the different kernels, it is necessary to compare their fitted results. Unfortunately there is no obvious correspondence between the values of r_0 for each kernel; i.e., what is the best value of r_0 for the Tophat kernel need not be the best value for the Gaussian or Cauchy kernels. Therefore it is necessary to investigate the behaviour with changing r_0 independently for each kernel, and only then compare the best results.

The only parameter when using the Tophat kernel is the length scale defining the volume. Appropriate values of r_0 are limited by the statistics in the reference samples; there is a trade off between having large statistical fluctuations when r_0 is small—possibly resulting in an unphysical zero cross-section—and losing sensitivity to the shape of the distribution as r_0 becomes large. To find the best balance between these, the values of r_0 are defined in terms of the population of the reference samples in the vicinity of the data points. This is achieved by the requirement that for each different reference sample there must be a certain number, $N_{RP/DP}$, of reference events within the test volume for each data event. This defines a value, r_0^{MIN} , for each data point for any given value of $N_{RP/DP}$.

For the Gaussian and Cauchy kernels, it is less obvious how to relate the size of r_0 to the local population in the reference samples. However, the value of $r_0^{\text{MIN}}(\mathfrak{X}_i^{\text{DATA}})$, defined for use with the Tophat kernel, does give a measure of the population in the vicinity of a data point at position $\mathfrak{X}_i^{\text{DATA}}$, so that a population-

based value of r_0 may be obtained as a product of r_0^{MIN} and a scale factor, f_{r_0} . This means that there is an additional—although not independent—degree of freedom, f_{r_0} , which must be investigated.

The simplest use of the value of r_0 is to have a single value for all the data events; but, as previously mentioned, there is nothing to say that the data events should not have different values of r_0 . When using a single global value the largest value of r_0^{MIN} out of all the data events is taken, thereby ensuring that a differential cross-section of zero may never occur; when using individual r_0 s, each event point takes its own value of r_0^{MIN} .

It is important to remember that the value of r_0 is always constant for any particular data event; i.e., the value of r_0 does not change for each different reference sample (although this may be a viable extension).

Figure 5.5 shows the results and standard deviation obtained by fitting fifty data-sample sized samples—consisting of fully reconstructed simulated Standard Model events—to the α -parameters. There is a lot of information in this plot; for the Tophat Kernel (the top four pairs of points in each column) only $N_{RP/DP}$, the population in the elemental volume, is varied to vary the value of r_0 ; for the Gaussian and Cauchy kernels (the rest of the points), the population and scale factor, f_{r_0} , are each varied independently. Furthermore, for each value of r_0 both global values (the open points), and individual values (the filled points) are tested.

It can be seen from figure 5.5 that both the Tophat and Gaussian kernels are capable of giving reasonable results; the Cauchy kernel seems biased in all cases. That the Cauchy kernel gives the worst performance is not surprising when considering its form; its tails are very much more pronounced than the other kernels, and so events which are further from the test point will get higher weighting than with the other kernels. Comparing the best fit results for individual and global r_0 values, there is little to choose between them. Individual values are used, simply for the aesthetic reason that otherwise the data point which fits least well with the reference samples dictates the length scale for all the other data points.

Again, there is little difference between the best results from the Gaussian and Tophat kernels; the Gaussian kernel is used for the measurements presented in this thesis for two reasons: firstly, it should never measure a null differential cross-section from a finite sample, which can happen with the Tophat kernel (this will become more significant when very low statistics samples are used in the background evaluation); secondly, all things being equal, it is the more interesting method as it is an alternative to the traditional binned fits which feature at some point in most of the other OPAL T.G.C. analyses.

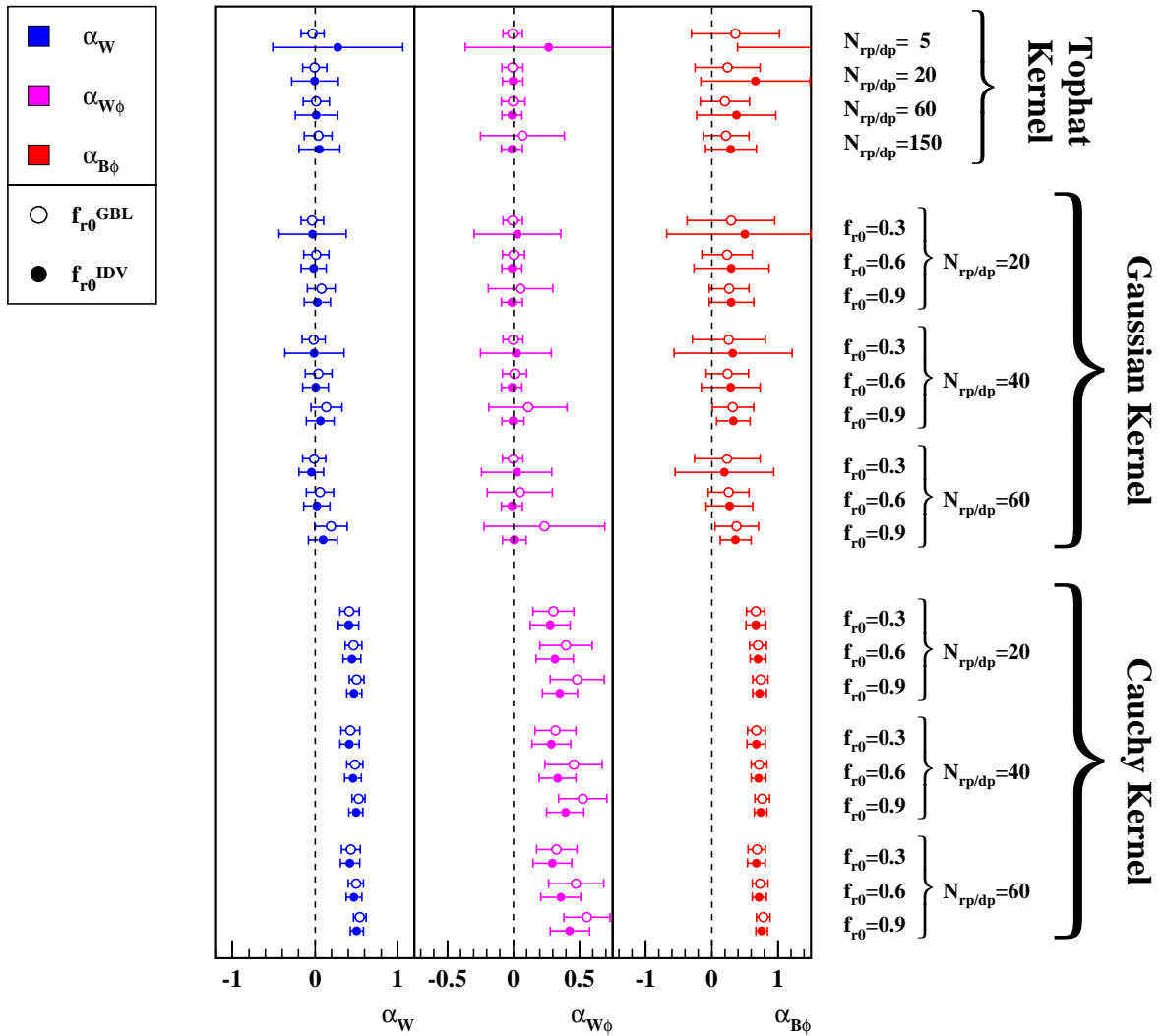


FIGURE 5.5: Average fit results and their standard deviations obtained by fitting 50 simulated Standard Model data samples to the α -parameters, using different kernels with different methods of choosing the length scale, r_0 ; the open points are those using a single, global value of r_0 , whereas the filled points are those using individual values for each data point. Note the different scales for the different parameters. The dashed line gives the true T.G.C. value of the samples.

5.3.3 OPTIMIZATION OF r_0

Having chosen the kernel and method for selecting the length scale, the actual values of the population measure, $N_{RP/DP}$, and the scale value, f_{r_0} , are investigated more fully in order to, somewhat, optimize their values. At both $\sqrt{s} = 183\text{GeV}$ and $\sqrt{s} = 189\text{GeV}$ fifty data-sample sized simulated samples were fitted using different values of $N_{RP/DP}$ and f_{r_0} . The average fitted values and average errors are shown in figure 5.6 and 5.7.

The parameters which give the worst fit results are $\alpha_{B\phi}$ at 183GeV and $\Delta\kappa_\gamma$ at 189GeV, which is expected as they have the lowest variation of cross-section with T.G.C. strength; the other parameters give good results for most combinations of $N_{RP/DP}$ and f_{r_0} tested. In figures 5.6 and 5.7 the boxes highlighted in yellow indicate that average fitted values and errors are acceptable; out of these the combinations

$$\begin{aligned} N_{RP/DP} &= 40 \\ f_{r_0} &= 0.5 \end{aligned}$$

at $\sqrt{s} = 183\text{GeV}$ and

$$\begin{aligned} N_{RP/DP} &= 60 \\ f_{r_0} &= 0.5 \end{aligned}$$

at $\sqrt{s} = 189\text{GeV}$ were chosen for use in the analysis of this thesis. For these values of $N_{RP/DP}$ & f_{r_0} the average fitted values from figure 5.6 & 5.7 and associated standard deviations are as follow:

$$\begin{aligned} \overline{\alpha_W} &= -0.002 \pm 0.022 & \sigma_{\alpha_W} &= 0.155 \\ \overline{\alpha_{W\phi}} &= -0.011 \pm 0.011 & \sigma_{\alpha_{W\phi}} &= 0.079 \\ \overline{\alpha_{B\phi}} &= -0.245 \pm 0.072 & \sigma_{\alpha_{B\phi}} &= 0.505 \end{aligned}$$

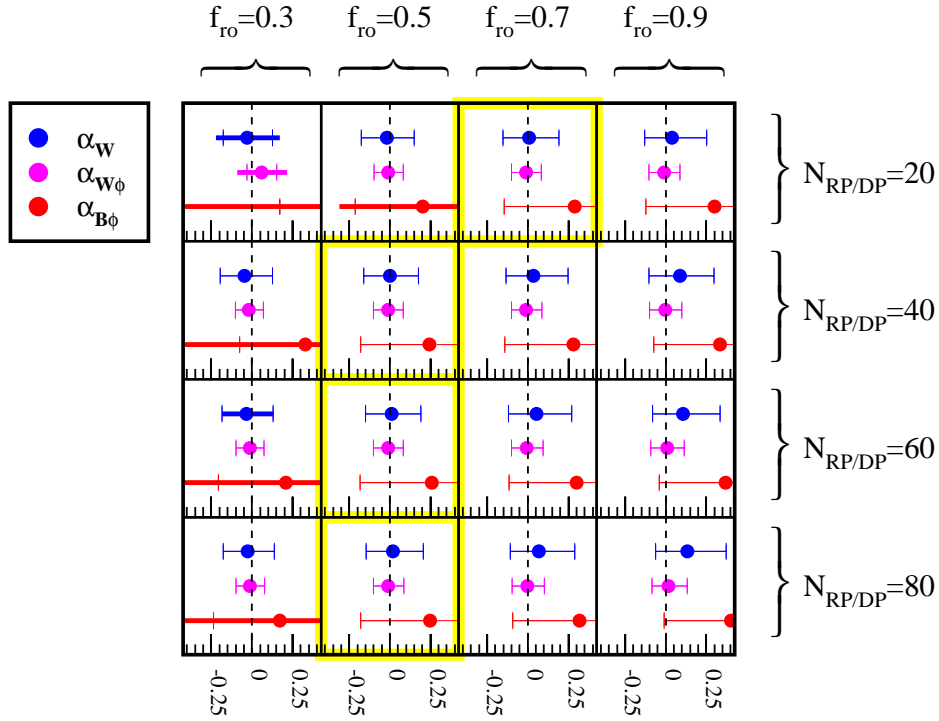


FIGURE 5.6: Mean and standard deviation of fitted values of fifty Standard Model Monte Carlo samples at 183GeV using the Gaussian kernel with various values of $N_{RP/DP}$ and f_{r_0} . The average fit errors of the fifty fitted values are given by the error bars; a thicker line extending beyond the error bars indicates that the average errors do not contain 68% or more of the fitted values, and the extent of the thicker lines indicates how much the errors must be scaled such that they do. The acceptable combinations of $N_{RP/DP}$ and f_{r_0} are highlighted. The dashed line gives the true T.G.C. value of the samples.

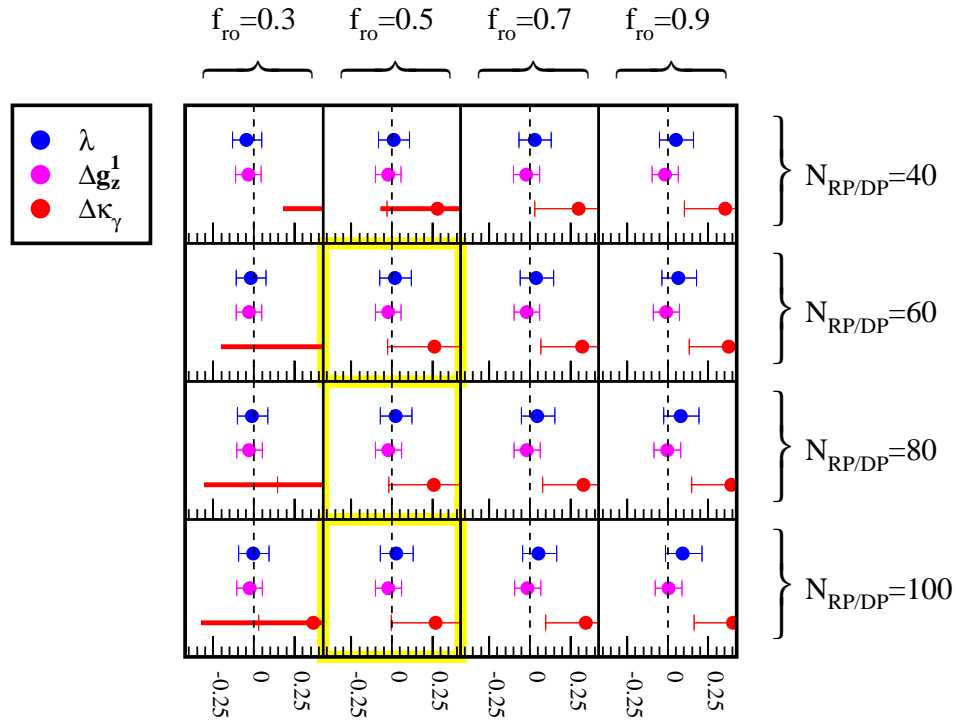


FIGURE 5.7: Mean and standard deviation of fitted values of fifty Monte Carlo samples at 189GeV using the Gaussian kernel with various values of $N_{RP/DP}$ and f_{r_0} . See figure 5.6 for a description of the information contained in the plot.

at $\sqrt{s} = 183\text{GeV}$, and

$$\begin{aligned} \bar{\lambda} &= 0.019 \pm 0.011 & \sigma_{\lambda} &= 0.074 \\ \overline{\Delta g_Z^1} &= -0.023 \pm 0.010 & \sigma_{\Delta g_Z^1} &= 0.068 \\ \overline{\Delta \kappa_{\gamma}} &= 0.264 \pm 0.041 & \sigma_{\Delta \kappa_{\gamma}} &= 0.287. \end{aligned}$$

at $\sqrt{s} = 189\text{GeV}$.

5.3.4 N.N.M.L. FITTING TO DIFFERENT VALUES OF THE T.G.C. PARAMETERS

To test the method over a range of T.G.C. strengths, fits are performed of large simulated test samples (i.e., approximately ten times the data sample at each energy) which were generated with anomalous coupling strengths. The simulated samples are taken from the reference sample which would be used for fitting the data sample. To avoid correlations, the events used in the test sample at one value are also omitted from the reference samples for all other values. This means that the reference samples used are smaller than those actually used in the analysis, and the fitted results will, therefore, have a larger associated error.

Figure 5.8 shows graphs of the fitted results for the main parameter sets used at $\sqrt{s} = 183\text{GeV}$ and $\sqrt{s} = 189\text{GeV}$ (i.e., the α -parameters and the λ - Δg_Z^1 - $\Delta \kappa_{\gamma}$ set, respectively). In this figure the solid line gives the weighted least squares fit to these points, so that the equation of the line is

$$\alpha^{\text{FIT}} = \sigma \alpha^{\text{TRUE}} + \beta \tag{5.33}$$

where σ gives the slope of the line, and, therefore, gives the response of the method, and β gives the extent of any overall bias; the dashed line indicates where this line would lie if the method were perfect.

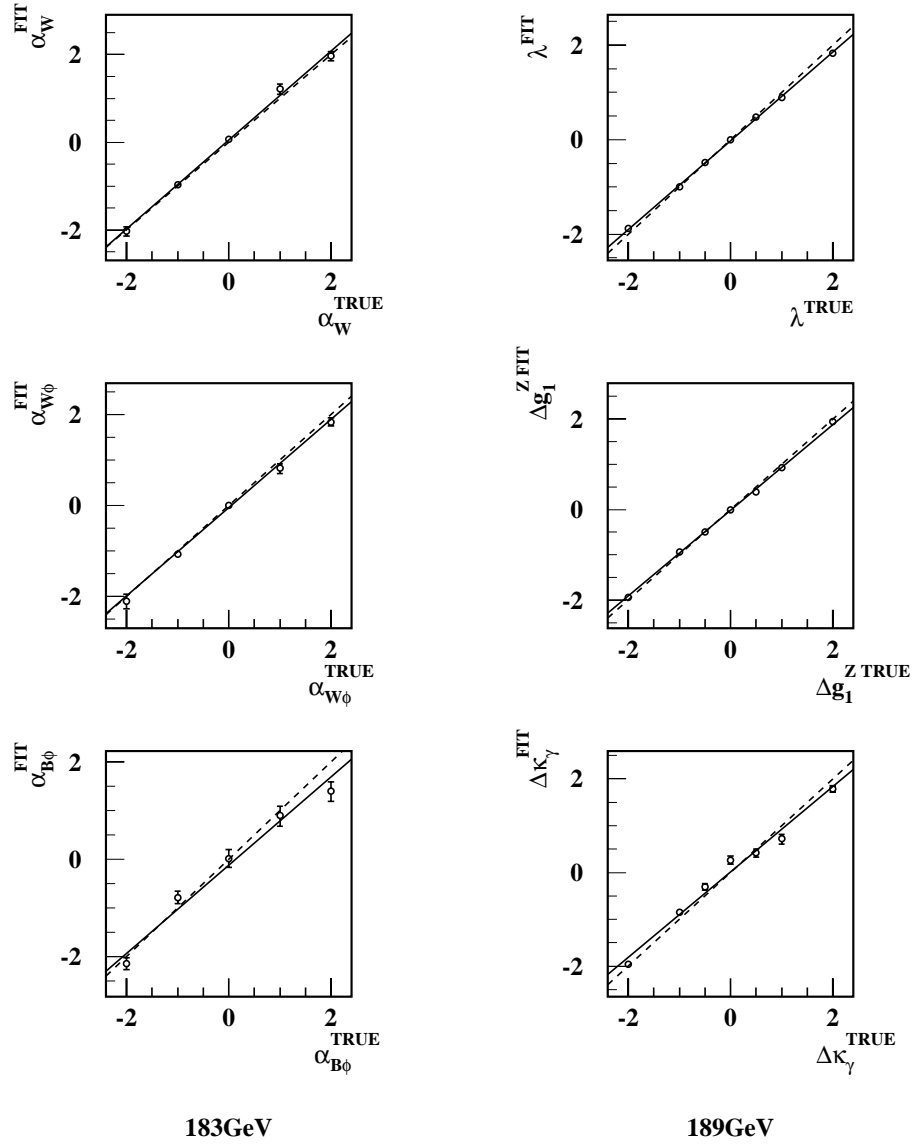


FIGURE 5.8: Bias plots of the main parameters at $\sqrt{s} = 183 \text{ GeV}$ and $\sqrt{s} = 189 \text{ GeV}$. The solid line shows the weighted least squares fit to the fitted values, and the dashed line shows the line which would be given by a perfect fit.

The $\alpha_{B\phi}$ and $\Delta\kappa_\gamma$ parameters again give the worst fits; all the other parameters have a good response over the range of values and show no bias.

In addition to the main parameter sets OPAL has reference samples at $\sqrt{s} = 183\text{GeV}$ for three other parameters: Δg_Z^1 , $\Delta\kappa$ and $\Delta\kappa_\gamma^{\text{HISZ}}$. Similar plots for these parameters are shown in figure 5.9. Fits to these parameters, again, show a good response and no bias.

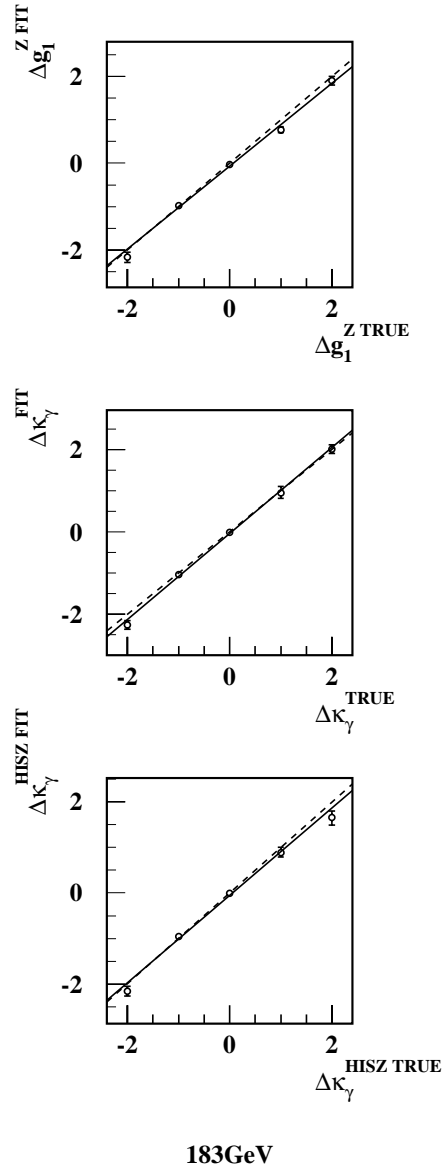


FIGURE 5.9: Bias plots of other *T.G.C.* parameters at $\sqrt{s} = 183\text{ GeV}$. The solid and dashed lines are as in figure 5.8.

5.4 INCORPORATING ALL ACCEPTED PROCESSES

The main reference samples, in general, will not contain every type of process which may be accepted; for example, the 4-fermion EXCALIBUR samples used by OPAL do not contain Z^0/γ , $\gamma\gamma$ or any events with an electron-positron pair in the final state. If ignored entirely this will introduce a bias into the fitted T.G.C. strength, due to both the accepted cross-section being larger than expected, and also due to the assumed shape of the differential cross-section being incorrect.

5.4.1 CORRECTING THE TOTAL CROSS-SECTION

For the simplest case where the extra accepted events do not affect the shape of the angular distribution the extra accepted events effectively scale the total cross-section. This cannot affect the results of the ordinary log likelihood fit, as this does not make use of the rate information. It will, however, effect the results from the extended fit. To compensate for this effect it is only necessary to add the expected number of events from the additional processes to that from the main reference process, so that the extended log likelihood now becomes

$$\mathcal{L}_E(\alpha) \sim \mathcal{L}(\alpha) + \lambda_{\text{INC}}(\alpha) - N_{\text{DATA}} \ln \lambda_{\text{INC}}(\alpha), \quad (5.34)$$

where

$$\lambda_{\text{INC}} = \sum^{\text{All processes}} \lambda_i. \quad (5.35)$$

It is assumed that the processes other than that of the main reference process have no T.G.C. dependence, which is true for OPAL's 4-fermion samples.

5.4.2 INCORPORATING THE INCLUSIVE DIFFERENTIAL CROSS-SECTION

To properly incorporate all accepted processes it is necessary to take account of their positions in the phase-space. The method can be extended in a coherent way simply by adding a contribution to the differential cross-section which must be evaluated from reference samples describing the additional processes.

Considering, for ease of description, a single additional process, the differential cross-section distribution may again be defined as in equation 5.10. Then the inclusive differential cross-section reference distribution, incorporating the main reference sample, $d\sigma_0$, and that of the additional process, $d\sigma_X$, is given by

$$d\sigma_{\text{INC}} = d\sigma_0 + d\sigma_X \quad (5.36)$$

$$= \frac{1}{\mathcal{L}_0} \sum_{j=1}^{N_0} \delta(\mathfrak{x} - \mathfrak{x}_j^0) + \frac{1}{\mathcal{L}_X} \sum_{j=1}^{N_X} \delta(\mathfrak{x} - \mathfrak{x}_j^X) \quad (5.37)$$

This differential cross-section may then be used in equation 5.12 to give the measured inclusive differential cross-section, now generalised to many processes:

$$d\sigma_{r_0}^{\text{INC}}(\mathfrak{x}) = \sum_{\text{All processes}} \frac{1}{\mathcal{L}_i} \sum_{j=1}^{N_i} \Delta(\mathfrak{x}_j^i - \mathfrak{x}; r_0) \quad (5.38)$$

The inclusive total cross-section is simply the sum of the cross-sections from each of the relevant processes,

$$\sigma^{\text{INC}} = \sum_{\text{All processes}} \sigma^i. \quad (5.39)$$

The inclusive cross-section will also follow a quadratic form, with the additional processes simply contributing a constant term, and so the cross-section functions and the log-likelihoods may be formed as before.

Figure 5.10 shows the result of fitting fifty data-sample sized samples of simulated Standard Model events to the α -parameters using the N.N.M.L. in

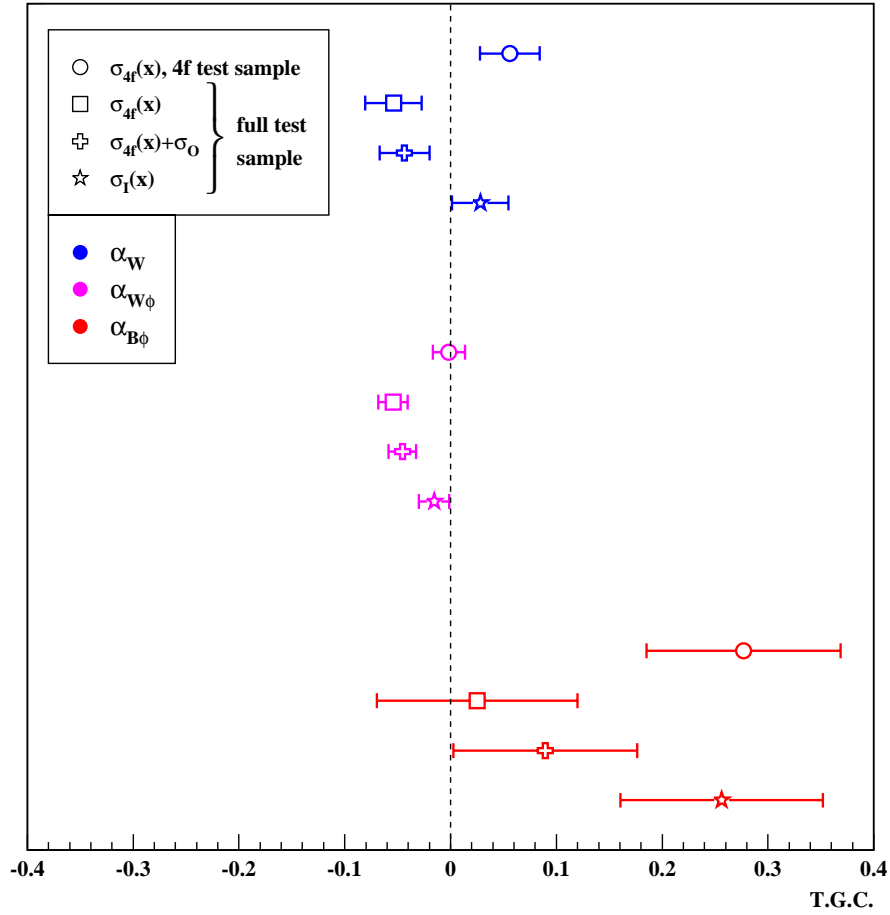


FIGURE 5.10: Plot showing the central value and associated error from fifty simulated samples, fitted using different cross-sections obtained from different combinations of samples; $\sigma_{4f}(x)$ indicates the standard 4-fermion reference samples; σ_O indicates an additional total cross-section (no shape information) for other processes; $\sigma_I(x)$ indicates the total inclusive cross-section, such that $\sigma_I(x) = \sigma_{4f}(x) + \sigma_O(x)$. The dashed line gives the true T.G.C. value of the samples.

different analysis modes. Each point in the plot shows the central value and associated error of the fit results from fifty 57pb^{-1} Standard Model samples. Two types of simulated sample are used; 4-fermion samples, taken from the normal reference samples, and inclusive samples where these 4-fermion events are supplemented by events arising from other processes. For each model, the topmost point shows the result of fitting 4-fermion test samples against 4-fermion reference samples; for the second point, inclusive test samples were fitted against 4-fermion reference samples, which shows the bias that the additional accepted events would contribute; the third point fits inclusive samples against 4-fermion samples but uses the correct number of expected events in the extended log likelihood; and the fourth point shows the results of fitting inclusive samples against inclusive reference samples.

In all cases, fitting using the inclusive sample significantly corrects the bias introduced by the other accepted events.

5.5 THE MULTI-PARAMETER N.N.M.L. METHOD

The single parameter fits fix all other T.G.C. parameters to their Standard Model values, but there is no reason for the anomalous couplings to be manifest in this way. In particular, it would be ideal to simultaneously measure the three independent parameters which conserve the $SU(2)_L \times U(1)_Y$ symmetry of the Lagrangian; i.e., the α -parameters or the equivalent λ - Δg_Z^1 - $\Delta \kappa_\gamma$ set.

5.5.1 THE MULTI-PARAMETER LIKELIHOOD FUNCTION

The Near Neighbour method of measuring the differential cross-section from a reference sample is identical for the multi-parameter fits to that for the single-parameter fits; the difference lies in the function to which these measured cross-sections are fit.

The single-parameter differential cross-section given in equation 5.19 may be simply extended to give that as a function of three T.G.C. parameters (shown here for the α -parameters):

$$\begin{aligned}
 d\sigma(\mathfrak{x}, \alpha_W, \alpha_{W\phi}, \alpha_{B\phi}) = & \quad d\sigma^{\text{SM-SM}}(\mathfrak{x}) & (5.40) \\
 & + \alpha_W^2 d\sigma^{\text{W-W}}(\mathfrak{x}) & + \alpha_W d\sigma^{\text{SM-W}}(\mathfrak{x}) \\
 & + \alpha_{W\phi}^2 d\sigma^{\text{W}\phi\text{-W}\phi}(\mathfrak{x}) & + \alpha_{W\phi} d\sigma^{\text{SM-W}\phi}(\mathfrak{x}) \\
 & + \alpha_{B\phi}^2 d\sigma^{\text{B}\phi\text{-B}\phi}(\mathfrak{x}) & + \alpha_{B\phi} d\sigma^{\text{SM-B}\phi}(\mathfrak{x}) \\
 & + \alpha_W \alpha_{W\phi} d\sigma^{\text{W-W}\phi}(\mathfrak{x}) \\
 & + \alpha_{W\phi} \alpha_{B\phi} d\sigma^{\text{W}\phi\text{-B}\phi}(\mathfrak{x}) \\
 & + \alpha_{B\phi} \alpha_W d\sigma^{\text{B}\phi\text{-W}}(\mathfrak{x}).
 \end{aligned}$$

Equation 5.40 describes a hyperparabola in the phase-space of the three T.G.C.

parameters. The last three terms give the correlations between the T.G.C. parameters, whereas all the other terms describing the hyperparabola are the same as in the single parameter fits. Therefore, in addition to those required to measure the single parameter cross-section, it is necessary to use a minimum of three extra reference samples—one for each unique pairing of T.G.C. parameters—in order to evaluate these correlation terms.

As with the single parameter case, the probability density simply follows from the differential cross-section:

$$\rho_{r_0}(\mathbf{x}, \alpha_W, \alpha_{W\phi}, \alpha_{B\phi}) = \frac{d\sigma(\mathbf{x}, \alpha_W, \alpha_{W\phi}, \alpha_{B\phi})}{\sigma(\alpha_W, \alpha_{W\phi}, \alpha_{B\phi})}. \quad (5.41)$$

Hence the negative log likelihood is given by

$$\mathcal{L}(\alpha_W, \alpha_{W\phi}, \alpha_{B\phi}) = \sum_{i=1}^{N_{\text{DATA}}} -\ln \rho_{r_0}(\mathbf{x}_i, \alpha_W, \alpha_{W\phi}, \alpha_{B\phi}) \quad (5.42)$$

and the negative extended log likelihood by

$$\begin{aligned} \mathcal{L}_E(\alpha_W, \alpha_{W\phi}, \alpha_{B\phi}) &= \mathcal{L}(\alpha_W, \alpha_{W\phi}, \alpha_{B\phi}) + N(\alpha_W, \alpha_{W\phi}, \alpha_{B\phi}) \\ &\quad - N_{\text{DATA}} \ln N(\alpha_W, \alpha_{W\phi}, \alpha_{B\phi}). \end{aligned} \quad (5.43)$$

To be explicit, the expected number of events, $N(\alpha_W, \alpha_{W\phi}, \alpha_{B\phi})$, is given by:

$$\begin{aligned} N(\alpha_W, \alpha_{W\phi}, \alpha_{B\phi}) &= \mathcal{L}^{\text{DATA}} \sigma(\alpha_W, \alpha_{W\phi}, \alpha_{B\phi}) \\ &= \mathcal{L}^{\text{DATA}} (\sigma^{\text{SM-SM}} \\ &\quad + \alpha_W^2 \sigma^{\text{W-W}} + \alpha_W \sigma^{\text{SM-W}} \\ &\quad + \alpha_{W\phi}^2 \sigma^{\text{W}\phi\text{-W}\phi} + \alpha_{W\phi} \sigma^{\text{SM-W}\phi} \\ &\quad + \alpha_{B\phi}^2 \sigma^{\text{B}\phi\text{-B}\phi} + \alpha_{B\phi} \sigma^{\text{SM-B}\phi} \\ &\quad + \alpha_W \alpha_{W\phi} \sigma^{\text{W-W}\phi} \\ &\quad + \alpha_{W\phi} \alpha_{B\phi} \sigma^{\text{W}\phi\text{-B}\phi} \\ &\quad + \alpha_{B\phi} \alpha_W \sigma^{\text{B}\phi\text{-W}}). \end{aligned} \quad (5.44)$$

The multi-parameter fits may incorporate any additional processes in exactly the same way described for the single-parameter fit.

5.5.2 MEASURING THE HYPERPARABOLA PARAMETERS

As with the single parameter fit, for each data point several differential cross-sections are measured from the reference samples; these are then used in a weighted least squares fit[62], but, in this case, to the multi-parameter differential cross-section of equation 5.40. The same is done for the total cross-sections of the reference samples, and then the method proceeds as before, using the MINUIT package to find the best values of the T.G.C. parameters.

However, the hyperparabola parameters are constrained in that, physically, the cross-section function must be positive definite for all values of the T.G.C. parameters. Because the measured cross-sections have an associated error, the conditions for this to be true[64] are not always satisfied. Using a simple unconstrained fit, these events must be discarded, and, as such events are liable to be clustered in regions of phase-space, this will inevitably lead to a bias (which will be illustrated in the following section). Distributions of the events which fail the fit for both the data sample and a Standard Model Monte Carlo sample are shown in figure 5.11. The number of events which give unphysical cross-section decreases as the value of the length scale, r_0 , increases, which indicates that the effect is indeed due to the error on the measured differential cross-sections; the proportion of events which are discarded varies roughly between 15–30% for reasonable values of r_0 (again, “reasonable values” are discussed and evaluated in the following section).

Attempts were made to recover these events using the MINUIT package with appropriate constraints on the hyperparabola parameters. Unfortunately, the constraints used were too stringent and led to larger biases than simply discarding the events, and so this approach was not pursued. However, this could well be a fruitful area for further study.

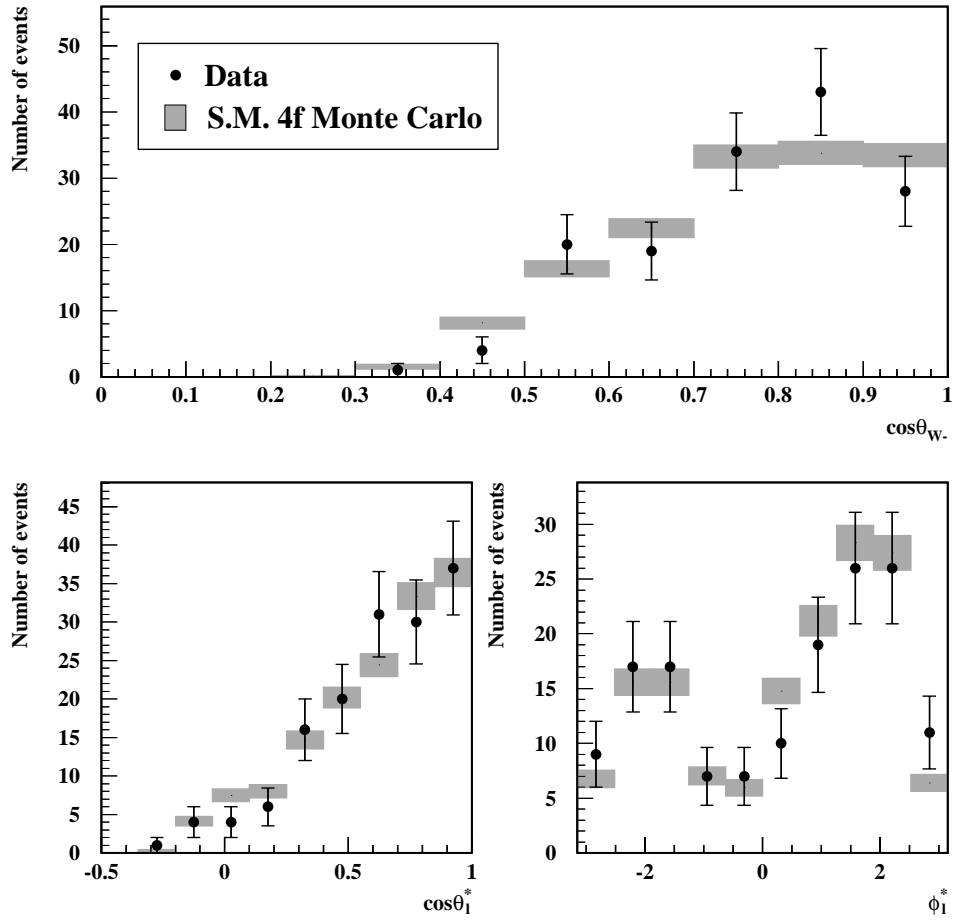


FIGURE 5.11: Plot showing the distributions of the events which fail the multi-parameter fit, for the data sample and for a Standard Model 4-fermion Monte Carlo sample.

5.5.3 PERFORMANCE AND OPTIMIZATION OF THE MULTI-PARAMETER FITS

The necessary correlation reference samples—i.e., with two non-zero T.G.C. parameters—are only available at $\sqrt{s} = 189\text{GeV}$, so that the multi-parameter fits are only performed on the 1998 data set and only for the $\lambda\text{-}\Delta g_Z^1\text{-}\Delta\kappa_\gamma$ parameter set.

When evaluating the performance of the triple-parameter N.N.M.L. it is necessary, once again, to look at a range of values of the length scale, r_0 . Due to time constraints and the added complexity of comparing results from three parameters simultaneously, the method of choosing r_0 was not investigated as thoroughly as with the single parameter fits; a single sample, approximately 10 times the data sample and comprised of simulated Standard Model events, was analyzed using several values of the population measure, $N_{RP/DP}$, but with no scale factor, f_{r_0} , applied.

Figure 5.12 shows several plots of the 95% confidence level limit (C.L.L.) contours from the negative extended log likelihood obtained using different values of $N_{RP/DP}$. In each of these plots, the contour is shown for two of the parameters, whilst the other is at its fitted value; the fitted value of the displayed parameters is indicated on each of the plots. From these, a value of $N_{RP/DP} = 100$ is chosen for the multi-parameter analysis.

It should be noted that, in all cases, the 95% C.L.L. contours for the $\lambda - \Delta g_Z^1$ parameters exclude the Standard Model value, although all of the single parameter values are consistent with the Standard Model values within this limit. In this respect, the multi-parameter fits could well be improved, particularly for the Δg_Z^1 parameter. This may be due to the discarded events leading to a bias; the simplest way to improve the performance of this fit would probably be to include more reference files with correlated T.G.C. parameter values, rather than the minimum of three which are available at present. In addition, further work may be done to recover the discarded events using a constrained fit to the hyperparabola parameters.

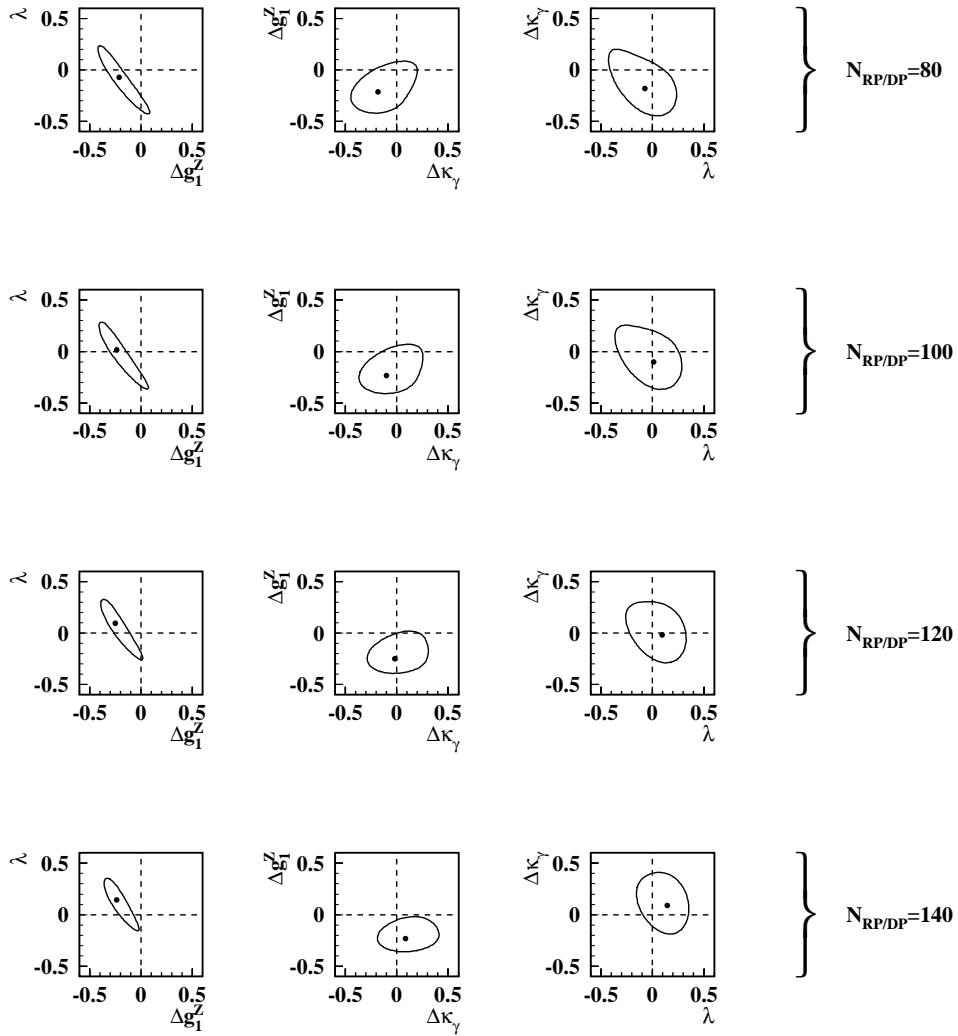


FIGURE 5.12: 95% C.L.L. contours for the λ - Δg_Z^1 - $\Delta \kappa_\gamma$ parameters from the analysis of a large Standard Model sample of events at $\sqrt{s} = 189\text{GeV}$. Each row of plots shows the fit results using a different value of $N_{RP/DP}$. For each plot, the contour and fitted values for two parameters are displayed whilst the third is at its fitted value. The Standard Model position is indicated by the dotted lines.

5.6 INCORPORATING A SYSTEMATIC ERROR IN THE ANALYSIS

Any experimental measurement will have an associated systematic error. This means that the true probability distribution is not that given by the likelihood functions, but instead by the convolution of the likelihood functions with the additional probability function of the systematic uncertainty[62]. It is this convolved probability which should then be used in the negative log likelihood fits.

With such a complicated analysis as that described in this chapter there will probably be many sources of systematic uncertainty (these are described in chapter 7), so that the systematic probability function should be approximately Gaussian, by the Central Limit Theorem[62].

Therefore, the likelihood function of equation 5.24 will become

$$\mathcal{L}^S(\alpha) \equiv -\ln \left(\int_{-\infty}^{\infty} d\alpha' L(\alpha') \exp \left\{ \frac{-(\alpha - \alpha')^2}{2\varepsilon_\alpha^2} \right\} \right) \quad (5.45)$$

where ε_α is the total systematic error.

It is these functions which should be used in the negative log likelihood fit to find the measured T.G.C. parameters. The fit function (i.e., $L(\alpha)$ in equation 5.45) is too complicated for these integral to be performed analytically, and so it must be solved using numerical computational techniques[63].

In addition to the systematic uncertainty from the negative log likelihood function, there will also be a systematic uncertainty in the expected total cross-section, and, hence, the expected number of accepted events. This means that the negative extended log likelihood function will become

$$\mathcal{L}_E^S(\alpha) \equiv -\ln \left(\int_{-\infty}^{\infty} d\alpha' L(\alpha') \exp \left\{ \frac{-(\alpha - \alpha')^2}{2\varepsilon_\alpha^2} \right\} \right. \\ \left. \times \int_0^{\infty} dN'_{\text{DATA}} P(N'_{\text{DATA}}; \lambda) \exp \left\{ \frac{-(N_{\text{DATA}} - N'_{\text{DATA}})^2}{2\varepsilon_N^2} \right\} \right),$$

where ε_N is the error on the accepted number of events. The Poisson probability function for the total number of accepted events may be very well

approximated by a Gaussian, so that the second integral in equation 5.46 may be performed analytically, using the identity

$$\int_{-\infty}^{\infty} dx' \frac{1}{\sqrt{2\pi a}} \exp\left\{\frac{-x'^2}{a}\right\} \frac{1}{\sqrt{2\pi b}} \exp\left\{\frac{-(x-x')^2}{b}\right\} = \frac{1}{\sqrt{2\pi(a+b)}} \exp\left\{\frac{-x^2}{a+b}\right\}. \quad (5.46)$$

This expression is not exactly appropriate, as the integral runs from $-\infty$ to ∞ whereas the Gaussian approximation to the Poisson distribution has a lower limit of zero; but the width of the distribution and the statistical error on the number of events are sufficiently small in comparison to the position of the peak of the distribution that the difference will not be appreciable. Hence the complete negative extended log likelihood function to be minimized is

$$\mathcal{L}_E^S(\alpha) \equiv -\ln \left(\int_{-\infty}^{\infty} d\alpha' L(\alpha') \exp\left\{\frac{-(\alpha-\alpha')^2}{2\varepsilon_\alpha^2}\right\} \exp\left\{\frac{-(N_{\text{DATA}}-\lambda(\alpha))^2}{2(\lambda(\alpha)-\varepsilon_\sigma^2)}\right\} \right). \quad (5.47)$$

This function gives the best measurement of the T.G.C. parameters incorporating all the available information.

CHAPTER 6

THE MEASUREMENT OF THE T.G.C.S

To recap from chapter 2, the principal measurements of this thesis involve the two, equivalent sets of $SU(2) \times U(1)$ invariant triple gauge coupling parameters:

- $\alpha_W, \alpha_{W\phi}$ and $\alpha_{B\phi}$,
- $\lambda, \Delta g_Z^1$ and $\Delta\kappa_\gamma$.

Additionally there are simulated samples generated with a nominal collision energy of 183GeV for the following parameters:

- $\Delta g_Z^{1\dagger}, \Delta\kappa_\gamma^{\text{HISZ}}, \Delta\kappa$.

As the α -parameters and the λ - Δg_Z^1 - $\Delta\kappa_\gamma$ parameters are the main focus of this analysis, the log-likelihood plots for their measurements are grouped together; the log-likelihood plots for the additional parameters are then displayed subsequently.

Triple-parameter fits are presented for the 1998 data sample, with 95% C.L.L. contours to illustrate the correlations between the parameters.

[†] Although Δg_Z^1 appears in sets of parameters at both energies, it is not considered one of the main samples at $\sqrt{s} = 183\text{GeV}$ because the complete set of $SU(2)_L \times U(1)_Y$ invariant parameters are not covered without the λ and $\Delta\kappa_\gamma$ parameters.

6.1 MEASURED VALUES OF THE T.G.C. PARAMETERS

As detailed in chapter 4, §4.4.2, the selected data sample obtained by OPAL in 1997, when LEP ran at a collision energy of 183GeV and OPAL received 57.0fb^{-1} , comprises 247 events. The expected number of accepted events according to the Standard Model is 238.2. That selected in 1998, when LEP ran at 189GeV and OPAL received 183.1fb^{-1} , comprises 747 events. The expected number at this energy according to the Standard Model is 806.3.

The final fitted values of the α -parameters at $\sqrt{s} = 183\text{GeV}$ are

$$\begin{aligned}\alpha_{\text{W}} &= 0.012_{-0.240}^{+0.343} \pm 0.056 \\ \alpha_{\text{W}\phi} &= 0.039_{-0.128}^{+0.144} \pm 0.022 \\ \alpha_{\text{B}\phi} &= -0.423_{-0.345}^{+0.493} \pm 0.470\end{aligned}$$

and those for the λ - Δg_Z^1 - $\Delta\kappa_\gamma$ parameters at $\sqrt{s} = 189\text{GeV}$ are

$$\begin{aligned}\lambda &= -0.059_{-0.081}^{+0.086} \pm 0.061 \\ \Delta g_Z^1 &= -0.010_{-0.073}^{+0.076} \pm 0.054 \\ \Delta\kappa_\gamma &= 0.211_{-0.251}^{+0.314} \pm 0.210.\end{aligned}$$

The values of the additional parameters measured at $\sqrt{s} = 183\text{GeV}$ are

$$\begin{aligned}\Delta g_Z^1 &= 0.101_{-0.233}^{+0.252} \pm 0.061 \\ \Delta\kappa_\gamma^{\text{HISZ}} &= -0.102_{-0.201}^{+0.220} \pm 0.054 \\ \Delta\kappa &= -0.117_{-0.175}^{+0.191} \pm 0.210.\end{aligned}$$

The measured values are taken from the log-likelihood curves shown in section §6.2.4, generated with the full single parameter N.N.M.L. analysis incorporating the systematic error (the evaluation and inclusion of the systematic error are described in the following chapter). The first error on the values is statistical and is taken from the log-likelihood curves shown in §6.2.3 which are

from the full N.N.M.L. fit without including the systematic error. The second error is the systematic uncertainty on the fitted values.

The 95% C.L.L. obtained from the full N.N.M.L. fit with systematic error for the α -parameters at $\sqrt{s} = 183\text{GeV}$ are

$$-0.415 < \alpha_W < 0.726$$

$$-0.202 < \alpha_{W\phi} < 0.340$$

$$-1.135 < \alpha_{B\phi} < 2.011$$

and those for the λ - Δg_Z^1 - $\Delta\kappa_\gamma$ parameters at $\sqrt{s} = 189\text{GeV}$ are

$$-0.216 < \lambda < 0.116$$

$$-0.150 < \Delta g_Z^1 < 0.143$$

$$-0.247 < \Delta\kappa_\gamma < 0.859.$$

For the other parameters measured at $\sqrt{s} = 183\text{GeV}$ the limits are

$$-0.316 < \Delta g_Z^1 < 0.568$$

$$-0.484 < \Delta\kappa_\gamma^{\text{HSZ}} < 0.355$$

$$-0.449 < \Delta\kappa < 0.280.$$

6.2 LOG-LIKELIHOOD CURVES AND FITTED VALUES FROM DIFFERENT ANALYSIS MODES

Various different analysis modes were described in chapter 5. Several sets of log-likelihood curves are presented in this section, in order to illustrate the effect of using the inclusive cross-section—as described in §5.4 of chapter 5—and also the effect on the curves of the systematic uncertainty. In all the plots, the dashed line gives the log-likelihood curve from the fit to the angular distribution of the data, the dotted curve gives the log-likelihood curve from the fit to the total cross-section, and the solid line gives their sum, the extended log-likelihood curve.

In addition to results from the single-parameter fits, 95% C.L.L. contours from the triple-parameter fits of the 1998 data sample are also shown. Due to time constraints, the systematic uncertainties were not incorporated in the multi-parameter fits, and so the fitted parameter values are not quoted. The plots are included to show the correlations between the different parameters and are shown for the full, inclusive cross-section fit (§6.2.3).

6.2.1 THE BASIC N.N.M.L. FIT

The simplest measurement of the T.G.C.s uses the method and configuration described in §5.2 of chapter 5. The main features are as follows:

- A gaussian kernel
- Individual values of r_0 for each data event, depending on the population of the reference samples in the vicinity.
- The value of r_0 for any given data point is calculated by finding the

minimum radius to contain 40 reference events for the 183GeV data and 60 for the 189GeV data, and then scaling this radius by 0.5.

- No process other than those in the main reference samples is included in the analysis.

The log-likelihood curves for this simplest measurement are shown in figures 6.1 and 6.2. In the 1997 data there are two minima to the total cross-section log-likelihood curve, because there are more events in the data sample than the minimum expected number; conversely, there is a single minimum in that for the 1998 data because there are fewer than the minimum expected.

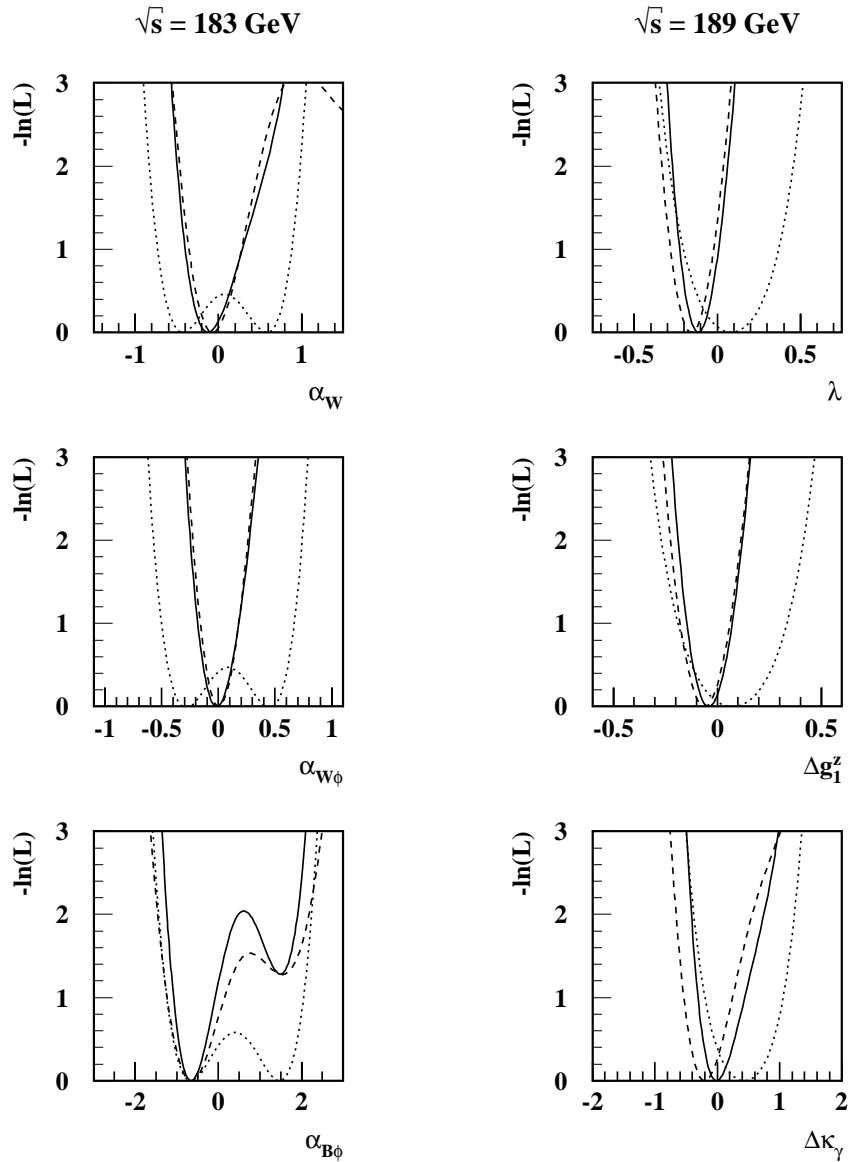


FIGURE 6.1: Log-likelihood curves for the main T.G.C. parameters measured using the basic N.N.M.L. fit to the 183 GeV and 189 GeV data. The dotted line gives the negative log likelihood curve from the total cross-section analysis, the dashed line gives that from the angular distribution analysis, and the solid line is their sum which is the negative extended log likelihood curve.

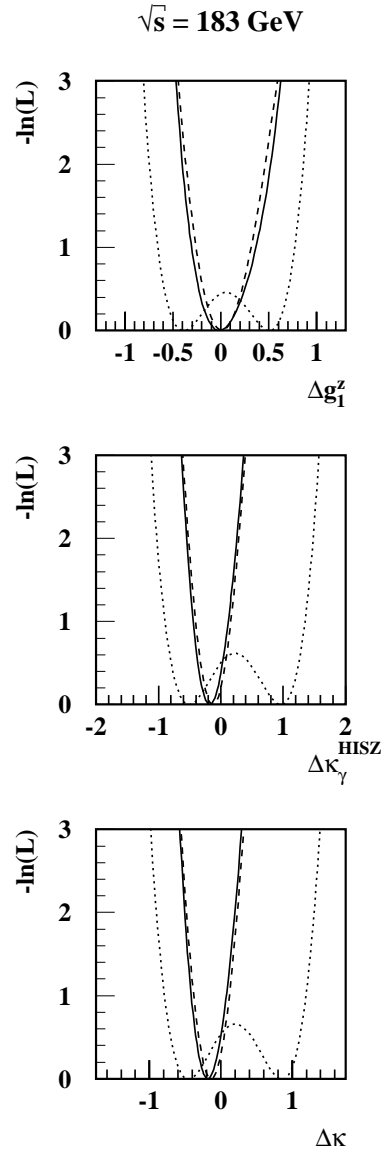


FIGURE 6.2: Log-likelihood curves for additional *T.G.C.* parameters measured using the basic *N.N.M.L.* on the 183GeV data.

6.2.2 INCORPORATING THE EXPECTED BACKGROUND LEVEL

The first level of sophistication is to account for the expected level of background in the extended log-likelihood fit, as described in section §5.4.1. Only the results of the extended log-likelihood fit are altered, and the modified log-likelihood curves are shown in figures 6.3 and 6.4. It can be seen from these figures that the local maximum in the log-likelihood curves of the total-cross section is less pronounced, which is simply due to the minimum expected number of events having increased.

6.2.3 THE MEASUREMENT USING THE INCLUSIVE CROSS-SECTION

Fully incorporating all accepted processes, as described in §5.4 of chapter 5, gives the log-likelihood curves shown in figures 6.5 and 6.6. Now the log-likelihood curves from the angular distribution fit have changed; the shape is roughly the same for all parameters, but for those parameters which have a local maximum in their curves— α_W & $\alpha_{B\phi}$ —the height of the maximum has decreased, and for the others, where the curve is roughly parabolic, the width of the curves has increased slightly. This indicates that neglecting the additional accepted processes would lead to an underestimated statistical error, and possibly a biased measurement.

SIMULTANEOUS FITS TO THE λ - Δg_Z^1 - $\Delta\kappa_\gamma$ PARAMETERS

Figure 6.7 shows the 95% C.L.L. contours for the λ - Δg_Z^1 - $\Delta\kappa_\gamma$ parameter set as measured from the 1998 data set using the multi-parameter negative extended log likelihood fit. The fitted values are indicated on the plots.

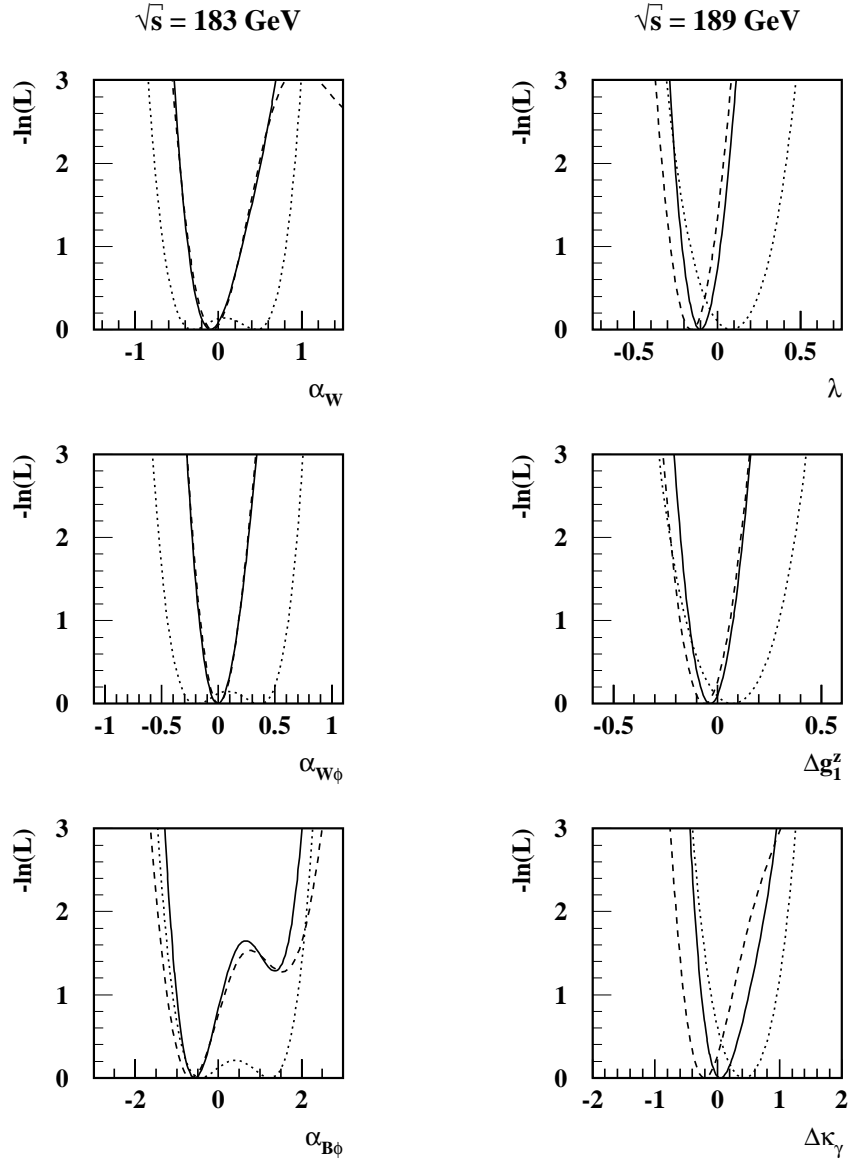


FIGURE 6.3: Log-likelihood curves for the main *T.G.C.* parameters measured using the basic *N.N.M.L.* fit incorporating the expected total cross-section.

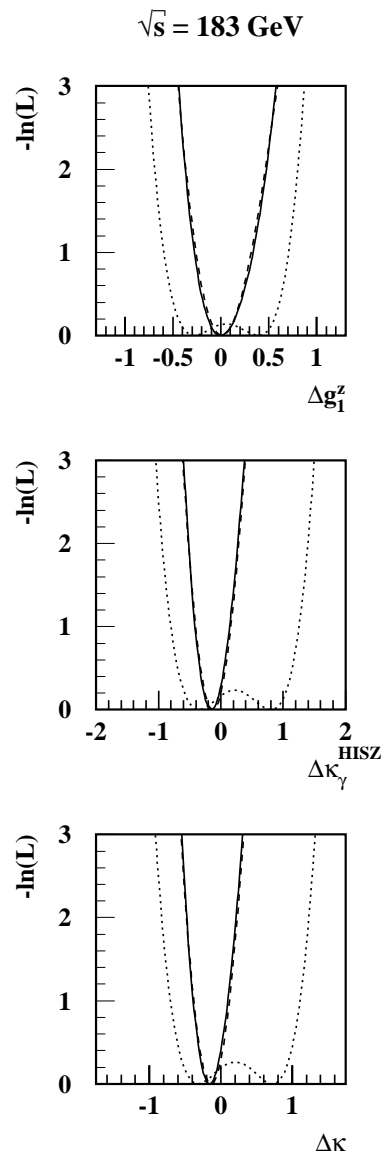


FIGURE 6.4: Log-likelihood curves for the additional T.G.C. parameters measured using the basic N.N.M.L. fit incorporating the expected total cross-section.

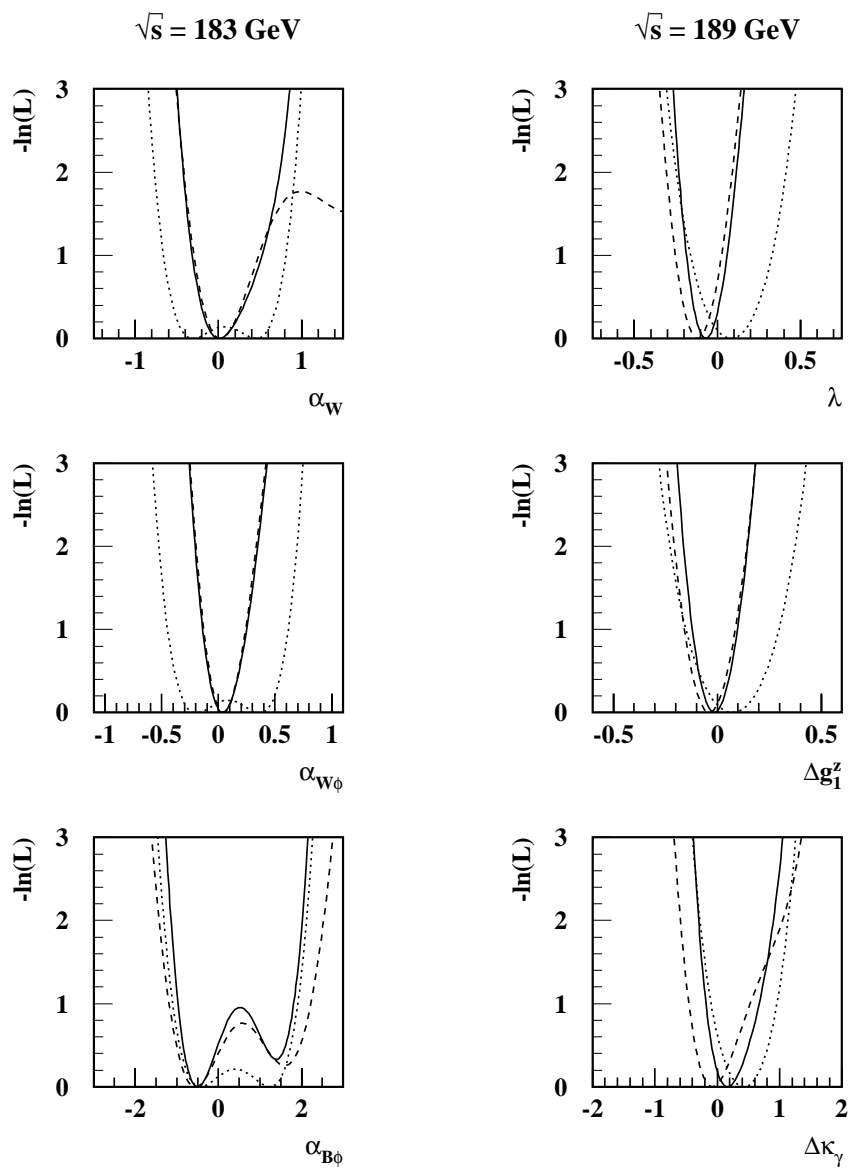


FIGURE 6.5: Log-likelihood curves for the main T.G.C. parameters measured using the inclusive cross-section N.N.M.L..

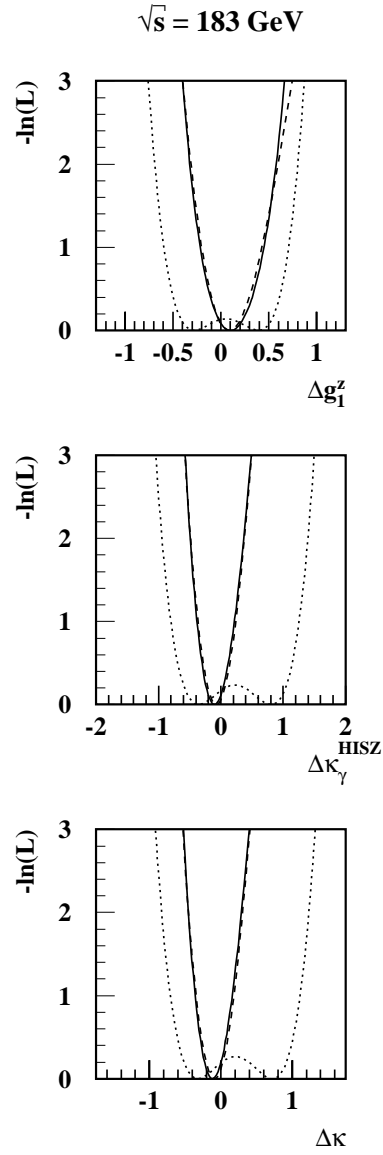


FIGURE 6.6: *Log-likelihood curves for additional T.G.C. parameters measured using the inclusive cross-section N.N.M.L..*

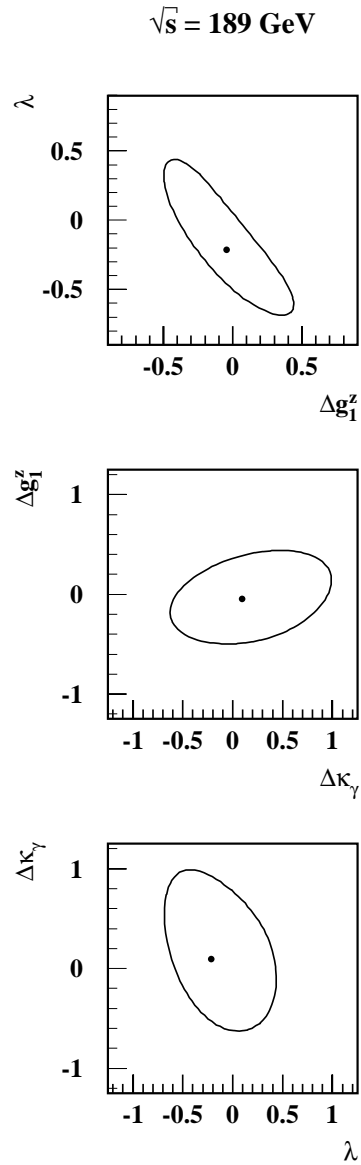


FIGURE 6.7: 95% C.L.L. contours for the λ - Δg_1^z - $\Delta \kappa_\gamma$ parameters measured from the 1998 data using the multi-parameter inclusive N.N.M.L..

6.2.4 INCORPORATING THE SYSTEMATIC ERROR

The systematic errors are incorporated in the fit as described in chapter 5, §5.6; the evaluation of the systematic errors are described in the following chapter. The resultant log-likelihood curves are shown in figures 6.8 and 6.9. The positions of the minima for these curves are taken as the final measured values of the T.G.C. parameters, quoted at the beginning of this chapter. The inclusion of the systematic uncertainty in the total cross-section has no noticeable effect, as it is so much smaller than the Poisson standard deviation on the number of events in the data sample; the effect of including that for the angular distribution fit is noticeable, and tends to soften the shape of the curves, as would be expected.

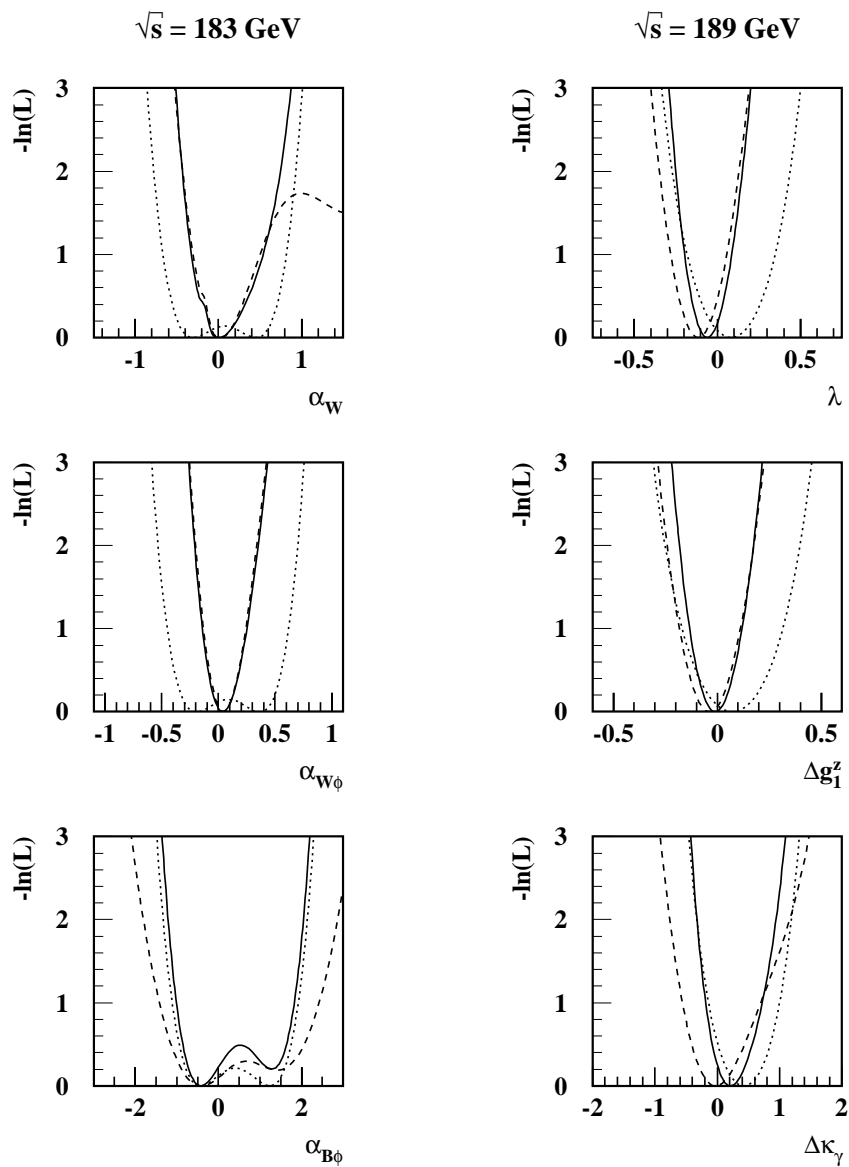


FIGURE 6.8: Log-likelihoods curves for the main T.G.C. parameters measured using the inclusive N.N.M.L. incorporating the expected systematic error.

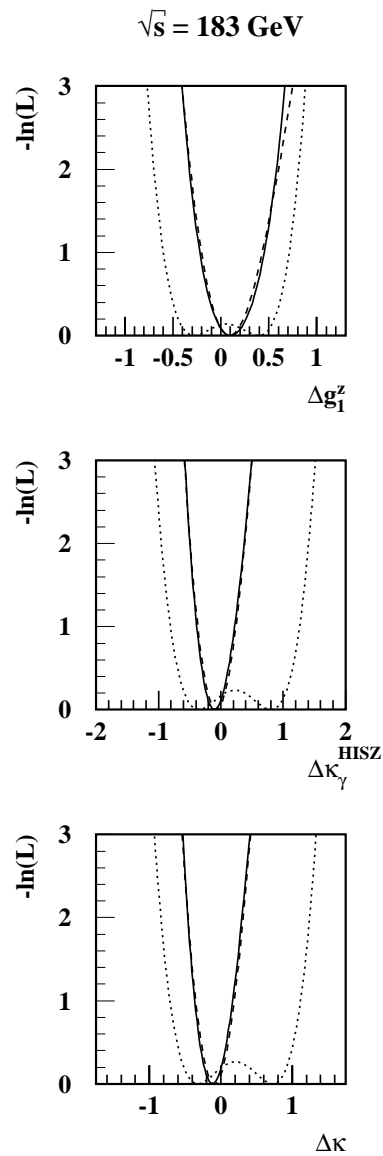


FIGURE 6.9: Log-likelihoods curves for additional T.G.C. parameters measured using the inclusive N.N.M.L. incorporating the expected systematic error.

6.3 MEASURED LIMIT ON THE SCALE OF NEW PHYSICS

A measured anomalous coupling implies the existence of some new physics process, as described by the relations given in §2.1.2. Using these relations, the measured values of the T.G.C. parameters give a range of values on the Upper Limit on the Scale of New Physics of 1–4TeV. However, these Upper Limits would only be significant if the Standard Model parameter values had been excluded; within the 1 sigma variation of the measured T.G.C. parameter values, no limit on Λ_{NP} may be imposed.

CHAPTER 7

EVALUATION OF THE SYSTEMATIC ERROR

The final results given in the previous chapter included the total systematic error without any reference to their source or evaluation. This chapter describes the evaluation of that systematic error. As the analyses are almost identical at the two different energies, there are only minor differences in the sources of systematic error. The sources of error which affect the event rate are detailed in section §7.1 and those which affect the distributions in §7.2.

7.1 SYSTEMATIC ERROR ON THE TOTAL CROSS-SECTION

There are several sources of uncertainty in the expected accepted cross-section. The uncertainties in the total cross-section are given in table 7.1, and the different contributions are described in the following sections. The resulting change in the fitted T.G.C. values (denoted as “ $\Delta\alpha$ ”) due to the inclusion of the rate systematics alone are given as the last entries in the table for information; they are not used directly in the analysis. The systematic errors due to the uncertainty in the total cross-section turn out to be negligible in comparison with those due to uncertainties in the angular distributions.

\sqrt{s} (in GeV)	T.G.C. Parameter	Uncertainty (in pb)				ΔN_{DATA}	$\Delta\alpha$	
		Electroweak Modelling	Acceptance	M_W & E_{BEAM}	Detector Simulation			Total
183GeV	α_W	0.020	0.018	0.003	0.021	0.034	2.0	0.0001
	$\alpha_W \phi$		0.019	0.003		0.035	2.0	0.0000
	$\alpha_{B\phi}$		0.018	0.009		0.035	2.0	-0.0008
	Δg_Z^1		0.019	0.003		0.035	2.0	0.0000
	$\Delta \kappa_\gamma^{\text{HSZ}}$		0.018	0.003		0.034	2.0	0.0002
	$\Delta \kappa$		0.018	0.003		0.034	2.0	0.0001
	λ		0.003	0.0094		0.019	0.059	11.1
Δg_Z^1	0.003	0.0093	0.059	11.1	-0.003			
$\Delta \kappa_\gamma$	0.004	0.0092	0.059	11.1	-0.026			
189GeV		0.055						

TABLE 7.1: The contributions to the systematic error on the total cross-section analysis. The evaluation of the different sources of uncertainty are described in the following sections. ΔN_{DATA} is the corresponding error in the accepted number of events, and $\Delta\alpha$ is the resulting change in the fitted T.G.C. parameters.

7.1.1 ELECTROWEAK MODELLING

The main reference four-fermion samples used in the analysis were generated using the EXCALIBUR generator, but other Monte Carlo generators predict a slightly different accepted cross-section. The only other four-fermion generator used to produce fully simulated data samples—and, hence, suitable for comparison—is `grc4f`. The breakdown of the total four-fermion cross-sections for the EXCALIBUR and `grc4f` generators are given in table 7.2, as are the difference between their predicted cross-sections and the resulting uncertainty in the predicted number of accepted events. There are no fully simulated `grc4f` samples generated with anomalous T.G.C. parameters so the systematic errors are evaluated at the Standard Model values.

\sqrt{s} (in GeV)	Cross-Section (in pb)								Uncertainty (in pb)
	EXCALIBUR				grc4f				
	Main 4-fermion	T.G.C.-dependent 4-fermion	T.G.C.-independent 4-fermion	Total	$\bar{l}l'\bar{l}' & l-\bar{\nu}_l l'+\nu_l$	$q\bar{q}l\bar{l} & q\bar{q}'l\nu_l$	$q\bar{q}q'\bar{q}' & q'l\bar{q}''q'''\bar{q}''''$	Total	
183 GeV	4.072	-	-	4.072	0.0014	4.041	0.0092	4.051	0.020
189 GeV	-	4.247	0.020	4.267	0.0014	4.205	0.0062	4.212	0.055

TABLE 7.2: The difference between expected accepted cross-section for the main four-fermion processes (excluding final states with e^\pm pairs) generated with the EXCALIBUR and that generated with the grc4f Monte Carlo Generators.

7.1.2 SELECTION ALGORITHM ACCEPTANCE

The expected accepted cross-section is calculated from Monte Carlo samples, and, therefore, has an associated error due to the finite statistics; this is effectively an uncertainty in the acceptance of the selection algorithm. This error has two main contributions: from the main 4-fermion reference samples, and from the samples for the other accepted processes. The errors from these sources are added in quadrature, and they are given in table 7.3.

MAIN REFERENCE SAMPLES

The total expected cross-section for the main reference samples is calculated as a function of the T.G.C. parameters from the Monte Carlo reference samples. The total number of accepted events in any given reference sample has an associated error, which, for simplicity, is taken as the Poisson standard deviation. Three parameters describe a cross-section parabola and so the error on the total cross-section is evaluated from these cross-section parameters and their covariance matrix, which themselves are found using the MINUIT package. For each T.G.C. parameter, the error is calculated at its fitted value.

REFERENCE SAMPLES FOR ADDITIONAL ACCEPTED PROCESSES

The additional reference samples, which are independent of the T.G.C. parameters, also have an associated error. Again, this is taken as the Poisson standard deviation on the total number of accepted events for each sample.

\sqrt{s} (in GeV)	T.G.C. Parameter	Process								Total
		Main 4-fermion	$Z^0/\gamma \rightarrow \bar{b}b$	2-photon	$e^-e^+q\bar{q}$	$e^-e^+\tau^-\tau^+$	$e^-e^+f\bar{f}$ (s-channel)	$e^-e^+f\bar{f}$ (t-channel)	Other 4-fermion	
183GeV	α_W	0.017								0.018
	$\alpha_{W\phi}$	0.018								0.019
	$\alpha_{B\phi}$	0.017	0.0034	0.004	0.0031	0.0002	-	-	-	0.018
	Δg_Z^1	0.017								0.019
	$\Delta \kappa_\gamma^{\text{HISZ}}$	0.017								0.018
	$\Delta \kappa$	0.017								0.018
	λ	0.0085								0.010
	Δg_Z^1	0.0084	0.0029	0.004	-	-	0.0006	0.002	0.0009	0.010
	$\Delta \kappa_\gamma$	0.0080								0.010
	189GeV									

TABLE 7.3: Systematic error due to statistical fluctuations in the Monte Carlo Reference Samples.

7.1.3 THE DEPENDENCE OF THE CROSS-SECTION ON KINEMATIC PARAMETERS

The cross-section for W-pair production depends on many input parameters, apart from the T.G.C. strengths. Most of these are very well-measured, and do not lead to an appreciable uncertainty in the expected cross-section, but both the W boson mass and the collision energy will do so. The resultant uncertainty is evaluated by direct evaluation of the $W^+W^- \rightarrow q\bar{q}l\nu_l$ cross-section using the Gentle cross-section calculator with different input parameters, corresponding to the uncertainties on these quantities. The errors are calculated at the fitted values of each of the T.G.C. parameters.

The full 4-fermion cross-section could be calculated using the EXCALIBUR Monte Carlo generator, but this would not be appropriate unless acceptance cuts could be applied; when only considering the CC3 cross-section this should be less important.

The errors due to the uncertainty on the mass of the W-boson and the beam energy are given in table 7.4.

THE MASS OF THE W^\pm BOSON

The EXCALIBUR Monte Carlo reference samples were generated using a W boson mass of 80.33GeV, but the current measured value from Fermilab is $80.45 \pm 0.06\text{GeV}$ [65]. It is possible to evaluate a systematic shift due to this effect rather than a symmetric error, but the best method to do this is somewhat ambiguous because the extent of the change in the cross-section is dependent on the T.G.C. strength; fortunately, the error due to this uncertainty is small, and any bias in the fitted T.G.C. value is absolutely negligible compared with their errors.

BEAM ENERGY

The Monte Carlo reference samples were generated with the nominal beam energies of 183GeV and 189GeV. The actual beam energy is not constant across a single run, and also has an associated error. The average beam energy is

$$E_{\text{BEAM}} = 91.480 \pm 0.167 \pm 0.025 \text{GeV}$$

for the 1997 run[66, 67], and

$$E_{\text{BEAM}} = 94.348 \pm 0.144 \pm 0.020 \text{GeV}$$

for the 1998 run[68, 69]. The first error is the standard deviation of the beam energies for the runs and the second is the error on the measurement of the beam energy; only the latter is taken as a systematic uncertainty.

\sqrt{s} (in GeV)	T.G.C.	Uncertainty (in pb)		
	Parameter	M_W	E_{BEAM}	Total
183GeV	α_W	0.0024	0.0012	0.003
	$\alpha_{W\phi}$	0.0025	0.0012	0.003
	$\alpha_{B\phi}$	0.0084	0.0014	0.009
	Δg_Z^1	0.0031	0.0012	0.003
	$\Delta \kappa_\gamma^{\text{HISZ}}$	0.0029	0.0013	0.003
	$\Delta \kappa$	0.0030	0.0013	0.003
189GeV	λ	0.0027	0.0006	0.003
	Δg_Z^1	0.0030	0.0006	0.003
	$\Delta \kappa_\gamma$	0.0039	0.0006	0.004

TABLE 7.4: *Uncertainties in the $W^+W^- \rightarrow q\bar{q}'l\nu_l$ cross-section due to the mass of the W^\pm boson and the beam energy.*

7.1.4 DETECTOR SIMULATION

There is an error in the measured cross-section which is due to the acceptance uncertainty from the imperfect simulation of the OPAL detector[70, 71]. Firstly, there are known to be tracking losses in the OPAL detector which are not simulated by the GOPAL package. Secondly, there is a discrepancy between the acceptance of faked $W^+W^- \rightarrow q\bar{q}l\nu_l$ events from real data and Monte Carlo events; the faked events are constructed by combining real LEP-I multihadronic events and hemispheres from lepton pair events. The WW package selection function is tested on the faked and Monte Carlo events and the difference between the measured acceptance is assigned as the systematic error. The errors are shown in table 7.5.

\sqrt{s} (in GeV)	Uncertainty (in pb)		
	Tracking Losses	Data/MC Discrepancy	Total
183GeV	0.0123	0.0170	0.0210
183GeV	0.0099	0.0163	0.0191

TABLE 7.5: *Uncertainty in the measured cross-section due to the imperfect detector simulation.*

7.2 UNCERTAINTIES IN THE DECAY DISTRIBUTIONS

The effect of the uncertainties in the decay angle distributions of the final state fermions has a much larger effect than the uncertainty in the total cross-section. The total systematic errors on the fitted T.G.C. parameters from the analysis are given in table 7.6, and the evaluation of the different contributions are explained in the subsequent sections.

7.2.1 FINITE MONTE CARLO STATISTICS

The analysis method, obviously, is heavily dependent on the size of the reference files. The statistics directly effect the fitted paraboli, used to find the probability density functions, but this error does not propagate through to the final error on the fitted value. Hence, an estimation of the contribution to the error from the limited statistics of the reference samples must be included in the total error.

If the analysis of a particular parameter were repeated an arbitrary number of times, but with different reference samples, there will be a finite standard deviation on the distribution of the fitted results; it is assumed that this standard deviation will vary in inverse proportion to the root of the size of the reference samples.

Obviously, extra sets of reference samples do not exist and so this spread in the fitted value cannot be directly measured. However, it may be inferred by splitting the existing reference samples into smaller subsamples, and repeating the analysis with these subsamples. From the standard deviation found using these smaller samples, the standard deviation for the full samples may be inferred.

Each of the reference samples are split into four subsamples, so that each of

\sqrt{s} (in GeV)	T.G.C. Parameter	Fitted Value	Systematic Error						Total
			Finite Statistics	Background Level	Electroweak Modelling	Detector Simulation	Jet Recon- struction		
183GeV	α_W	$0.012^{+0.343}_{-0.240}$	0.012	0.012	0.053	0.005	0.0103	0.0565	
	$\alpha_{W\phi}$	$0.039^{+0.144}_{-0.128}$	0.0048	0.0065	0.017	0.003	0.0099	0.0218	
	$\alpha_{B\phi}$	$-0.423^{+0.493}_{-0.345}$	0.037	0.0064	0.467	0.020	0.0432	0.471	
	Δg_Z^1	$0.101^{+0.252}_{-0.233}$	0.015	0.012	0.023	0.003	0.0131	0.0322	
	$\Delta \kappa_\gamma^{\text{HISZ}}$	$-0.102^{+0.220}_{-0.201}$	0.0030	0.0067	0.028	0.011	0.0136	0.0342	
	$\Delta \kappa$	$-0.117^{+0.191}_{-0.175}$	0.014	0.0064	0.032	0.003	0.0128	0.0379	
189GeV	λ	$-0.059^{+0.086}_{-0.081}$	0.0041	0.0022	0.059	0.027	0.0152	0.0669	
	Δg_Z^1	$-0.010^{+0.076}_{-0.073}$	0.0072	0.0036	0.051	0.013	0.0161	0.0569	
	$\Delta \kappa_\gamma$	$0.211^{+0.314}_{-0.251}$	0.029	0.025	0.203	0.093	0.0377	0.235	

TABLE 7.6: The systematic error on the fitted T.G.C. values. The evaluation of the individual contributions are described in the following sections.

the subsamples from a single reference sample are of equal size. The analysis is repeated for each set of subsamples, and the standard deviations are calculated. The true standard deviation, σ_{MCSTATS} , is then assumed to be given by

$$\sigma_{\text{MCSTATS}} = \frac{\sigma_{\text{SUBSAMPLE}}}{\sqrt{4}}.$$

Where $\sigma_{\text{SUBSAMPLE}}$ is the standard deviation of the fitted results from the four sets of subsamples. By splitting each of the main samples into equal sized subsamples, the difference in absolute size of the samples becomes irrelevant.

This method is not watertight; for one thing, four subsamples will only give a relatively poor measure of the standard deviation. Secondly, the analysis parameters (r_0 and $N_{RP/DP}$) are not optimized for these smaller samples. This should not matter too much, as only their relative spread—not the central values themselves—are important. The uncertainties as measured using this method are given in table 7.7.

\sqrt{s} (in GeV)	T.G.C. Parameter	Error
183 GeV	α_W	0.012
	$\alpha_{W\phi}$	0.0048
	$\alpha_{B\phi}$	0.037
	Δg_Z^1	0.015
	$\Delta \kappa_\gamma^{\text{HISZ}}$	0.0030
	$\Delta \kappa$	0.014
189 GeV	λ	0.0041
	Δg_Z^1	0.0072
	$\Delta \kappa_\gamma$	0.029

TABLE 7.7: Estimation of the error due to the finite statistics of the Monte Carlo Reference Samples.

7.2.2 THE BACKGROUND ESTIMATION

Each of the samples used in the background estimation are considerably smaller than those used as the main reference samples; this makes the relative error due to statistical fluctuations comparatively large. In order to estimate the resulting error, shown in table 7.8, the overall background cross-sections are, in turn, increased and decreased by a factor corresponding to the Poisson standard deviation. The fits to the data samples are performed using these modified background samples, and the largest deviation from the central value is taken as the systematic error.

In addition to this, the two-photon background is known to be somewhat poorly modelled (as mentioned in section §4.1.2) and so, in addition to the previous evaluation, this background is doubled and removed in the fit; again, the largest deviation is taken as the error.

\sqrt{s} (in GeV)	T.G.C. Parameter	Uncertainty		
		All background	2-photon	Total
183GeV	α_W	0.010	0.0050	0.012
	$\alpha_{W\phi}$	0.0053	0.0038	0.0065
	$\alpha_{B\phi}$	0.0035	0.0054	0.0064
	Δg_Z^1	0.0071	0.0091	0.012
	$\Delta \kappa_\gamma^{\text{HISZ}}$	0.0057	0.0035	0.0067
	$\Delta \kappa$	0.0052	0.0037	0.0064
189GeV	λ	0.0021	0.0008	0.0022
	Δg_Z^1	0.0031	0.0018	0.0036
	$\Delta \kappa_\gamma$	0.014	0.020	0.025

TABLE 7.8: *Uncertainty in the fitted values of the T.G.C. parameters due to the statistical error of the non-T.G.C. dependent Monte Carlo reference samples.*

7.2.3 MONTE CARLO MODELLING

All the T.G.C.-dependent samples used in the analysis were generated with the EXCALIBUR Monte Carlo generator. No Monte Carlo generator could give a perfect simulation of the data events collected by OPAL, and there are a number of uncertainties which may effect the reference samples.

Most obviously, there is an uncertainty in how well the generator describes the fundamental interactions. In order to obtain a measure of the uncertainty in the modelling of the physical interaction by this generator, fits to Standard Model EXCALIBUR test samples are compared to fits to Standard Model grc4f test samples. The systematic error is taken as the difference between the two fit results.

In addition to this, the way that the quarks fragment into jets of particles is not very well understood. Dedicated programs simulate the fragmentation of a quark into a jet, and of these JETSET is the most commonly used. In order to see the effect that the uncertainty in the fragmentation model may have, fits are compared to two samples which have identical events at the generator level but have had the quarks hadronized by JETSET and by HERWIG [72]. Again, the error is taken as the difference between these fitted results.

The errors from these two sources are shown in table 7.9.

7.2.4 DETECTOR SIMULATION

The imperfect modelling of the detector affects the acceptance efficiency of the detector as a function of the detector polar angle. This has the largest effect on the electron candidate in $W^+W^- \rightarrow q\bar{q}'e\nu_e$ events. The most problematic region for the electrons is in the overlap of the Electromagnetic Barrel and Endcap Calorimeters, the ‘‘Transition Region’’; this lies between $0.72 < |\cos \theta_{\text{DET}}| < 0.82$. Additionally, there are discrepancies in the 1998 run between the Monte Carlo and Data acceptance of electrons in the forward calorimeter, where $0.90 < |\cos \theta_{\text{DET}}| < 0.95$. For simplicity, the errors due

\sqrt{s} (in GeV)	T.G.C. Parameter	Uncertainty		
		Electroweak Modelling	Fragmentation Modelling	Total
183GeV	α_W	0.045	0.028	0.053
	$\alpha_{W\phi}$	0.014	0.011	0.017
	$\alpha_{B\phi}$	0.401	0.239	0.467
	Δg_Z^1	0.010	0.020	0.023
	$\Delta \kappa_\gamma^{\text{HISZ}}$	0.019	0.022	0.028
	$\Delta \kappa$	0.0078	0.031	0.032
189GeV	λ	0.058	0.011	0.059
	Δg_Z^1	0.050	0.011	0.051
	$\Delta \kappa_\gamma$	0.118	0.164	0.203

TABLE 7.9: *Uncertainty in the fitted T.G.C. parameters due to Monte Carlo modelling.*

to these acceptance uncertainties are evaluated by performing the T.G.C. fits on reduced data samples which have these events removed; for the 1998 data samples two reduced data samples are formed, one with the Transition Region events removed, and the other with the Forward Detector events removed. The error is taken as the difference between the fitted values from these samples and the full event samples. The errors are given in table 7.10

\sqrt{s} (in GeV)	T.G.C. Parameter	Uncertainty		
		Electromagnetic Calorimeter	Forward Detector	Total
183 GeV	α_W	0.005	-	0.005
	$\alpha_{W\phi}$	0.003	-	0.003
	$\alpha_{B\phi}$	0.020	-	0.020
	Δg_Z^1	0.003	-	0.003
	$\Delta \kappa_\gamma^{\text{HISZ}}$	0.011	-	0.011
	$\Delta \kappa$	0.003	-	0.003
189 GeV	λ	0.020	0.018	0.027
	Δg_Z^1	0.010	0.008	0.013
	$\Delta \kappa_\gamma$	0.083	0.042	0.093

TABLE 7.10: *Uncertainties in the fitted T.G.C. parameters due to the imperfect detector simulation.*

7.2.5 JET RECONSTRUCTION

In addition to the uncertainty in the modelling of the jet fragmentation, there is also an uncertainty in their reconstruction. This is evaluated[73] by studying antiparallel jets at LEP1 and comparing the collected data with the Monte Carlo events. This yields uncertainties of 10% for the jet energy resolution, 0.5% for the overall jet energy, 10% for the resolution of the jet angles in the lab-frame, $\cos\theta_{\text{JET}}$ and ϕ_{JET} , and ~ 0.01 for the absolute error on $\cos\theta_{\text{JET}}$. In order to quantify the systematic error due to these uncertainties, a large Standard Model EXCALIBUR test sample is modified as follows to give six new samples:

- E_{JET} smeared by 10%
- E_{JET} scaled by 0.5%
- $\cos\theta_{\text{JET}}$ smeared by 10%
- $\cos\theta_{\text{JET}}$ shifted by 0.010
- $|\cos\theta_{\text{JET}}|$ shifted by 0.009
- ϕ_{JET} smeared by 10%

Each of these six samples and the original, unaltered sample were fit to the T.G.C. parameters; the total systematic error is taken as the shifts in the fitted results added in quadrature. The errors are given in table 7.11.

The measured direction of the hadronic system is very important in this analysis, as it gives the W boson decay angle ($\cos\theta_{\text{W}}$). The resolution on $\cos\theta_{\text{W}}$ may be inferred directly by studying radiative fermion-pair production events. By selecting events with an identified initial state photon a sample of jet pairs with similar acolinearities to those in W-pair production events is obtained. As it is known that the hadronic system and the photon must be antiparallel, the resolution on the measured direction of the hadronic system may be taken as their acolinearity. Such studies yield a very conservative

\sqrt{s} (in GeV)	T.G.C. Parameter	Uncertainty							Total
		E_{JET} Smeared	E_{JET} Scaled	$\cos \theta_{\text{JET}}$ Smeared	$\cos \theta_{\text{JET}}$ Shifted	$ \cos \theta_{\text{JET}} $ Shifted	ϕ_{JET} Smeared		
183GeV	α_{W}	0.0002	0.0016	0.0042	0.0041	0.0068	0.0048	0.0103	
	$\alpha_{\text{W}\phi}$	0.0005	0.0026	0.0024	0.0038	0.0079	0.0029	0.0099	
	$\alpha_{\text{B}\phi}$	0.0043	0.0067	0.032	0.012	0.015	0.020	0.0432	
	Δg_{Z}^1	0.0012	0.0051	0.0001	0.0078	0.0072	0.0056	0.0131	
	$\Delta \kappa_{\gamma}^{\text{HSZ}}$	0.0025	0.0051	0.0027	0.0019	0.0112	0.0040	0.0136	
	$\Delta \kappa$	0.0012	0.0016	0.0035	0.0044	0.0099	0.0055	0.0128	
	λ	0.0035	0.0023	0.0012	0.0015	0.0145	0.0003	0.0152	
	Δg_{Z}^1	0.0030	0.0014	0.0009	0.0008	0.0157	0.0010	0.0161	
	$\Delta \kappa_{\gamma}$	0.0093	0.0040	0.0012	0.0017	0.0362	0.0008	0.0377	
	189GeV								

TABLE 7.11: *Uncertainties in the fitted T.G.C. parameters due to the uncertainty in the measured energy and direction of the jets.*

error on the W boson decay angle of 0.01, which is in good agreement with the suggested error on the individual jets, given above, and so no additional systematic error need be assigned.

CHAPTER 8

CONCLUSION

In this thesis a new analysis method—the Near Neighbour Maximum Likelihood—was used to measure the Triple Gauge Couplings from data collected by the OPAL detector at collision energies of 183GeV and 189GeV. To conclude this thesis, the performance and possible improvements of the N.N.M.L. are reviewed, and finally the implications of the measured results and their consistency with the published measurements from the OPAL experiment are discussed.

8.1 REVIEW OF THE N.N.M.L. METHOD

8.1.1 POSSIBLE MODIFICATIONS OF THE METHOD

The Near Neighbour method for measuring a differential cross-section or probability density from a set of discrete points has been shown to be a viable method by the tests of the analysis, described in chapter 5. However, there are many modifications which could be made, both for use in T.G.C. studies, or else for application in other analyses.

For the general Near Neighbour weighting method:

- The length scale, r_0 , need not be the same for each variable in the phase space, so that the weighting function would have a hyper-

ellipsoidal symmetry, rather than hyper-spheroidal as it does as used in the analysis presented in this thesis. This would allow the relative sensitivities of the different variables to be utilised.

- Alternative kernels could be investigated, although it is unlikely that a dramatic improvement would result.

For T.G.C. analyses in particular:

- For any given data event the length scale, r_0 , could be allowed to vary for different reference samples. When using the tophat kernel this would be akin to measuring the volume which contains a given number of reference events, rather than measuring the number of data events within a specified volume. Developing this method for other kernels would be harder, particularly if the error on the measured differential cross-section is to be used.
- An increased phase space may be used, including, for example, the decay angles of the hadronic system.
- The method could easily be applied to the other decay channels. If it were, it might be useful to investigate the use of other variables other than the traditional angular variables, because of the ambiguities in their reconstruction in the $W^+W^- \rightarrow l\nu_l l'\nu_{l'}$ and $W^+W^- \rightarrow q'\bar{q}''q'''\bar{q}''''$ channels.
- For the multi-parameter fits, more effort should be devoted to recovering those events which give non-physical cross-section functions. A procedure based around the MINUIT package would probably be most succesful for this, although additional reference samples would probably also be useful.

Of these possible modifications, the variable-dependent r_0 might be the most useful extension of the general method.

8.1.2 THE PERFORMANCE OF THE N.N.M.L.

The analysis appears to work least well for the $\alpha_{B\phi}$ and $\Delta\kappa_\gamma$ parameters; this is seen both in the tests of the analysis (chapter 5) and also in the errors on the measurement of the data (chapters 6 & 7). The reason for this is almost certainly that the cross-section is much less sensitive to anomalous values of these parameters than of the others.

The large statistical error on these parameters is to be expected, as the measurement of a weaker parameter will always have a larger statistical error. However, the systematic error on the fitted values of these two parameters is much more significant than it is for any of the other parameters measured. Again, this is probably due to the statistical fluctuations within the test sample and reference samples having a much larger effect than with the more sensitive parameters. If this is the case, a better measure of these two parameters might be achieved if the reference samples were generated with a larger range of coupling strengths (so that samples with coupling strengths of, say, $-4, -2, -1, 0, 1, 2, 4$ were used in the fit rather than samples with strengths of $-2, -1, -\frac{1}{2}, 0, \frac{1}{2}, 1, 2$). This should not degrade the statistical error, and might reduce the systematic error. If the N.N.M.L. method were to be more fully investigated—as opposed to being developed expressly to be used in an analysis, as in this thesis—it might be useful to compare, for example, fits using the three samples generated with Δg_Z^1 equal to $-\frac{1}{2}, 0$ and $+\frac{1}{2}$ to fits with the samples generated with $\Delta\kappa_\gamma$ equal to $-2, 0$ and $+2$; this would give some indication whether the comparatively poorer measurement of the $\alpha_{B\phi}$ & $\Delta\kappa_\gamma$ parameters was simply due to the weaker cross-sectional dependence.

8.1.3 COMPARISON WITH OTHER METHODS

The N.N.M.L. analysis was included in the OPAL analysis of the 1998 data set[74] as a consistency check of the main analysis which is based on an “Optimal Observables” method; to be consistent with the other analyses in

the paper, events selected as $W^+W^- \rightarrow q\bar{q}'\tau\nu_\tau$ had to be included in the data sample and Monte Carlo reference samples. Figure 8.1 shows the likelihood curve from the Optimal Observables (O.O.) method, the Binned Maximum Likelihood (B.M.L.) method (both performed by other members of the OPAL T.G.C. group) and the N.N.M.L. method; as can be seen, the N.N.M.L. is in good agreement with the other methods although the error is slightly bigger.

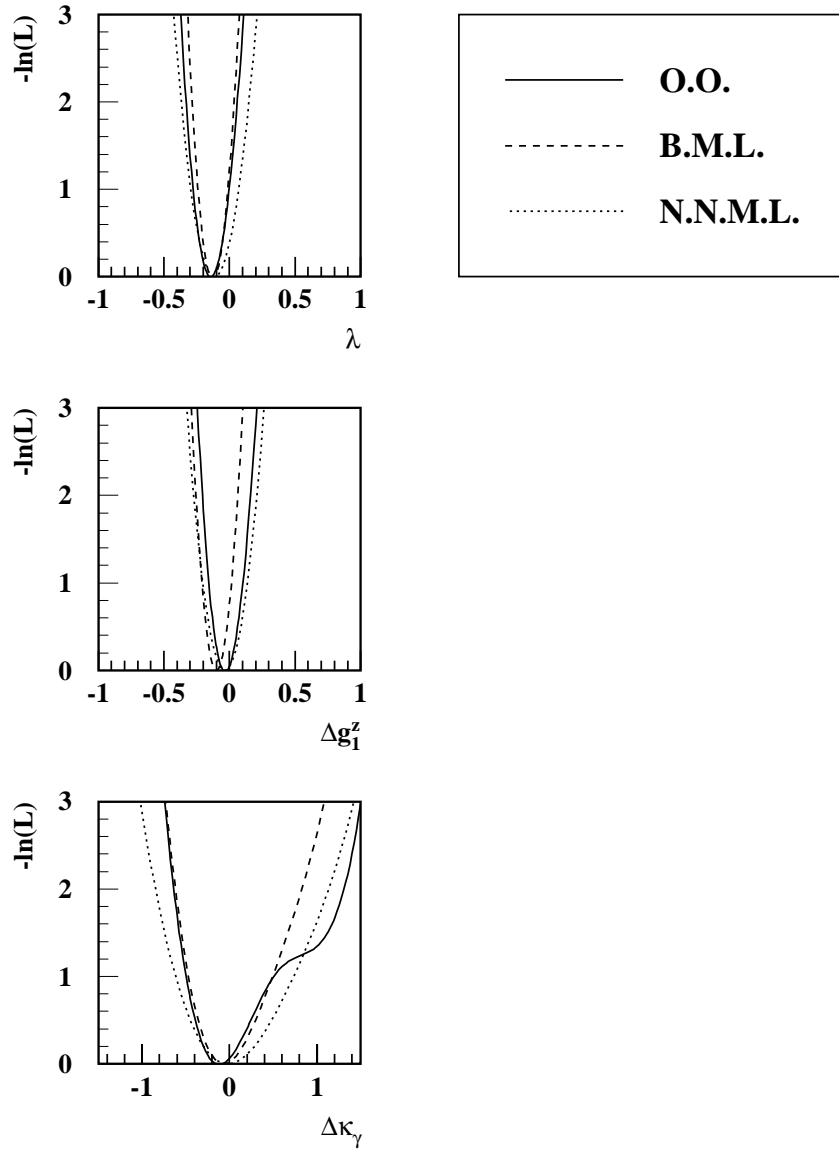


FIGURE 8.1: Likelihood curves for the λ - Δg_Z^1 - $\Delta \kappa_\gamma$ parameter set obtained using three different analyses on the 1998 data set of events selected as $W^+W^- \rightarrow q\bar{q}'e\nu_e$ or $W^+W^- \rightarrow q\bar{q}'\mu\nu_\mu$ or $W^+W^- \rightarrow q\bar{q}'\tau\nu_\tau$, as published by the OPAL Collaboration[74].

8.2 DISCUSSION OF THE MEASUREMENTS

No anomalous coupling strengths between the electroweak gauge bosons were detected in the analysis of the 1997 and 1998 data sets of events selected as $W^+W^- \rightarrow q\bar{q}'e\nu_e$ or $W^+W^- \rightarrow q\bar{q}'\mu\nu_\mu$. Table 8.2 shows the published

\sqrt{s} (in GeV)	T.G.C. Parameter	N.N.M.L. Measurements	Published OPAL Measurements
183GeV	α_W	$0.012_{-0.240}^{+0.343} \pm 0.056$	$-0.14 \pm -0.15 \pm 0.04$
	$\alpha_{W\phi}$	$0.039_{-0.128}^{+0.144} \pm 0.022$	$-0.06_{-0.10}^{+0.12} \pm 0.11$
	$\alpha_{B\phi}$	$-0.423_{-0.345}^{+0.493} \pm 0.470$	$0.04_{-0.45}^{+0.61} \pm 0.18$
	Δg_Z^1	$0.101_{-0.233}^{+0.252} \pm 0.061$	$-0.01 \pm 0.14 \pm 0.043$
	$\Delta \kappa_\gamma^{\text{HISZ}}$	$-0.102_{-0.201}^{+0.220} \pm 0.054$	$-0.13_{-0.16}^{+0.18} \pm 0.17$
	$\Delta \kappa$	$-0.117_{-0.175}^{+0.191} \pm 0.210$	$-0.13_{-0.16}^{+0.17} \pm 0.17$
189GeV	λ	$-0.059_{-0.081}^{+0.086} \pm 0.061$	$-0.143_{-0.093}^{+0.097} \pm 0.036$
	Δg_Z^1	$-0.010_{-0.073}^{+0.076} \pm 0.054$	$-0.032_{-0.085}^{+0.091} \pm 0.038$
	$\Delta \kappa_\gamma$	$0.211_{-0.251}^{+0.314} \pm 0.210$	$-0.12_{-0.27}^{+0.36} \pm 0.143$

TABLE 8.1: *The measured T.G.C. parameter values from the OPAL experiment using events selected as $W^+W^- \rightarrow q\bar{q}'e\nu_e$ or $W^+W^- \rightarrow q\bar{q}'\mu\nu_\mu$ or $W^+W^- \rightarrow q\bar{q}'\tau\nu_\tau$, and those from the N.N.M.L. analysis using only those events selected as $W^+W^- \rightarrow q\bar{q}'e\nu_e$ or $W^+W^- \rightarrow q\bar{q}'\mu\nu_\mu$. The numbers in italics were obtained with a preliminary analysis[75] using a binned maximum likelihood analysis on an incomplete data set; the other results from OPAL[76, 74] were obtained using an Optimal Observable analysis.*

measurements of the T.G.C. parameters from the OPAL experiment obtained

using the O.O. or B.M.L. analyses on the 1997 and 1998 data sets of events selected as $W^+W^- \rightarrow q\bar{q}'e\nu_e$ or $W^+W^- \rightarrow q\bar{q}'\mu\nu_\mu$ or $W^+W^- \rightarrow q\bar{q}'\tau\nu_\tau$. Unlike the case for the likelihood curves shown in figure 8.1, the measured values and errors for each parameter shown in table 8.2 are not expected to be the same, as the data sample is different (some of the OPAL measurements were preliminary, and did not use the complete data set; these are indicated in the table). The measurements obtained using the N.N.M.L. are consistent with the OPAL measurements, although with larger errors.

In addition, table 8.2 gives the 95% C.L.L. from the analysis presented in this thesis, and also the combined limits from the OPAL experiment[74] and those from the DØ [77] experiment for the λ - Δg_Z^1 - $\Delta\kappa_\gamma$ parameter set.

Parameter	N.N.M.L. Limits	Published OPAL Limits	Published DØ Limits	Published CDF Limits
λ	-0.216, 0.116	-0.25, 0.04	-0.18, 0.19	-0.81, 0.84
Δg_Z^1	-0.150, 0.143	-0.14, 0.14	-0.67, 0.56	—
$\Delta\kappa_\gamma$	-0.247, 0.859	-0.36, 0.83	-0.18, 0.36	—

TABLE 8.2: 95% C.L.L. on the λ - Δg_Z^1 - $\Delta\kappa_\gamma$ parameters from the $\sqrt{s} = 189\text{GeV}$ N.N.M.L. analysis compared with the published limits from the OPAL[74] and DØ [77] experiments. Additionally, limits from the CDF experiment[10] are given for the λ parameter.

At the experimental precision reached to date, there is no evidence of anomalous trilinear couplings between the electroweak bosons. Naturally, this means that no limit can be imposed upon the Scale of New Physics.

APPENDIX A

MONTE CARLO SAMPLES

Tables A.1 & A.2 give the details of the Monte Carlo samples at $\sqrt{s} = 183\text{GeV}$ & $\sqrt{s} = 189\text{GeV}$ respectively used in the analysis presented in this thesis.

A.1 MONTE CARLO SAMPLES AT $\sqrt{s} = 183\text{GeV}$

Simulated Process	Generator	Run Number	$\frac{N_{\text{ACCEPTED}}}{N_{\text{SAMPLE}}}$	Luminosity (in fb^{-1})
4-fermion ^a Standard Model	EXCALIBUR	7330	$\frac{21299}{100000}$	5231
4-fermion $\alpha_W = -2$	EXCALIBUR	7334	$\frac{11526}{50000}$	1376
4-fermion $\alpha_W = -1$	EXCALIBUR	7832	$\frac{11224}{50000}$	2114

^aThroughout this table samples labelled “4-fermion” contain no e^+e^- pairs.

TABLE A.1: *Monte Carlo Reference samples at $\sqrt{s} = 183\text{GeV}$. N_{ACCEPTED} is the number of events accepted by the Selection algorithm—described in Chapter 4—and N_{SAMPLE} is the number of events processed.*

Table A.1 continued ...

Simulated Process	Generator	Run Number	$\frac{N_{\text{ACCEPTED}}}{N_{\text{SAMPLE}}}$	Luminosity (in fb^{-1})
4-fermion $\alpha_W = +1$	EXCALIBUR	7831	$\frac{10699}{49500}$	2177
4-fermion $\alpha_W = +2$	EXCALIBUR	7333	$\frac{11381}{50000}$	1447
4-fermion $\alpha_{W\phi} = -2$	EXCALIBUR	7332	$\frac{12012}{50000}$	962
4-fermion $\alpha_{W\phi} = -1$	EXCALIBUR	7828	$\frac{11704}{50000}$	1814
4-fermion $\alpha_{W\phi} = +1$	EXCALIBUR	7827	$\frac{10697}{50000}$	1878
4-fermion $\alpha_{W\phi} = +2$	EXCALIBUR	7331	$\frac{11347}{50000}$	1000
4-fermion $\alpha_{B\phi} = -2$	EXCALIBUR	7830	$\frac{10828}{48500}$	2367
4-fermion $\alpha_{B\phi} = -1$	EXCALIBUR	7336	$\frac{11341}{50000}$	2058
4-fermion $\alpha_{B\phi} = +1$	EXCALIBUR	7829	$\frac{9706}{47500}$	2342
4-fermion $\alpha_{B\phi} = +2$	EXCALIBUR	7335	$\frac{9804}{50000}$	2089
4-fermion $\Delta g_Z^1 = -2$	EXCALIBUR	7826	$\frac{11990}{50000}$	1250
4-fermion $\Delta g_Z^1 = -1$	EXCALIBUR	7825	$\frac{11146}{49500}$	2024
4-fermion $\Delta g_Z^1 = +1$	EXCALIBUR	7824	$\frac{11021}{50000}$	2090
4-fermion $\Delta g_Z^1 = +2$	EXCALIBUR	7823	$\frac{11378}{49500}$	1276

Table A.1 continued ...

Simulated Process	Generator	Run Number	$\frac{N_{\text{ACCEPTED}}}{N_{\text{SAMPLE}}}$	Luminosity (in fb^{-1})
4-fermion $\Delta\kappa_{\gamma}^{\text{HISZ}} = -2$	EXCALIBUR	7835	$\frac{11046}{50000}$	2278
4-fermion $\Delta\kappa_{\gamma}^{\text{HISZ}} = -1$	EXCALIBUR	7836	$\frac{11443}{50000}$	1682
4-fermion $\Delta\kappa_{\gamma}^{\text{HISZ}} = +1$	EXCALIBUR	7834	$\frac{10203}{50000}$	2342
4-fermion $\Delta\kappa_{\gamma}^{\text{HISZ}} = +2$	EXCALIBUR	7833	$\frac{10144}{50000}$	1753
4-fermion $\Delta\kappa = -2$	EXCALIBUR	7839	$\frac{11111}{50000}$	2213
4-fermion $\Delta\kappa = -1$	EXCALIBUR	7840	$\frac{11727}{50000}$	1549
4-fermion $\Delta\kappa = +1$	EXCALIBUR	7838	$\frac{10234}{50000}$	2293
4-fermion $\Delta\kappa = +2$	EXCALIBUR	7837	$\frac{10367}{50000}$	1627
$e^{-}e^{+}q\bar{q}$	grc4f	7055	$\frac{248}{133677}$	5000
$e^{-}e^{+}\tau^{-}\tau^{+}$	grc4f	7054	$\frac{1}{9378}$	5000
$Z^0/\gamma \rightarrow q\bar{q}$	PYTHIA	5050	$\frac{249}{396019}$	4654
Tagged Two-photon	HERWIG	1126	$\frac{5}{168177}$	501

Table A.1 continued ...

Simulated Process	Generator	Run Number	$\frac{N_{\text{ACCEPTED}}}{N_{\text{SAMPLE}}}$	Luminosity (in fb ⁻¹)
$l^-\bar{\nu}_l l'^+ \nu_{l'} & \bar{l} l' \bar{l}'$ Standard Model	grc4f	7349	$\frac{7}{15090}$	5000
$q\bar{q}' l \nu_l & q\bar{q} \bar{l}'$ Standard Model	grc4f	8056	$\frac{20206}{40566}$	5000
$q'\bar{q}'' q'''\bar{q}'''' & q\bar{q}q'\bar{q}'$ Standard Model	grc4f	7051	$\frac{46}{39312}$	5000
$e^-e^+ \rightarrow W^+W^-$ JETSET fragmentation	grc4f	8437	$\frac{19882}{77701}$	5000
$e^-e^+ \rightarrow W^+W^-$ HERWIG fragmentation	grc4f	8441	$\frac{19924}{77701}$	5000

A.2 MONTE CARLO SAMPLES AT $\sqrt{s} = 189\text{GeV}$

Simulated Process	Generator	Run Number	$\frac{N_{\text{ACCEPTED}}}{N_{\text{SAMPLE}}}$	Luminosity (in fb^{-1})
T.G.C.-dependent 4-fermion Standard Model	EXCALIBUR	8100	$\frac{107203}{460000}$	25260
T.G.C.-dependent 4-fermion $\lambda=-2$	EXCALIBUR	8262	$\frac{24326}{100000}$	2432
T.G.C.-dependent 4-fermion $\lambda=-1$	EXCALIBUR	8110	$\frac{24137}{100000}$	4112
T.G.C.-dependent 4-fermion $\lambda=-0.5$	EXCALIBUR	8261	$\frac{16841}{71500}$	3577
T.G.C.-dependent 4-fermion $\lambda=+0.5$	EXCALIBUR	8260	$\frac{23239}{100000}$	5235
T.G.C.-dependent 4-fermion $\lambda=+1$	EXCALIBUR	8109	$\frac{23579}{100000}$	4396
T.G.C.-dependent 4-fermion $\lambda=+2$	EXCALIBUR	8259	$\frac{24312}{100000}$	2634

TABLE A.2: Monte Carlo Reference samples at $\sqrt{s} = 189\text{GeV}$. The format is the same as that for table A.1

Table A.2 continued ...

Simulated Process	Generator	Run Number	$\frac{N_{\text{ACCEPTED}}}{N_{\text{SAMPLE}}}$	Luminosity (in fb ⁻¹)
T.G.C.-dependent 4-fermion $\Delta g_Z^1 = -2$	EXCALIBUR	8258	$\frac{24983}{100000}$	2232
T.G.C.-dependent 4-fermion $\Delta g_Z^1 = -1$	EXCALIBUR	8108	$\frac{24314}{100000}$	3962
T.G.C.-dependent 4-fermion $\Delta g_Z^1 = -0.5$	EXCALIBUR	8257	$\frac{23476}{100000}$	4954
T.G.C.-dependent 4-fermion $\Delta g_Z^1 = +0.5$	EXCALIBUR	8256	$\frac{23205}{100000}$	5160
T.G.C.-dependent 4-fermion $\Delta g_Z^1 = +1$	EXCALIBUR	8107	$\frac{24004}{100000}$	4222
T.G.C.-dependent 4-fermion $\Delta g_Z^1 = +2$	EXCALIBUR	8255	$\frac{24527}{100000}$	2401
T.G.C.-dependent 4-fermion $\Delta \kappa_\gamma = -2$	EXCALIBUR	8254	$\frac{24297}{100000}$	3998
T.G.C.-dependent 4-fermion $\Delta \kappa_\gamma = -1$	EXCALIBUR	8106	$\frac{24366}{100000}$	4981
T.G.C.-dependent 4-fermion $\Delta \kappa_\gamma = -0.5$	EXCALIBUR	8253	$\frac{23900}{100000}$	5344

Table A.2 continued ...

Simulated Process	Generator	Run Number	$\frac{N_{\text{ACCEPTED}}}{N_{\text{SAMPLE}}}$	Luminosity (in fb^{-1})
T.G.C.-dependent 4-fermion $\Delta\kappa_\gamma = +0.5$	EXCALIBUR	8252	$\frac{22927}{100000}$	5425
T.G.C.-dependent 4-fermion $\Delta\kappa_\gamma = +1$	EXCALIBUR	8105	$\frac{22205}{100000}$	5137
T.G.C.-dependent 4-fermion $\Delta\kappa_\gamma = +2$	EXCALIBUR	8251	$\frac{20978}{100000}$	4210
T.G.C.-dependent 4-fermion $\lambda = +1, \Delta g_Z^1 = +1$	EXCALIBUR	8113	$\frac{24464}{100000}$	2971
T.G.C.-dependent 4-fermion $\Delta g_Z^1 = +0.537,$ $\Delta\kappa_\gamma = +1$	EXCALIBUR	8111	$\frac{22199}{100000}$	5015
T.G.C.-dependent 4-fermion $\Delta\kappa_\gamma = +1, \lambda = +1$	EXCALIBUR	8112	$\frac{22610}{100000}$	4110
T.G.C.-independent 4-fermion (no e^+e^-)	EXCALIBUR	8101	$\frac{504}{52300}$	25250
e^-e^+ff (s-channel)	grc4f	8230	$\frac{230}{41402}$	25000
e^-e^+ff (t-channel)	grc4f	8231	$\frac{86}{150000}$	5000

Table A.2 continued ...

Simulated Process	Generator	Run Number	$\frac{N_{\text{ACCEPTED}}}{N_{\text{SAMPLE}}}$	Luminosity (in fb ⁻¹)
$Z^0/\gamma \rightarrow q\bar{q}$	PYTHIA	5078	$\frac{209}{175000}$	5066
Tagged Two-photon	HERWIG	1049	$\frac{5}{150000}$	497
$l^-\bar{\nu}_l l^+ \nu_l$ & $l\bar{l} l\bar{l}$ Standard Model	grc4f	7844	$\frac{7}{15354}$	4842
$q\bar{q} l \nu_l$ & $q\bar{q} l\bar{l}$ Standard Model	grc4f	8055	$\frac{21023}{43396}$	5000
$q'\bar{q}' q''\bar{q}''$ & $q\bar{q} q'\bar{q}'$ Standard Model	grc4f	7846	$\frac{31}{42088}$	5000
$e^-e^+ \rightarrow W^+W^-$ JETSET fragmentation	grc4f	8438	$\frac{21021}{82190}$	5000
$e^-e^+ \rightarrow W^+W^-$ HERWIG fragmentation	grc4f	8442	$\frac{9792}{38286}$	2311

BIBLIOGRAPHY

- [1] W.B.Rolnick, *The Fundamental Particles and their Interactions*, Addison-Wesley Publishing Company, Inc., 1994.
- [2] F. Halzen & A.D.Martin, *Leptons & Quarks*, Wiley & Sons, 1984.
- [3] Y. Fukuda et al, Evidence for Oscilation of Atmospheric Neutrinos, submitted to *Phys. Rev. Lett.* (1998).
<http://www-sk.icrr.u-tokyo.ac.jp/doc/sk/pub/nuosc98.submitted.pdf>
- [4] C. Caso et al, *The European Physical Journal* **C3** (1998) 1.
- [5] ALEPH, DELPHI, L3, OPAL Collaborations, CERN-EP/99-060 (1999).
- [6] I.J.R. Aitchison & A.J.G. Hey, *Gauge Theories in Particle Physics* (2nd Edition), Institute of Physics Publishing, 1989.
- [7] F.Mandl & G.Shaw, *Quantum Field Theory*, Wiley & Sons, 1993.
- [8] P. Cvitanović, *Field Theory*, Nordita, 1983.
- [9] J.P.Elliot & P.G.Dawber, *Symmetry in Physics*, The MacMillan Press, 1979.
- [10] F.Abe et al, *Phys. Rev. Lett.* **74** (1995) 1936, *Phys. Rev. Lett.* **75** (1995) 1017.
- [11] S. Abachi et al, *Phys. Rev. Lett.* **75** (1995) 1023, *Phys. Rev. Lett.* **75** (1995) 1034.
- [12] G. Gounaris et al, *International Journal of Modern Physics A*, Vol. 8, No. 19 (1993) 3285–3320.
- [13] M. Bilenky et al, *Nucl. Phys.* **B409** (1993) 22–68.

- [14] Physics at LEP2, Edited by G. Altarelli, T. Sjöstrand, F.Zwirner, Report on the LEP2 Workshop 1995, CERN 96-01 (1996).
- [15] G.J. Gounaris, F.M. Renard, G. Tsirigoti, Phys.Lett. **B350** (1995) 212.
- [16] R.L. Sekulin, Phys. Lett. **B338** (1994) 369.
- [17] C. Grosse-Knetter, I.Kuss, D.Schildknecht, Z.Phys. **C60** (1993) 375.
- [18] G.Bella, D.Charlton, P.Clarke, OPAL Technical Note TN492 (1997).
- [19] K. Hagiwara et al, Phys. Lett. **B283** (1992) 353, Phys. Rev. **D48** (1993) 2182.
- [20] C.P.Burgess & D.London, Phys. Rev. **D48** (1993) 4337–4351.
- [21] I.Trigger, S. von Dobschütz, OPAL Technical Note, TN476 (1997).
- [22] S. Myers, CERN Report 91–08 (1991).
- [23] K.Ahmer et al, OPAL Collaboration, Nucl. Instr. Meth. **A305** (1991) 275.
- [24] P.P.Allport et al, Nucl. Instr. Meth. **A346** (1994) 476.
- [25] J.R.Carter et al, Nucl. Instr. Meth. **A286** (1990) 99.
- [26] M.Hauschild et al, Nucl. Instr. Meth. **A314** (1992) 74.
- [27] H.Mes et al, Nucl. Instr. Meth. **A265** (1988) 445.
- [28] D.C.Imrie et al, Nucl. Instr. Meth. **A283** (1989) 515.
- [29] B.E.Anderson et al, Nucl. Instr. Meth. **A283** (1989) 650.
- [30] B.E.Anderson et al, IEEE Trans. Nucl. Sci. **41** (1994) 845.
- [31] G.Aguillion et al, Nucl. Instr. Meth. **A417** (1998) 266.
- [32] C.Beard et al, Nucl. Instr. Meth. **A286** (1990) 117.
- [33] M.Akrawy et al, Nucl. Instr. Meth. **A290** (1990) 76.

- [34] G.Bella et al, Nucl. Instr. Meth. **A252** (1986) 503.
- [35] S.Dado et al, Nucl. Instr. Meth. **A252** (1986) 511.
- [36] G.Mikenberg et al, Nucl. Instr. Meth. **A265** (1988) 223.
- [37] G.T.J.Arnison et al, Nucl. Instr. Meth. **A294** (1990) 431.
- [38] R.J.Akers et al, Nucl. Instr. Meth. **A357** (1995) 253. Check.
- [39] M.Arignon et al, Nucl. Instr. Meth. **A313** (1992) 103.
- [40] M.Arignon et al, Nucl. Instr. Meth. **A333** (1993) 330.
- [41] D.G.Charlton et al, Nucl. Instr. Meth. **A325** (1993) 129.
- [42] C.Hawkes et al, The Rope Users Guide, ROPE410 (1996).
- [43] J.Allison et al, Nucl. Instr. Meth. **A317** (1992) 47.
- [44] R.Brun et al, CERN Report DD/EE/84-1 (1984).
- [45] G. Marchesini et al, **hep-ph/9906412** (1998).
- [46] T.Sjöstrand, Comp. Phys. Comm. **39** (1986) 347. T.Sjöstrand & M.Bengtsson, Comp. Phys. Comm. **43** (1987) 367. T.Sjöstrand & H.-U.Bengtsson, Comp. Phys. Comm. **46** (1987) 43.
- [47] J. Fujimoto et al, Comput.Phys.Commun. **100** (1997) 128–156.
- [48] F.Berends & A.I. van Sighem, Nucl.Phys. **B454** (1995) 467–484.
- [49] S.Jadach et al, CERN-TH/98-242 (1998).
- [50] T.Sjöstrand, Comp. Phys. Comm. **82** (1994) 74. T.Sjöstrand, Lund University report LU TP 95-20 (1995).
- [51] <http://www.thep.lu.se/~torbjorn/pythia/pythia6127.f> (1997)
- [52] R.Engel & J.Ranft, Siegen SI 95-08 (1995).

- [53] WW111 Manual, Coordinators: C.P.Ward, D.R.Ward & N.K.Watson (1998). <http://opalinfo.cern.ch/opal/manuals/ww/pro/ww.html>
- [54] Embryonic Users Manual for the WV Package, The OPAL TGC Group (1997).
http://opalinfo.cern.ch/opal/group/ww/TgcWorkPage/wv/wv110_manual.ps
- [55] Stephen T. Betts, An evaluation of the $W^+W^- \rightarrow q\bar{q}l\nu_l$ likelihood selection in the WW110 package for use by the TGC Group, OPAL Informal Note, (1997).
http://opalinfo.cern.ch/opal/group/ww/TgcWorkPage/writeups/stb_ww110qqln.ps
- [56] K. Ackerstaff et al, Eur. Phys. J. **C2** (1998) 597-606.
- [57] A GRope Primer, <http://www.cern.ch/opal/manuals/gr/pro/gr.html>
- [58] D.M.Schmidt, R.J.Morrison & M.S.Witherell, Nucl. Instr. Meth. **A328** (1993) 547-552.
- [59] G. Arfken, Mathematical Methods for Physicists (3rd edition), Academic Press, Inc., 1985.
- [60] F. James & M. Roos, Comput.Phys.Commun. **10** (1975) 343-367.
- [61] F.James, Minuit Reference Manual, CERN Program Library Long Writeup D506 (1994).
- [62] R.J.Barlow, Statistics, J. Wiley & Sons, 1989.
- [63] William H. Press et al, Numerical Recipes in C (second edition), Cambridge University Press, 1992.
- [64] K.F.Riley, Mathematical Methods for the Physical Sciences, Cambridge University Press, 1974.
- [65] M.Lancaster, New Tevatron Measurements of the W Boson Mass. Proceedings Rencontres de Moriond Electroweak Interactions and Unified

- Theories, March 1999.
http://www-cdf.fnal.gov/physics/ewk/conferences/ml_moriond99.ps
- [66] LEP Energy Working Group, 98-01 (1998).
- [67] OPAL Run Summaries, <http://hpozon1.cern.ch:8080/runsum/runs97.html>
- [68] LEP Energy Working Group, 99-01 (1999).
- [69] OPAL Run Summaries, <http://hpozon1.cern.ch:8080/runsum/runs98.html>
- [70] The WW Working Group, OPAL Physics Note PN331 (1998).
- [71] The WW Working Group, OPAL Physics Note PN378 (1999).
- [72] N. Isamu, T.Kawamoto & S. Yamashita, OPAL Technical Note TN482 (1997).
- [73] K. Ackerstaff et al., Phys. Lett. **B397** (1997), 147.
- [74] The OPAL Collaboration, OPAL Physics Note PN375 (1999).
- [75] The OPAL Collaboration, OPAL Physics Note PN329 (1998).
- [76] G. Abbiendi et al, Eur. Phys. J. **C8** (1999) 191-215.
- [77] N. A. Graf, Production and Decay Properties of Gauge Bosons at the Tevatron. Proceedings Rencontres de Moriond Electroweak Interactions and Unified Theories, March 1999.
http://moriond.in2p3.fr/EW/transparencies/99/06_Friday/Friday_pm/Graf/main.pdf